FLOW INSTABILITIES OF ALASKAN GLACIERS

by

James Bradley Turrin

A dissertation submitted to the faculty of
The University of Utah
in partial fulfillment of the requirements for the degree of

Doctor of Philosophy

Department of Geography

The University of Utah

August 2014

The University of Utah Graduate School

STATEMENT OF DISSERTATION APPROVAL

The dissertation of James Bradley Turrin

has been approved by the following supervisory committee members:

Richard R. Forster	, Chair	6/11/2014 Date Approved
Philip E. Dennison	, Member	6/12/2014 Date Approved
Dorothy K. Hall	, Member	6/17/2014 Date Approved
Kathleen Nicoll	, Member	Date Approved
Ronald L. Bruhn	, Member	Date Approved

and by Andrea Brunelle , Chair of

the Department of Geography

and by David B. Kieda, Dean of The Graduate School.

ABSTRACT

Over 300 of the largest glaciers in southern Alaska have been identified as either surge-type or pulse-type, making glaciers with flow instabilities the norm among large glaciers in that region. Consequently, the bulk of mass loss due to climate change will come from these unstable glaciers in the future, yet their response to future climate warming is unknown because their dynamics are still poorly understood. To help broaden our understanding of unstable glacier flow, the decadal-scale ice dynamics of 1 surging and 9 pulsing glaciers are investigated.

Bering Glacier had a kinematic wave moving down its ablation zone at 4.4 ± 2.0 km/yr from 2002 to 2009, which then accelerated to 13.9 ± 2.0 km/yr as it traversed the piedmont lobe. The wave first appeared in 2001 near the confluence with Bagley Ice Valley and it took 10 years to travel ~64 km. A surge was triggered in 2008 after the wave activated an ice reservoir in the midablation zone, and it climaxed in 2011 while the terminus advanced several km into Vitus Lake.

Ruth Glacier pulsed five times between 1973 and 2012, with peak velocities in 1981, 1989, 1997, 2003, and 2010; approximately every 7 years. A typical pulse increased ice velocity 300%, from roughly 40 m/yr to 160 m/yr in the midablation zone, and involved acceleration and deceleration of the ice en masse; no kinematic wave was evident. The pulses are theorized to be due to deformation of a subglacial till causing enhanced basal motion.

Eight additional pulsing glaciers are identified based on the spatiotemporal pattern of their velocity fields. These glaciers pulsed where they were either constricted laterally or joined by a tributary, and their surface slopes are 1–2°. These traits are consistent with an overdeepening. This observation leads to a theory of ice motion in overdeepenings that explains the cyclical behavior of pulsing glaciers. It is based on the concept of glaciohydraulic supercooling, and includes sediment transport and erosion along an adverse slope, ice thickening, and ablation of the ice surface such that the ratio of the angle of the adverse slope to ice surface slope oscillates around the supercooling threshold.

I would like to dedicate this work to Gerald and Margie, Helen and Dan,

Frank and Beulah, and most importantly to Mom and Dad.

I miss you and I love you.

"Glaciers are delicate and individual things, like humans.

Instability is built into them."

Will Harrison

TABLE OF CONTENTS

Chapters

3. A MECHANISM FOR CYCLICAL GLACIER FLOW IN OVERDEEPENINGS……………………………………………………………….. 75

LIST OF TABLES

INTRODUCTION

During the 2000s total sea-level rise was found to be 2.4–2.7 mm/yr (Leuliette & Miller, 2009); 1.2 mm/yr of this is due to thermal expansion of the oceans (Antonov et al., 2005), 0.4 mm/yr comes from glaciers and ice caps, and the remainder from the two ice sheets covering Greenland and Antarctica (Jacob et al., 2012). By 2100 sea-level could rise 0.5–2.0 m, based on a predicted temperature increase of 4°C, and displace an estimated 187 million people (Nicholls et al., 2011). Appropriately, sea-level rise and the contribution to it from glaciers is a vigorous area of scientific inquiry.

Over the past 14 years most Alaskan glaciers have been shown to be retreating, thinning, and losing mass. Adalgeirsdóttir et al. (1998) and Arendt et al. (2002) compared old topographic maps and laser altimetry profiles of Alaskan and Yukon glaciers, and demonstrated that widespread glacial thinning occurred between the mid-1950s and the mid-1990s. Luthcke et al. (2008) used Gravity Recovery and Climate Experiment (GRACE) mass concentration (mascon) data to show that all 12 mascon regions covering Alaska's glaciated areas are losing mass. They established a rate of mass loss for each region, ranging from -3.6 ± 0.3 to -15.3 ± 0.7 gigatons/yr from 2003 to 2007. Berthier et al. (2010) used Digital Elevation Model (DEM) differencing to show, on a glacier-by-glacier basis, that nearly all Alaskan glaciers are thinning, with losses of -2 to -10 m/yr typical near glacier fronts over the last 50 years. Consequently, Alaskan glaciers' contribution to sea-level rise is estimated to be 0.12 ± 0.02 mm/yr over the past 50 years, which comprises 1/3rd of the total contribution from all mountain glaciers and ice caps on Earth (Berthier et al., 2010).

While it is possible to measure the effects of climate change on Alaskan glaciers' mass balance and their resulting contribution to sea-level rise over the past several decades, it is not clear what the effects of climate change have been, or will be, on the dynamics of many of these glaciers. Alpine glaciers move down slope via gravity, by sliding at the ice/bed interface underneath the glacier and by internal deformation (creep) of the ice under its own weight (Note: glacier motion via till deformation is often lumped with sliding). Both mechanisms are influenced by climate; the rate of creep is proportional to the 4th power of the ice thickness (Paterson, 1981), which in turn is determined by the amount of winter snowfall and summer surface melt. Likewise, sliding at the glacier base is influenced by the ice thickness and the amount of water available at the glacier base for lubrication (Paterson, 1981); again, both of these are determined by winter snowfall and summer melt. For land-terminating stable glaciers, ice velocity is expected to decrease due to reduced mass flux when mass balance is negative, as has been observed by Heid and Kääb (2012) in the Central Alaska Range. However, this simple relationship does not apply to glaciers with dramatic, periodic flow instabilities, such as tidewater glaciers and surging glaciers; and it may not apply so simply to other glaciers with lesser flow instabilities, such as pulsing glaciers, or glaciers that experience regular spring sliding events or jökulhlaups (glacier outburst floods).

Post (1969) notes the existence of over 200 surge-type glaciers in southern Alaska and adjacent Yukon, Canada, and Mayo (1978) found roughly 140 pulse-type glaciers in southern Alaska. Consequently, Mayo (1978) noted that large glaciers of unstable type are more common in southern Alaska than stable glaciers. Ultimately, the bulk of

Alaska’s contribution to sea-level rise in the future will come from these glaciers, which contain the majority of ice volume. Unfortunately, surges and pulses are seldom-observed glacial phenomena that greatly influence mass balance. So, how are large, unstable Alaskan glaciers responding to climate change? We begin to answer this question by studying the behavior of these glaciers over decades, where possible, and observing what aspects of their behavior have changed, what has remained constant, and what processes influence their dynamic response to climate change. To further our understanding of the dynamic behavior of large, unstable Alaskan glaciers, and to help predict their response to future climate change, the following chapters present: 1) a surge of Bering Glacier that was observed over a 10-year period, the results of which can be compared to its previous surge in 1993–95 and to future surges, and which will help establish a trend in surge behavior relative to climate change; 2) five pulses of Ruth Glacier that were observed over a 39-year period that expands our base of knowledge concerning this little-known phenomenon; and 3) a new theory explaining the cyclical behavior of ice velocity through overdeepenings that is based on observations of eight additional pulsing glaciers over four decades, and that identifies the glaciological processes responsible for this behavior and their major forcings.

Each of the three chapters that follow present measurements of glacier movement obtained via optical feature tracking methods. The details of how optical feature tracking works may be found in the Methods section within each chapter, so instead, here is presented an overview of the development of optical feature tracking in the field of glaciology and the people who still work to advance its capabilities. Optical feature tracking algorithms measure the movement of land-surface features, such as glaciers, sand dunes, permafrost, or faults, between sequential aerial or satellite images. Feature tracking algorithms typically use a cross-correlation function in either the spatial domain to find the peak correlation of brightness values between two images, or in the Fourier domain to find the peak correlation between the magnitude or the phase of two images. Optical feature tracking was first proven effective by Bindschadler and Scambos (1991) who used Landsat Thematic Mapper satellite imagery in conjunction with a feature tracking algorithm (later named Image Correlator [IMCORR]) to measure the velocity of Ice Stream E in Antarctica between January, 1987 and December, 1988. The team of Bindschadler and Scambos published four more papers presenting velocity measurements of ice streams and ice shelves in Antarctica between 1992 and 1996 using IMCORR and Landsat imagery (Bindschadler et al., 1994; Bindschadler et al., 1996; Scambos et al., 1992; Scambos & Bindschadler, 1993). Then in 1997, Rolstad et al. presented a study of Osbornebreen, Svalbard, during a surge using a feature tracking algorithm in conjunction with Landsat and Satellite Pour l'Observation de la Terre (SPOT) satellite imagery. This was the first application of optical feature tracking to an alpine glacier and also the first application to a surging glacier. In 2000 Kääb and Vollmer at the University of Oslo, Norway, published results of optical feature tracking on permafrost creep, expanding the application of this method in alpine environments and introducing their version of a cross-correlation program called Correlation Image Analysis (CIAS). Until 2007 all feature tracking programs used in glaciology searched for peaks in correlation among brightness values in the spatial domain, or magnitude in the Fourier domain (both of which are mathematically equivalent, but computation in the Fourier domain is faster). In 2007 Leprince et al. introduced a new optical feature tracking program called Coregistration of Optically Sensed Images and Correlation (COSI-Corr), which seeks the peak correlation based on the phase of sequential digital images in the Fourier domain.

This technique, termed phase correlation, has the advantage of a very sharp correlation peak that allows for greater subpixel accuracy and was originally developed to measure fault displacement following earthquakes using Advanced Spaceborne Thermal Emission and Reflection Radiometer (ASTER) satellite imagery. Scherler, et al. (2008) were the first to apply COSI-Corr to glaciers (of the Himalaya Mountains), with an accuracy of 1/20th to 1/10th of a pixel. By 2011 both cross-correlation and phase correlation had been adapted to work with Landsat-7 images that contain scan-line voids (Ahn & Howat, 2011; Haug et al., 2010), thus expanding the archive of satellite imagery suitable for use in optical feature tracking.

Currently, there are three notable groups who regularly publish glaciological research utilizing optical feature tracking methods and who work to expand the capabilities of this method: Sebastian Leprince and his peers at the California Institute of Technology, who developed COSI-Corr and have applied it to glaciers (Scherler et al., 2008), faults (Leprince et al., 2007), sand dunes on Earth (Vermeesch & Drake, 2008), and sand dunes on Mars (Bridges et al., 2012); Andreas Kääb and his group at the University of Oslo, who introduced Orientation Correlation (Haug et al., 2010) for use with Landsat-7 images containing scan-line voids and methods to automatically select appropriate subimage sizes for correlation (Debella-Gilo & Kääb, 2012), and who first applied optical feature tracking to Moderate-resolution Imaging Spectroradiometer (MODIS) images of Antarctic ice shelves (Haug et al., 2010); and Ian Howat and his associates at the Byrd Polar Research Center at The Ohio State University, who developed the null-exclusion method for use with Landsat-7 images with scan-line voids (Ahn & Howat, 2011), and who study the outlet glaciers of the Greenland Ice Sheet (Howat et al., 2008).

References

Adalgeirsdóttir, G., Echelmeyer, K. A., & Harrison, W. D. (1998). Elevation and volume changes on the Harding Icefield, Alaska. *Journal of Glaciology, 44*(148), 570–582.

Ahn, Y., & Howat, I. (2011). Efficient automated glacier surface velocity measurement from repeat images using Multi-Image/Multichip and null exclusion feature tracking. *IEEE Transactions on Geoscience and Remote Sensing*, *49*(8), 2838–2846.

Antonov, J. I., Levitus, S., & Boyer, T. P. (2005). Thermosteric sea level rise, 1955–2003. *Geophysical Research Letters*, *32*(12), doi:10.1029/2005GL023112.

Arendt, A. A., Echelmeyer, K. A., Harrison, W. D., Lingle, C. S., & Valentine, V. B. (2002). Rapid wastage of Alaska glaciers and their contribution to rising sea-level. *Science*, *297*(5580), 382–386.

Berthier, E., Schiefer, E., Clarke, G. K. C., Menounos, B., & Rémy, F. (2010). Contribution of Alaskan glaciers to sea-level rise derived from satellite imagery. *Nature Geoscience Letters*, doi:10.1038/ngeo737.

Bindschadler, R. A. & Scambos, T. A. (1991). Satellite-image-derived velocity field of an Antarctic ice stream. *Science*, *252*(5003), 242–246.

Bindschadler, R. A., Fahnstock, M. A., Skvarca, P., & Scambos, T. A. (1994). Surface-velocity field of the northern Larsen Ice Shelf, Antarctica. *Annals of Glaciology*, *20*(1), 319–326.

Bindschadler, R., Vornberger, P., Blankenship, D., Scambos, T., & Jacobel, R. (1996). Surface velocity and mass balance of Ice Streams D and E, West Antarctica. *Journal of Glaciology*, *42*(142), 461–475.

Bridges, N. T., Ayoub, F., Avouac, J. P., Leprince, S., Lucas, A., & Mattson, S. (2012). Earth-like sand fluxes on Mars. *Nature, 485*(7398), 339–342.

Debella-Gilo, M., & Kääb, A. (2012). Locally adaptive template sizes for matching repeat images of Earth surface mass movements. *ISPRS Journal of Photogrammetry and Remote Sensing*, *69*, 10–28.

Haug, T., Kääb, A., & Skvarca, P. (2010). Monitoring ice shelf velocities from repeat MODIS and Landsat data – A method study on the Larsen C ice shelf, Antarctic Peninsula, and 10 other ice shelves around Antarctica. *The Cryosphere, 4*(2), 161–178.

Heid, T., & Kääb, A. (2012). Repeat optical satellite images reveal widespread and long term decrease in land-terminating glacier speeds. *The Cryosphere*, *6*(2), 467–478.

Howat, I. M., Joughin I., Fahnstock, M., Smith, B. E., & Scambos T. A. (2008). Synchronous retreat and acceleration of southeast Greenland outlet glaciers 2000–06: Ice dynamics and coupling to climate. *Journal of Glaciology*, *54*(187), 646–660.

Jacob, T., Wahr, J., Pfeffer, W. T., & Swenson, S. (2012). Recent contributions of glaciers and ice caps to sea level rise. *Nature*, *482*(7386), 514-518.

Kääb, A., & Vollmer, M. (2000). Surface geometry, thickness changes and flow fields on creeping mountain permafrost: Automatic extraction by digital image analysis. *Permafrost and Periglacial Processes*, *11*(4), 315–326.

Leprince, S., Barbot, S., Ayoub, F., & Avouac, J. P. (2007). Automatic and precise ortho-rectification, coregistration, and subpixel correlation of satellite images, application to ground deformation measurements. *IEEE Transactions on Geoscience and Remote Sensing*, *45*(6), 1529–1558.

Leuliette, E. W., & Miller, L. (2009). Closing the sea level rise budget with altimetry, Argo, and GRACE. *Geophysical Research Letters, 36*(4).

Luthcke, S. B., Arendt, A. A., Rowlands, D. D., McCarthy, J. J., & Larsen, C. F. (2008). Recent glacier mass changes in the Gulf of Alaska region from GRACE mascon solutions. *Journal of Glaciology*, *54*(188), 767–777.

Mayo, L. R. (1978). Identification of unstable glaciers intermediate between normal and surging glaciers. Academy of Sciences of the USSR. *Section of Glaciology of the Soviet Geophysical Committee and Institute of Geography, Data of Glaciological Studies Chronicle*, Discussion, Publication 133, 133–135, Moscow, May 1978.

Nicholls, R. J., Marinova, N., Lowe, J. A., Brown, S., Vellinga, P., de Gusmao, D., Hinkel, J., & Tol, R. S. J. (2011). Sea-level rise and its possible impacts given a ‘beyond 4°C world’ in the twenty-first century. *Philosophical Transactions of The Royal Society A, Mathematical, Physical, and Engineering Sciences, 369*(1934), 161-181.

Paterson, W. S. B. (1981). *The Physics of Glaciers, 2nd edition*. Pergamon Press, Oxford.

Post, A. (1969). Distribution of surging glaciers in western North America. *Journal of Glaciology*, *8*(53), 229–240.

Rolstad, C., Amlien, J., Hagen, J., & Lunden, B. (1997). Visible and near-infrared digital images for determination of ice velocities and surface elevation during a surge on Osbornebreen, a tidewater glacier in Svalbard. *Annals of Glaciology*, *24*, 255–261.

Scambos, T. A., Dutkiewicz, M. J., Wilson, J. C., & Bindschadler, R. A. (1992). Application of image cross-correlation to the measurement of glacier velocity using satellite image data. *Remote Sensing of Environment*, *42*(3), 177–186.

Scambos, T. A. & Bindschadler, R. (1993). Complex ice stream flow revealed by sequential satellite imagery. *Annals of Glaciology*, *17*, 177–182.

Scherler, D., Leprince, S., & Strecker, M. (2008). Glacier-surface velocities in alpine terrain from optical satellite imagery – Accuracy improvement and quality assessment. *Remote Sensing of Environment*, *112*(10), 3806–3819.

Vermeesch, P., & Drake, N. (2008). Remotely sensed dune celerity and sand flux measurements of the world’s fastest barchans (Bodélé, Chad). *Geophysical Research Letters*, *35*(24), doi10.10292008GL035921.

CHAPTER 1[1]

THE PROPAGATION OF A SURGE FRONT ON BERING GLACIER, ALASKA, 2001–2011

1.1 Abstract

Bering Glacier has an approximately 20 year surge cycle, with its most recent surge reaching the terminus in 2011. To study this most recent activity a time-series of ice velocity maps was produced by applying optical feature tracking methods to Landsat-7 ETM+ imagery spanning 2001 to 2011. The velocity maps show a yearly increase in ice surface velocity associated with the downglacier movement of a surge front. In 2008-2009 the maximum ice surface velocity was 1.5 ± 0.017 km/yr in the midablation zone, which decreased to 1.2 ± 0.015 km/yr in 2009-2010 in the lower ablation zone, and then increased to nearly 4.4 ± 0.03 km/yr in summer 2011 when the surge front reached the glacier terminus. The surge front propagated downglacier as a kinematic wave at an average rate of 4.4 ± 2.0 km/yr between September 2002 and April 2009, then accelerated to 13.9 ± 2.0 km/yr as it entered the piedmont lobe between April 2009 and September 2010. The wave seems to have initiated near the confluence of Bering Glacier and Bagley Ice Valley as early as 2001, and the surge was triggered in 2008 further

---

[1] Reprinted from *Annals of Glaciology,* with permission of the International Glaciological Society. Turrin J, Forster RR, Larsen C, Sauber J (2013). The propagation of a surge front on Bering Glacier, Alaska. *Annals of Glaciology, 54*(63), 221-228.

downglacier in the midablation zone after the wave passed an ice reservoir area. Overall, it took the kinematic wave from 2001 to 2011 to travel ~64 km in the ablation zone.

1.2 Introduction

1.2.1 Surges and Bering Glacier

Surging glaciers are distinguished by their periods of brief but anomalously fast flow, known as the active phase, and their often long periods of nearly stagnant flow, known as the quiescent phase (Post, 1969). The active phase, or “surge,” rapidly, sometimes violently, transports large volumes of ice downglacier from a reservoir area, often located in the accumulation zone, to the ablation zone and to the terminus, often causing the terminus to thicken by tens of meters and to advance by kilometers (e.g., Variegated Glacier; Kamb et al., 1985). During the ice transport process, fast-moving surging ice upglacier pushes against slow-moving quiescent ice downglacier, resulting in compression of the ice at the contact between the two, creating the surge front. Compression causes the ice at the location of the surge front to thicken, forming a kinematic wave. The kinematic wave represents the boundary between surging ice and quiescent ice, which in turn is located at the boundary between a high-pressure, slow-flow, linked-cavity drainage system upglacier and a low-pressure, fast-flow, channelized drainage system downglacier (Fowler, 1987). Therefore, a kinematic wave can be observed as a propagating front of increased ice thickness or increased ice velocity moving downglacier at a rate faster than the speed of the ice. When a sufficient length of the subglacial drainage system has been transformed to a high-pressure, linked-cavity system and the longitudinal driving stress overcomes the resisting force of drag along the glacier base and valley walls, the glacier will surge.

Theory and observations suggest a glacier will initiate a surge after it has attained an unstable geometry in which its accumulation zone is anomalously thick compared to its ablation zone (Kamb et al., 1985), and the glacier is in a severe state of mass disequilibrium. Lingle and Fatland (2003) proposed an 11-point theory suggesting englacial and subglacial storage of high-pressure water eventually drives a glacier in disequilibrium to surge by promoting widespread basal slip. Sliding may begin at a single nucleation point where local resistive stresses are overcome by driving stresses, thereby transferring the driving stresses to nearby locations that are also near their resistive threshold, and which will also begin sliding. This creates an ever-increasing area beneath the glacier that slides, thus initiating a surge (Fowler, 1987). These ideas imply climate has some control on surge frequency. The rate of snow accumulation in the glacier's upper reaches determines the rate at which a glacier will attain the necessary geometry to surge, and it will determine the ice thickness, which in turn determines the driving stress. The rate of ablation will determine the rate of ice thinning in the glacier's lower reaches and it will determine the rate and amount of meltwater for englacial and subglacial storage throughout.

During the 20th century Bering Glacier (Figure. 1.1) surged five times, ca. 1900, ca. 1920, ca. 1938–1940, 1957–1967, and 1993–1995; approximately every 20 years (Molnia & Post, 2010). The 1993–1995 surge was keenly studied using aerial photography (Herzfeld & Mayer, 1997; Lingle et al., 1993) and Synthetic Aperture Radar (SAR) data (Fatland & Lingle, 1998; Lingle & Fatland, 2003; Roush et al., 2003). The surge started well below the Equilibrium Line Altitude (ELA) during winter, and was associated with high englacial water pressures. This was evidenced by artesian, clear, blue water in fresh crevasses (Lingle et al., 1993), and by interferometric detection of vertical displacements in Bagley Ice Valley indicating localized subglacial hydraulic jacking (Fatland & Lingle, 1998; Lingle & Fatland, 2003). Analysis of SAR images showed the surge front propagated downglacier at a rate of 75–112 m/day (27–40 km/yr) in a wave-like fashion, while the ice velocity was considerably less, 10–20 m/day (3.7–7.3 km/yr; Roush et al., 2003). The surge also propagated upglacier at 200–500 m/day (73–182 km/yr) into Bagley Ice Valley, significantly faster than the rate at which it moved downglacier. Each stage of the surge (August, 1994 and September, 1995) ended with an outburst of turbid water into proglacial Vitus Lake (Fatland & Lingle, 1998).

Optical satellite imagery of the 1993–1995 surge is not available due to lack of acquisitions and cloud cover, and SAR interferometry is only capable of producing glacier velocity fields over short time spans (days to weeks), not over an entire year, so the presurge build-up and climax of the surge has never been studied on an annual basis. During the 2000s, though, Bering Glacier began a new surge phase and there is sufficient optical satellite imagery to study the surge through the entire process in the ablation zone.

1.2.2 Previous Observations of Kinematic Waves on Glaciers

Traveling waves on glaciers have been reported since the 1890s (Sharp, 1954), with observations on the Mer de Glace, France, in 1891–1895 (Vallot, 1900); on glaciers in Yakutat Bay, Alaska in the early 1900s (Tarr & Martin, 1914); on Hintereisferner, Austria, in 1905 (Blümcke & Finsterwalder, 1905); on Black Rapids Glacier, Alaska in 1936–1937 (Hance, 1937); and on Nisqually Glacier, Washington, USA in the 1950s and 1960s (Harrison, 1956; Johnson, 1953; Meier & Johnson, 1962). The 1982–1983 surge of Variegated Glacier was particularly well studied (Kamb et al., 1985; Raymond, 1987). A surge front was observed on Variegated Glacier that was described as a bulge propagating downglacier which was nearly coincident with a peak in velocity. As the front moved downglacier, the peaks in height and velocity increased in amplitude and approached the leading edge of the wave. This resulted in a shock-like surge front with longitudinal compression ahead of the surge front and extension behind it. More recently a surge front was observed, via repeat image feature tracking, on Kunyang Glacier in the Karakoram Mountains of Pakistan (Quincey et al., 2011). Over a 4 year period from 2006 to 2010 it was possible to track a velocity front as it grew in intensity and moved downglacier, until it eventually diminished as the surge ended. However, the rate at which the surge front propagated downglacier was not measured.

In general, the response of Alaskan glaciers to the warming climate has been to retreat (Hall et al., 2005), thin (Adalgeirsdóttir et al., 1998; Arendt et al., 2002; Berthier et al., 2010; Luthcke et al., 2008), and decelerate (Heid & Kääb, 2012a). Exactly how surging glaciers will respond to warming trends, either by increasing or decreasing surge frequency and magnitude, is unknown. A complete surge cycle, including the quiescent and active phases, may last from several decades to more than a century (Post, 1969). Therefore, it is important to study every surge possible because they occur only intermittently, and it is important to establish a baseline with which future observations may be compared to determine any changes in surge behavior. Consequently, the aim of this study is to observe the build-up and movement of a surge front on Bering Glacier as it progresses downglacier, measure its speed of propagation, and compare the results with previous observations of the 1993–1995 surge. The results will add to our understanding of the behavior of surging glaciers and their associated kinematic waves in the context of a warming climate.

1.3 Methods

For this study two different tracking algorithms were applied to sequential Landsat-7 ETM+ images of the ablation zone to measure the increase in ice surface velocity through time. The first method used orientation images, which are produced by calculating the gradient in brightness values in the north-south and east-west directions across the satellite image, thereby creating a complex image in which the east-west gradient is the real part and the north-south gradient is the imaginary part. Then the signum function (x/|x|) is applied to produce an image with values ranging from -1 to 1 (Fitch et al., 2002; Haug et al., 2010). Orientation images were used because they have been shown to be effective in feature tracking on large glaciers, specifically ice shelves in Antarctica (Haug et al., 2010). Further, orientation images are not affected by seasonal changes in solar illumination, which is beneficial when performing feature tracking on images taken during different seasons of different years, such as the July 2009 and September 2010 images used in this study (Table 1.1). Also, orientation images are not impacted by areas of uniform brightness, such as featureless snow patches found in some of the winter images also used in this study (Table 1.1). The orientation images were inserted into COSI-Corr feature tracking software (Leprince et al., 2007) to produce velocity maps of Bering Glacier for dates before failure of Landsat-7's scan line correction mirror in May, 2003. COSI-Corr makes use of the Fourier shift theorem which states the shift between two images is found in their phase difference, as opposed to the similarity of their intensities as with cross-correlation. Transformation of the images into the frequency domain allows isolation of the phase difference and measurement of the displacement between the two images (Shekarforoush et al., 1996). COSI-Corr was chosen due to its proven precision (1/10th pixel; Scherler et al., 2008), and because it executes faster than statistical cross-correlation which is performed in the spatial domain.

The second feature tracking program is a statistical cross-correlation algorithm that operates in the spatial domain based upon the work of Ahn and Howat (2011). It is robust when given Landsat-7 ETM+ images that contain scan line data voids (SLC-off images), whereas COSI-Corr is not. To achieve this robustness, pixels that lie within a data void are excluded from the cross-correlation calculations; therefore, only actual recorded brightness values contribute to the displacement measurements. Ahn and Howat (2011) suggest the use of large reference areas with a minimum size of 100 x 100 pixels to provide a sufficient number of valid pixels (in the presence of data voids that can be 30 pixels wide) to obtain accurate correlation results. This method was used to produce velocity measurements for areas of the glacier affected by scan line voids. The piedmont lobe and much of the ablation zone lie within an area in the satellite images in which the scan line data voids disappear. So, in this area the combination of orientation images and COSI-Corr was used to produce velocity measurements, instead of statistical cross-correlation, after May, 2003.

Individual point displacements are assigned to the center of the search window from which they were derived. In the case of statistical cross-correlation this is reasonable because the displacement measurement represents how well pixels within the smaller reference window (centered within the search window) match an equally sized patch within the larger search window. Thus, the displacement represents movement of the ice encompassed within the reference window, taken from the first image, to a new location within the second image. Because the displacement measurement begins at the center of the windows, it is reasonable to assign it to this position within the first image of the image-pair. For the case of phase correlation, such as COSI-Corr, the search and reference windows are the same size, so the dominant feature that is tracked may lie anywhere within the windows. It is not feasible to visually examine every match produced by a phase correlation program and determine the location of the feature matched within the windows; therefore, the displacement measurement is assigned to the center pixel of the search window.

Traditionally, optical feature tracking has been performed on the ablation areas of alpine glaciers using summer images in which there are numerous ice surface features to track. However, initial application of the feature tracking programs to summer images obtained in 2001 and 2002 revealed the effects of shifting surface features caused when sediment layers emerge from the ice due to ablation (Bruhn et al., 2009). This happens because the exposed edge of the sediment layer lies within a different plane than the ice surface and therefore moves relative to the ice surface as ice melts. This phenomenon is so prevalent on the lower portion of the ablation zone that feature tracking using summer images from 2001 and 2002 yielded unusable results, because the ice is nearly stagnant during the quiescent phase and the apparent motion of the emergent sediment layers is greater than the downglacier motion of the ice. Therefore, feature tracking was performed on images in which the ablation zone was snow-covered (April 2001 and April 2002) to avoid this problem. The snow in the ablation zone is sufficiently deep to hide the effects of emergent sediment layers; while other features such as prominent medial moraines and crevasses have greater visual contrast, even when snow-covered, and are distinguishable. Therefore, these moraines and crevasses can be reliably tracked because they dominate the local search window, rather than the emergent sediment layers that are buried by snow in winter.

Five velocity maps were produced from the Landsat-7 images, with time frames spanning: 2001–2002, 2003–2004, 2006–2007, 2008–2009, and 2009–2010. See Table 1.1 for specific image dates and their use. By summer 2011 the glacier surface was too disrupted by crevasses and contortion of surface features to extract accurate displacement measurements using repeat image feature tracking. Therefore, manual feature tracking was used to measure the displacement of large, obvious moraine features for 2010–2011 by visually determining their movement from one image to the next.

The point displacements produced using the feature tracking programs are post-processed to eliminate erroneous matches, remove image-to-image georeferencing error, and then turned into velocity rasters. Displacements on dry, cloud-free, snow-free land are averaged to determine the mean georeferencing error between sequential satellite images (Table 1.1). This error is subtracted from the on-ice displacements to improve their accuracy. The on-ice displacements are filtered using a neighborhood analysis routine to remove statistical outliers. Vectors that have either a direction or magnitude more than ±2 standard deviations away from their local neighborhood mean (computed from at least the nine nearest vectors) are deemed anomalies and removed. The vector field is then visually inspected and any remaining anomalous vectors are manually removed. The point data are interpolated using a linear inverse distance weighting scheme and then smoothed using a mean filter to produce a velocity raster (Figure 1.2) in which the mean is calculated over the area contained by the search window used to produce the velocity field.

The accuracy of optical feature tracking methods depends upon how well the two images are coregistered to one another and the precision of the algorithm used. Typical misalignment between two Landsat-7 ETM+ images acquired within the same World Reference System path and row on different days is < 5 m (Lee et al., 2004). We find misalignments between sequential satellite images ranging from 1.3 to 10.2 m (Table 1.1), with a mean (±1 standard deviation) for all image pairs of 4.8 ± 3.1 m, which is in agreement with the value give by Lee et al. (2004). The precision of COSI-Corr is approximately 1 m when applied to ETM+ imagery, and for statistical cross-correlation it is approximately 9 m (Heid & Kääb, 2012b). Using the root sum of squares method, the overall error in the resulting velocity maps is ±5 m when using COSI-Corr and ±10 m when statistical cross-correlation is used. These error estimates are valid on dry land without deformation of surface features from one image to the next. Removal of the mean georeferencing error, as described above, will decrease these error estimates. The precision of the 2010–2011 displacements obtained using manual feature tracking is estimated to be ±2 pixels (±30 m) due to the diffuse nature of the moraines that were matched and deformation of the features from one image to the next during the surge climax.

The error in the displacement measurements on the glacier ice produced by the feature tracking programs is difficult to quantify due to compressive and extensive deformation, rotation, emergent features, and crevassing. Statistical cross-correlation is robust against deformation (compression and extension) of surface features due to its pixel-by-pixel correlation process; however, the degree of its robustness has not been quantified. Phase correlation is more sensitive to feature deformation than statistical cross-correlation, but COSI-Corr incorporates a least squares routine so it is also robust versus surface compression and extension, as well as rotation. Again, the degree of its robustness has not been quantified. Both feature tracking algorithms are susceptible to mismatches from emergent features and crevassing, but these can be removed with the filtering routines described herein. As ice velocity increases during the surge it is reasonable to assume the degree of surface deformation will also increase. Therefore, we assume the amount of error in the feature tracking results increases linearly with velocity, from a minimum of ±10 m to a maximum of ±30 m, coinciding with little deformation for slowly moving ice and with the error associated with visual feature tracking during the surge climax, respectively. This yields a simple linear equation (1) that is used to estimate the error of the velocity calculations. Using equation (1) the error associated with a velocity of 1500 m/yr (roughly the peak velocity in 2008-2009; Figure 1.3) is ±17.5 m/yr, or slightly more than ±1 pixel/yr. At a velocity of 4390 m/yr, the maximum velocity found using visual feature tracking, the error is ±30 m/yr, or ±2 pixels/yr. These error estimates are approximately 1%, or less, of their associated velocities and are smaller than the line thickness and size of the individual data points displayed in Figure 1.3; therefore, no error bounds are shown.

$$\text{Error} = [0.01\overline{33} * \text{Velocity} + 10] \, / \, \text{time} \qquad (1)$$

1.4 Results

Five velocity fields were produced spanning 2001 to 2010 (Figure 1.2). A velocity profile along transect A–A’ for each of the 5 velocity fields illustrates the progression of the surge front downglacier through time (Figure 1.3). Beginning with the 2001–2002 profile, we interpret the small rise in velocity at approximately 6 km from the confluence with Bagley Ice Valley to be the first observable instance of the surge front. In later years it is evident by looking at the peak velocities that the surge front steadily progresses downglacier and the ice steadily accelerates year-by-year, until there is a drop in maximum ice velocity from roughly 1.4 ± 0.016 km/yr in 2008–2009 to 1.2 ± 0.015

km/yr in 2009–2010. It should be noted that the 2008–2009 velocity field was produced using winter images (see Table 1.1), so the velocity field does not extend upglacier as far as the others due to thicker snow cover at higher elevations obscuring features.

Due to large ice surface deformation and heavy crevassing in summer 2011, repeat image feature tracking was unsuccessful. However, manual tracking of medial moraines was still possible in the lower half of the ablation zone. Manual feature tracking results, shown as individual points in Figure. 1.3, reveal the piedmont lobe experienced nearly a three-fold increase in velocity compared to the previous 2008–2009 maximum, with velocities close to 4.4 ± 0.03 km/yr near the glacier terminus and decreasing rapidly upglacier.

By plotting the position of the surge front's peak velocity versus time it is possible to determine the rate at which the surge front moved downglacier (Figure 1.4). The slope of the line fitted through the points from September 2002 to April 2009 gives the mean celerity of the surge front during this time, 4.4 ± 2.0 km/yr. This velocity is greater than the velocity at which the ice moves, which indicates the surge front moves as a kinematic wave. From April 2009 to September 2010 the celerity of the surge front increased to 13.9 ± 2.0 km/yr. Selecting the location of the peak of the surge front to track its movement downglacier is subjective, with unknown errors, because the peak is not always obvious. Therefore, the error given for the kinematic wave celerity, ±2.0 km/yr, is the standard deviation of the regression analysis used to determine the mean celerity and should be considered a minimum.

1.5 Discussion

1.5.1 Ice Dynamics of the Surge

Burgess et al. (2012) found, via SAR speckle tracking over monthly repeat intervals, that the surge had two phases of acceleration surrounding a slower phase. The first acceleration phase, from September 2008 to February 2009 had ice velocities up to 7 m/day (2.5 km/yr) and the second phase of acceleration, summer 2011, had velocities up to 9 m/day (3.2 km/yr). These speckle tracking results are of comparable magnitude to the velocities presented here for the April 2008–April 2009 (1.5 ± 0.03 km/yr) and September 2010–October 2011 (4.4 ± 0.03 km/yr) time frames. The slower phase described by Burgess et al., from January to April 2010, is within the time span of our July 2009–September 2010 velocity field and would explain the overall decrease in ice surface velocity upglacier of the surge front compared to the earlier April 2008–April 2009 velocity field. Downglacier of the surge front in the 2009–2010 velocity field, the ice accelerated to roughly 350 m/yr, compared to values of 15–20 m/yr for previous years. This acceleration is likely due to the close proximity of the surge front to the glacier terminus and the associated increased longitudinal stress transfer downglacier overcoming basal drag near the terminus. In spite of this acceleration, the terminus did not advance, likely due to increased calving into Vitus Lake. In fact, the terminus of Bering Glacier has retreated annually since the end of the previous surge in 1995 (Shuchman et al., 2010). It is only since the surge front reached the terminus in 2011 that the terminus has advanced, roughly 2–4 km (see colored crosses in Figure 1.4).

The results presented here are annual measurements derived from satellite images acquired approximately 1 year apart, and therefore represent an average of the seasonal fluctuations in the surge. Conversely, Fatland and Lingle (1998) used SAR interferometry to measure displacements over 3 days for the 1993–1995 surge and these more closely represent seasonal velocity in Bagley Ice Valley and are not directly comparable to our measurements. However, visual feature tracking (Roush et al., 2003) using 35-day repeat SAR images showed typical ice velocities of 10–20 m/day in the piedmont lobe between August and September 1993. If these rates are extrapolated to an annual velocity (3.7–7.3 km/yr), they are comparable in magnitude to the maximum velocity of the ice presented here, 4.4 ± 0.03 km/yr.

1.5.2 Kinematic Wave

It has been suggested that a surge front represents the transition of the basal hydraulic system from fast, efficient tunnel drainage that promotes ice movement by deformational flow ahead of the front, to a high-pressure linked-cavity system behind the front that promotes flow by sliding (Kamb et al., 1985). Fowler (1987) describes the transition in terms of activation waves that move up- and downglacier from a nucleation point, and he states that the passage of the wave indicates collapse of the tunnel drainage system. Fast-flowing ice behind the surge front that is adjacent to slow-moving ice ahead of the front creates large compressive stress and strain gradients across the surge front that induces an increase in ice thickness. Kinematic wave theory predicts this perturbation in ice thickness will diffuse over time as the wave moves downglacier. Diffusion of the perturbed mass counterbalances the effects of increased ice velocity to stabilize the kinematic wave and produce a wave of constant height that moves with a constant velocity (Johnson, 1968). As shown above, the kinematic wave on Bering Glacier propagates downglacier at an average velocity of 4.4 ± 2.0 km/yr between September 2002 and April 2009, suggesting in this instance that diffusion acts to stabilize the wave, as theorized by Johnson (1968).

The kinematic wave accelerates to 13.9 ± 2.0 km/yr between April 2009 and September 2010. This rate is derived from only two data points and the straight line connecting them has no inherent statistical deviation, such as would be expected with a linear regression through a cluster of points. So we assign the rate the same error bounds as found for the wave speed from 2002–2009. The acceleration of the wave suggests a breakdown of the linear relationship between wave height and speed and replacement by a different response as it enters the piedmont lobe. Several physical variables change from the part of Bering Glacier contained in the valley to the piedmont lobe. The ice is thinnest in the piedmont lobe (Conway et al., 2009), the valley walls diminish so the ice spreads laterally to form a broad fan, the terminus calves into Vitus Lake, so there may be unknown lakewater effects, and the trend of underlying geologic structures changes. The orientation of geologic and topographic structures in the mid- and upper ablation zone causes mountain ridges adjacent to the glacier to plunge beneath the ice creating obstacles to flow. This pattern continues downglacier and into the eastern half of the piedmont lobe. In the western half of the piedmont lobe the trend in geologic structures changes to a north-south orientation, parallel to ice flow (Bruhn et al., 2009). Additionally, the existence of subglacial troughs has been noted in SAR imagery of the piedmont lobe (Bruhn et al., 2009). Exactly how all these physical attributes combine to influence kinematic wave speed is still unknown, but the relationship between wave height and speed has changed from the linear one observed upglacier, to a new, possibly nonlinear relationship in the piedmont lobe.

In this discussion we will refer to the location at which the surge began as the trigger point, or trigger area, and we refer to the location at which the surge front (kinematic wave) began as its nucleation point, or nucleation area. Between 2000 and 2003 airborne laser altimetry data showed there were small acceleration events in the accumulation zone that transferred ice downglacier to the upper ablation zone (Burgess et al., 2012). This formed a reservoir area from roughly the 30 km mark (Figures 1.2 and 1.3) extending upglacier to the confluence with Bagley Ice Valley and eastward into Bagley Ice Valley another 5 km, which Burgess et al. (2012) suggest acted as the trigger area for the first acceleration phase of the 2008–2011 surge. It is probably not a coincidence that our first observation of the kinematic wave in 2001–2002 is located in the reservoir area, because Fowler (1987) predicts the wave will nucleate within a reservoir of ice that exceeds its threshold of stability.

Fowler (1987) also predicts a surge will begin after the kinematic wave has propagated up- and downglacier of the entire reservoir area and its hydraulic system has been activated. Our observations seem to confirm this theory. In the current instance the reservoir extends to roughly the midablation zone by 2007 (cf. Figure 5b, Burgess et al., 2012) and our velocity maps show the kinematic wave in this same region, near the 33 km mark, in 2007. The surge begins the next year in 2008 after the wave has passed downglacier of the reservoir. Roush et al. (2003) place the trigger point in 1993 near the 40 km mark. If it is assumed the 1993–1995 surge was triggered within a reservoir of ice located in the same region as the current surge, then the 1993–1995 surge began downglacier of the reservoir area as well. Roush et al. (2003) also note the surge must have initiated upglacier of the extent of a 26 March 1993 SAR image because all the ice within that image was rumpled. This places the nucleation point for the 1993–1995 surge front at least 50 km upglacier of the terminus, near the confluence of Bering Glacier and Bagley Ice Valley, and in the same general location as our first observation of the surge front in the 2001–2002 velocity field.

The speed of the surge front during the 1993–1995 surge was measured using differential SAR interferometry in winter 1992 and winter 1994 by Fatland and Lingle (1998). They found the surge front celerity to be up to 100 m/day (36.5 km/yr). This rate is significantly greater than the estimates of 4.4 ± 2.0 km/yr and 13.9 ± 2.0 km/yr presented here. Assuming the 1993–1995 and 2001–2010 surge fronts actually moved at similar rates (because of similar trigger and nucleation points), the difference in magnitude between the two surge front propagation rates may illustrate the difference between seasonal and annual measurements and could indicate a seasonal cycle to surge front propagation, faster in late winter and early spring when creep closure pressurizes englacial and subglacial passages, and slower in summer when channelization of subglacial drainage pathways reduces water pressure. This type of seasonal pattern of surge front acceleration and deceleration was observed on Variegated Glacier in 1982–1983 (Raymond, 1987) in which the leading edge of the surge front moved downglacier fastest during April and May, and slowest from July to October. Fatland and Lingle (1998) also note the 1993–1995 surge propagated upglacier into Bagley Ice Valley at 200–500 m/day (73–182 km/yr), much faster than the downglacier rate. Due to limitations of optical feature tracking in snow-covered areas, we do not have velocity measurements in Bagley Ice Valley to constrain the upglacier propagation of the surge and cannot make comparisons with Fatland and Lingle’s observations. Our observations show that a kinematic wave took from 2001 to 2011 to travel approximately 64 km in the ablation zone. Currently no evidence has been presented to show the surge front for the 1993–1995 surge had a similar travel time, but considering the recent surge and the 1993–1995 surge had similar trigger and nucleation areas, it is not unreasonable to think the two events had surge fronts with similar travel times.

1.6 Summary

It has been shown that it is possible to track the build-up and movement of a surge front on a large temperate Alaskan glacier using a combination of repeat image feature tracking algorithms and Landsat-7 ETM+ imagery, including images with scan-line voids. Analysis of the resulting velocity maps, spanning 2001 to 2010, shows the surge front moved downglacier in the form of a kinematic wave with an average velocity of 4.4 ± 2.0 km/yr between September 2002 and April 2009. The small variability in speed of the wave during this time suggests it may have been stabilized by diffusion. The wave then accelerated to 13.9 ± 2.0 km/yr between April 2009 and September 2010 as it entered the piedmont lobe. The surge appears to have climaxed in summer 2011, with the ice velocity approaching 4.4 ± 0.03 km/yr near the terminus. The kinematic wave is estimated to have nucleated near the confluence of Bering Glacier and Bagley Ice Valley as early as 2001, and it took until 2011 to travel roughly 64 km in the ablation zone to the terminus. The surge began in 2008 after the kinematic wave moved downglacier of an ice reservoir area in the midablation zone, suggesting it was triggered there after the reservoir's basal hydraulic system was converted to a high-pressure linked-cavity system.

1.7 Acknowledgements

This project was funded by NASA grants NNX08APZ76 and NNX08AX88G. Thank you to Torborg Heid at the University of Oslo for generously donating her orientation correlation MATLAB program which was used to produce some of the velocity maps in this study. Thank you to Ted Scambos at the National Snow and Ice

Data Center in Boulder, Colorado, for his suggestion to try feature tracking on winter images to avoid the problem of emergent sediment layers in the ablation zone seen in summer images. We also thank the reviewers, including Duncan Quincey, and the editorial staff of Annals of Glaciology whose comments helped to improve this manuscript.

Table 1.1 Pairs of Landsat-7 ETM+ panchromatic imagery and feature tracking search parameters used for Bering Glacier. Search and reference window sizes are the same when using orientation correlation; thus only one size is listed. When using statistical cross-correlation, the search window is larger than the reference window; thus two values are given. The mean georeferencing error is given for each image pair; this value represents the average error in positional accuracy between the images.

Image Dates	Use in this study	Search and reference window sizes (pixels)	Mean georeferencing error between images (m)
April 19, 2001 April 22, 2002	Orientation correlation feature tracking in lower ablation zone	64x64	4.6
Sept. 10, 2001 Sept. 29, 2002	Orientation correlation feature tracking in upper ablation zone	64x64	2.1
April 25, 2003 April 11, 2004	Orientation correlation feature tracking in upper and lower ablation zone	64x64	10.2
Aug. 7, 2006 Aug. 10, 2007	Statistical feature tracking in upper and orientation correlation in lower ablation zone	Upper: 128x128, 32x32 Lower: 64x64	5.2
April 22, 2008 April 1, 2009	Orientation correlation feature tracking in lower ablation zone	256x256	1.3
July 30, 2009 Sept. 19, 2010	Statistical feature tracking in upper and orientation correlation in lower ablation zone	Upper: 128x128, 32x32 Lower: 256x256	5.8
Sept. 19, 2010 Oct. 8, 2011	Manual feature tracking in lower ablation zone	Not applicable	Not applicable

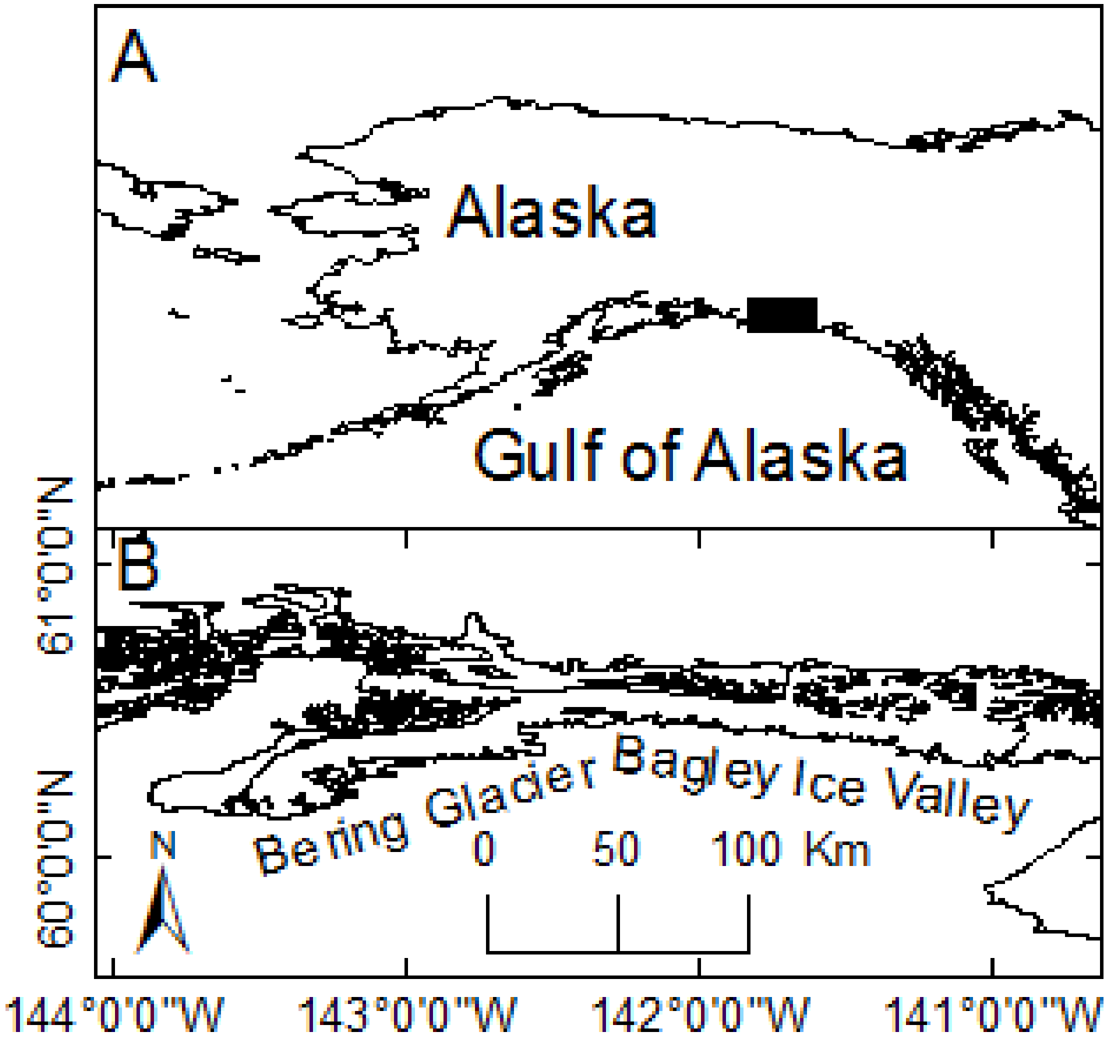

Figure 1.1. A) Location of Bering Glacier. Black rectangle in panel A indicates location of panel B within Alaska. B) Outline of Bering Glacier and Bagley Ice Valley.

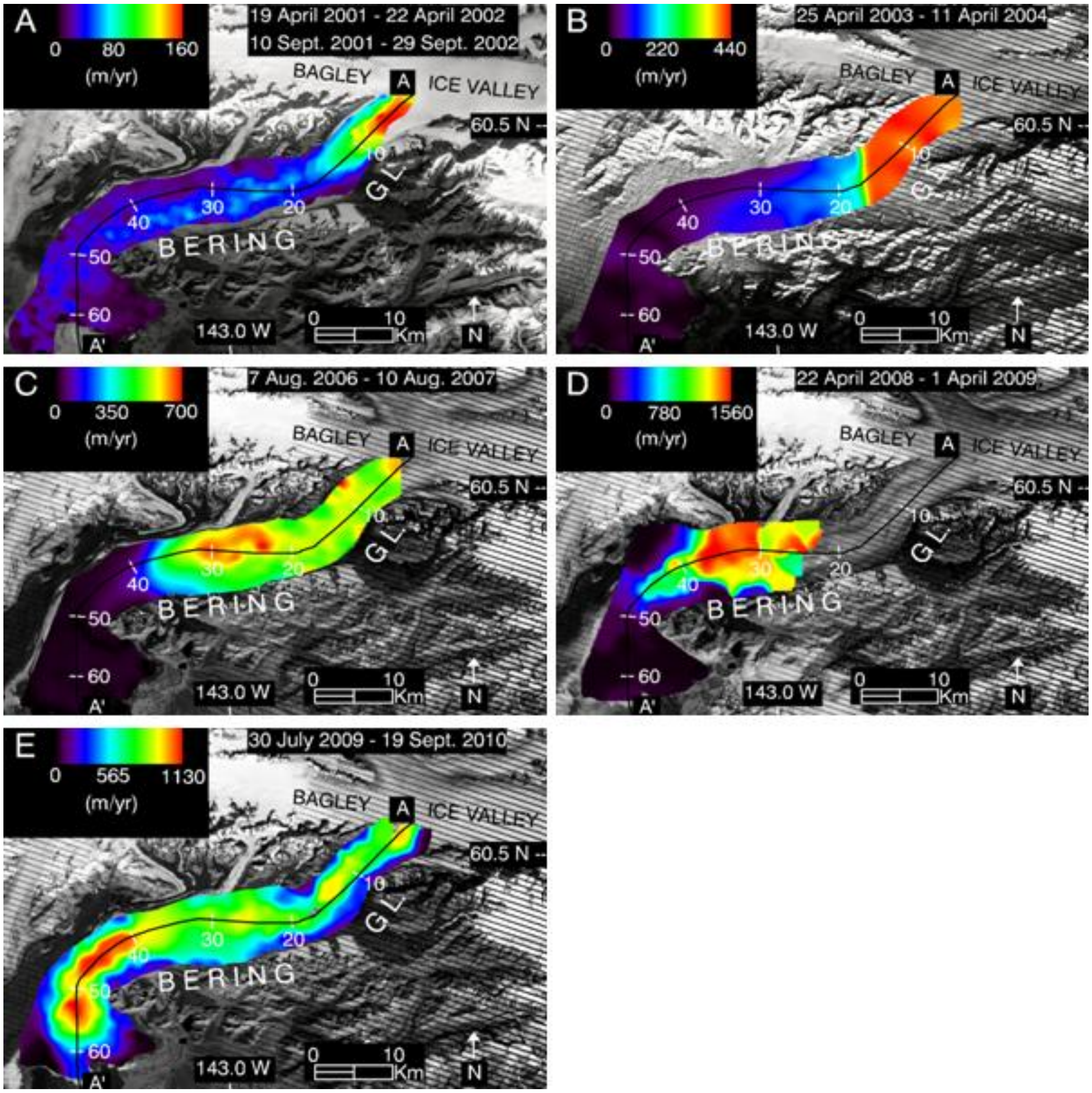

Figure 1.2. Velocity fields for Bering Glacier derived by repeat image feature tracking. A) Lower ablation zone: 19 April 2001 to 22 April 2002. Upper ablation zone: 10 September 2001 to 29 September 2002. B) 25 April 2003 to 11 April 2004. C) 7 August 2006 to 10 August 2007. D) 22 April 2008 to 1 April 2009. E) 30 July 2009 to 19 September 2010. Transect A–A’ within each panel shows location of velocity profiles in Figure 1.3. Note: velocity quantization is different for each velocity field to better highlight the spatial structure within each field.

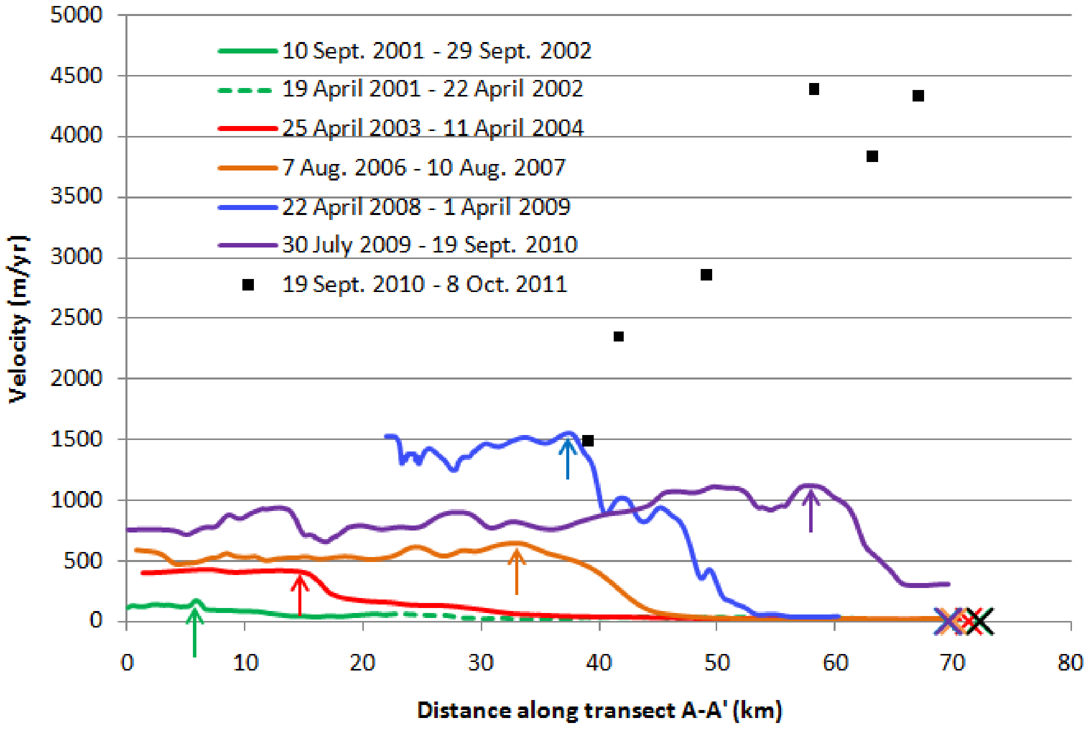

Figure 1.3. Velocity of Bering Glacier along transect A–A' for all five velocity fields (colored lines). The surge front is seen in each profile as a step change in velocity, and the peak of the surge front for each profile is indicated by colored arrows. The changing location of the peak indicates the yearly propagation of the surge front downglacier. The surge front increases in magnitude year-by-year from 2001 to 2009, until in the 2009-2010 profile there is a drop in peak velocity. The surge climax is illustrated by the manually-determined measurements (individual black squares), in which the velocity approaches 4.4 km/yr. Error estimates for velocity are within the line thickness. Colored crosses on the abscissa indicate position of the glacier terminus in the second image for each image pair used to produce the associated velocity profile of the same color.

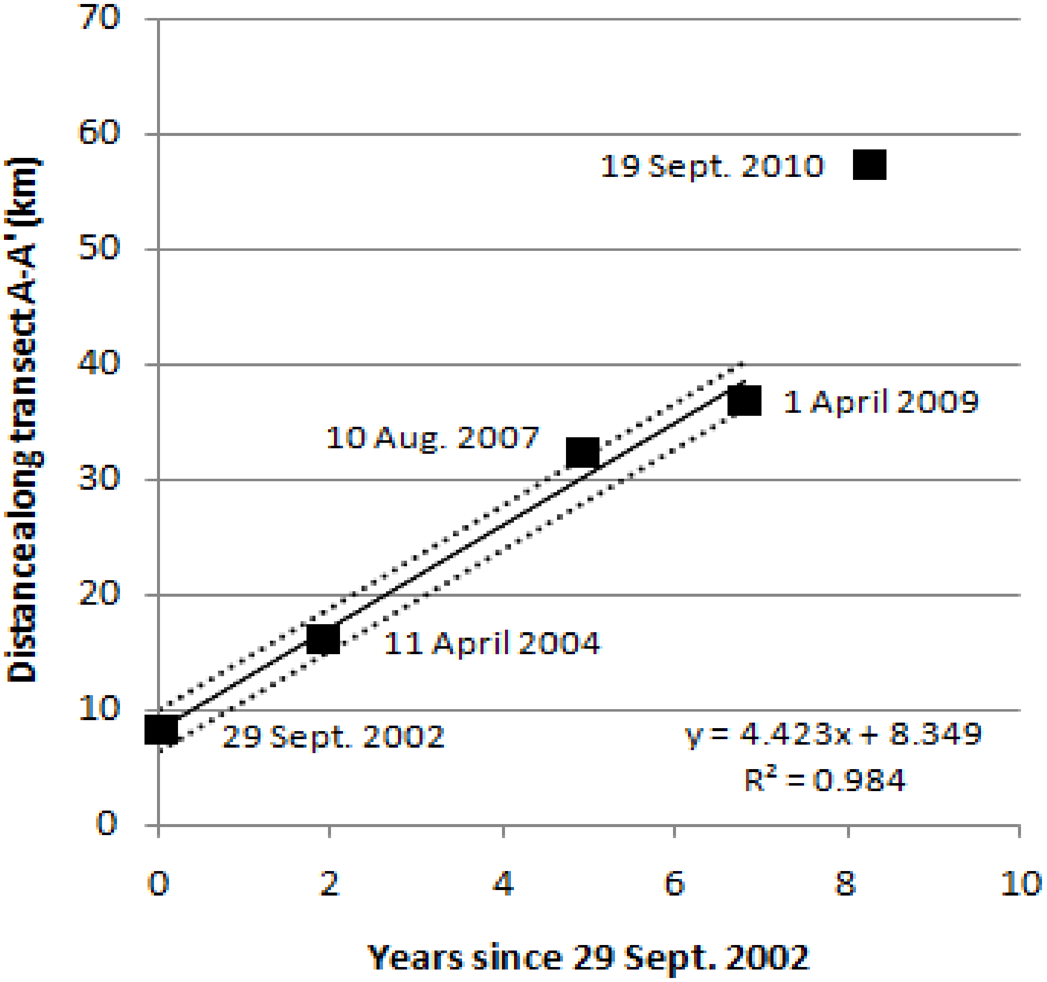

Figure 1.4. Location of the peak of the surge front through time. The abscissa values are the date of the second image within each image pair used to create a velocity field, the date is given next to each point. The ordinate values are the distances of the maximum ice velocity nearest the surge front from the confluence with Bagley Ice Valley. The slope of the solid line fitted through the points from 2002 to 2009 represents the average rate at which the surge front moves downglacier, 4.4 km/yr. Dotted lines represent ±2.0 km/yr, the standard deviation of the surge front speed.

1.8 References

Adalgeirsdóttir, G., Echelmeyer, K. A., & Harrison, W. D. (1998). Elevation and volume changes on the Harding Icefield, Alaska. *Journal of Glaciology*, *44*(148), 570–582.

Ahn, Y., & Howat, I. (2011). Efficient automated glacier surface velocity measurement from repeat images using Multi-Image/Multichip and null exclusion feature tracking. *IEEE Transactions on Geoscience and Remote Sensing*, *49*(8), 2838–2846.

Arendt, A. A., Echelmeyer, K. A., Harrison, W. D., Lingle, C. S. & Valentine, V. B. (2002). Rapid wastage of Alaska glaciers and their contribution to rising sea-level. *Science*, *297*(5580), 382–386.

Berthier, E., Schiefer, E., Clarke, G. K., Menouno, B., & Rémy, F. (2010). Contribution of Alaskan glaciers to sea-level rise derived from satellite imagery. *Nature Geoscience Letters*, doi:10.1038/ngeo737.

Blümcke, A., & Finsterwalder, S. (1905). Zeitliche Änderungen in der Geschwindigkeit der Gletscherbewegung. *Sitzungsberichte der Mathematisch physikalischen Klasse der Königlich Bayerischen Akademie der Wissenschaften*, *35*, 109–131.

Bruhn, R. L., Forster, R. R., Ford, A. L. J., Pavlis, T. L., & Vorkink, M. (2009). Structural geology and glacier dynamics, Bering and Stellar Glaciers, Alaska, in Shuchman, R.A., and Josberger, E.G. eds., *Bering Glacier: Interdisciplinary Studies of Earth's Largest Temperate Surging Glacier*: Geological Society of America Special Paper 462, doi: 10.1130/2009.2462(11).

Burgess, E. W., Forster, R. R., Larsen, C. F., & Braun, M. (2012). Surge dynamics on Bering Glacier, Alaska, in 2008–2011. *The Cryosphere*, *6*(6), 1251–1262.

Conway, H., Smith, B., Vaswani, P., Matsuoka, K., Rignot, E., & Claus, P. (2009). A low-frequency ice-penetrating radar system adapted for use from an airplane: Test results from Bering and Malaspina Glaciers, Alaska, USA. *Annals of Glaciology*, *50*(51), 93–97.

Fatland, D. R., & Lingle, C. S. (1998). Analysis of the 1993–95 Bering Glacier (Alaska) surge using differential SAR interferometry. *Journal of Glaciology*, *44*(148), 532–546.

Fitch, A. J., Kadyrov, A., Christmas, W. J., & Kittler, J. (2002). Orientation correlation, *British Machine Vision Conference*, 133–142.

Fowler, A. C. (1987). A theory of glacier surges. *Journal of Geophysical Research*, *92*(B9), 9111–9120.

Hall, D. K., Giffen, B. A., & Chien, J. Y. L. (2005). Changes in the Harding Icefield and the Grewingk-Yalik Glacier Complex. *62nd Eastern Snow Conference*, Waterloo, Ontario, Canada.

Hance, J. H. (1937). The recent advance of Black Rapids Glacier, Alaska. *Journal of Geology*, *45*, 775–783.

Harrison, A. E. (1956). Glacial activity in the western United States. *Journal of Glaciology*, *2*(19), 675–683.

Haug, T., Kääb, A., & Skvarca, P. (2010). Monitoring ice shelf velocities from repeat MODIS and Landsat data – A method study on the Larsen C ice shelf, Antarctic Peninsula, and 10 other ice shelves around Antarctica. *The Cryosphere, 4*(2), 161–178.

Heid, T., & Kääb, A. (2012a). Repeat optical satellite images reveal widespread and long term decrease in land-terminating glacier speeds. *The Cryosphere, 6*(2), 467–478.

Heid, T., & Kääb, A. (2012b). Evaluation of existing image matching methods for deriving glacier surface displacements globally from optical satellite imagery. *Remote Sensing of Environment, 118*, 339–355.

Herzfeld, U. C., & Mayer, H. (1997). Surge of Bering Glacier and Bagley Ice Field, Alaska: An update to August 1995 and an interpretation of brittle-deformation patterns. *Journal of Glaciology*, *43*(145), 427–434.

Johnson, A. (1953). Nisqually Glacier, Washington (Progress Report), U.S. Geological Survey, 17 p.

Johnson, J. N. (1968). Steady profile of a finite-amplitude kinematic wave on a glacier. *Journal of Glaciology*, *7*(49), 117–119.

Kamb, B., Raymond, C. F., Harrsion, W. D., Engelhardt, H., Echelmeyer, K. A., Humphrey, N., Brugman, M. M., & Pfeffer, T. (1985). Glacier surge mechanism: 1982–1983 surge of Variegated Glacier, Alaska. *Science, 227*(4686), 469–479.

Lee, D. S., Storey, J. C., Choate, J., & Hayes, R. W. (2004). Four years of Landsat-7 on-orbit geometric calibration and performance. *IEEE Trans. on Geoscience and Remote Sensing*, *42*(12), 2786–2795.

Leprince, S., Barbot, S., Ayoub, F., & Avouac, J. P. (2007). Automatic and precise ortho-rectification, coregistration, and subpixel correlation of satellite images, application to ground deformation measurements. *IEEE Transactions on Geoscience and Remote Sensing*, *45*(6), 1529–1558.

Lingle, C.S., Post, A., Herzfeld, U. C., Molnia, B. F., Krimmel, R. M. & Roush, J. J. (1993). Bering Glacier surge and iceberg-calving mechanism at Vitus Lake, Alaska, U.S.A. *Journal of Glaciology, 39*(133), 722–727.

Lingle, C. S., & Fatland, D. R. (2003). Does englacial water storage drive temperate glacier surges? *Annals of Glaciology, 36*(1), 14–20.

Luthcke, S. B., Arendt, A. A., Rowlands, D. D., McCarthy, J. J. & Larsen, C. F. 2008. Recent glacier mass changes in the Gulf of Alaska region from GRACE mascon solutions. *Journal of Glaciology*, *54*(188), 767–777.

Meier, M. F., & Johnson, J. N. (1962). The kinematic wave on Nisqually Glacier, Washington. *Journal of Geophysical Research*, *67*(2), 886.

Molnia, B.F., & Post, A. (2010). Surges of the Bering Glacier. In Shuchman, R.A., and Josberger, E.G. eds., *Bering Glacier: Interdisciplinary Studies of Earth's Largest Temperate Surging Glacier*: Geological Society of America Special Paper 462 doi: 10.1130/2009.2462(11), 291–316.

Post, A. (1969). Distribution of surging glaciers in western North America. *Journal of Glaciology*, *8*(53), 229–240.

Quincey, D. J., Braun, M., Glasser, N. F., Bishop, M. P., Hewitt, K., & Luckman, A. (2011). Karakoram glacier surge dynamics. *Geophysical Research Letters*, *38*(L18504), doi:10.1029/2011GL049004.

Raymond, C. F. (1987). How do glaciers surge? A review. *Journal of Geophysical Research*, *92*(B9), 9121–9134.

Roush, J. J., Lingle, C. S., Guritz, R. M., Fatland, D. R., & Voronina,V. A. (2003). Surge-front propagation and velocities during the early 1993–95 surge of Bering Glacier, Alaska, USA, from sequential SAR imagery. *Annals of Glaciology, 36*(1), 37–44.

Scherler, D., Leprince, S., & Strecker, M. (2008). Glacier-surface velocities in alpine terrain from optical satellite imagery – Accuracy improvement and quality assessment. *Remote Sensing of Environment*, *112*(10), 3806–3819.

Sharp, R. P. (1954). Glacier flow: A review. *Bull. Geological Society of America*, *65*(9), 821–838.

Shekarforoush, M., Berthod, M., & Zerubia, J. (1996). Subpixel image registration by estimating the polyphase decomposition of cross power spectrum. Proceedings: IEEE. *Computer Society Conference on Computer Vision and Pattern Recognition*. San Francisco, CA., USA. June 18–20, 1996.

Shuchman, R. A., Josberger, E. G., Jenkins, L. K., Payne, J. F., Hatt, C. R., & Spaete, L. (2010). Remote sensing of the Bering Glacier Region, in Shuchman, R.A., and Josberger, E.G. eds., *Bering Glacier: Interdisciplinary Studies of Earth's Largest Temperate Surging Glacier:* Geological Society of America Special Paper 462 doi: 10.1130/2009.2462(11).

Tarr, R.S., & Martin, L. (1914). Alaskan glacier studies, chapt. 10. Washington, National Geographic Society.

Vallot, J. (1900). Expériences sur la marche et les variations de la Mer de Glace, *Annales de la Observ. du Mt Blanc*, *4,* 35–157 and 61 plates.

CHAPTER 2[2]

EFFECTS OF BEDROCK LITHOLOGY AND SUBGLACIAL TILL ON THE MOTION OF RUTH GLACIER, ALASKA, DEDUCED FROM FIVE PULSES, 1973–2012

2.1 Abstract

A pulse is a type of unstable glacier flow intermediate between normal flow and surging. Using Landsat Multispectral Scanner System (MSS), Thematic Mapper (TM), and Enhanced Thematic Mapper Plus (ETM+) imagery and feature tracking software, a time-series of mostly annual velocity maps from 1973 to 2012 was produced that reveals five pulses of Ruth Glacier, Alaska. Peaks in ice velocity were found in 1981, 1989, 1997, 2003, and 2010; approximately every 7 years. During these peak years the ice velocity increased 300%, from approximately 40 m/yr to 160 m/yr, and occurred in an area of the glacier underlain by sedimentary bedrock. Based on the spatiotemporal behavior of Ruth Glacier during the pulse cycles, we suggest the pulses are due to enhanced basal motion via deformation of a subglacial till. The cyclical nature of the pulses is theorized to be due to a thin till, with low permeability, that causes incomplete drainage of the till between the pulses, followed by eventual recharge and dilation of the

---

[2] Chapter 2 has been submitted for publication to the *Journal of Glaciology* and is currently in the review process. It is cited in Chapter 3 as Turrin et al. (in review).

till. These findings suggest care is needed when attempting to correlate changes in regional climate with decadal-scale changes in velocity, because in some instances basal conditions may have a greater influence on ice dynamics than climate.

2.2 Introduction

2.2.1 Ruth Glacier

Recently, Heid and Kääb (2012a) produced velocity measurements for nine glaciers in the Alaska Range using optical feature tracking methods and noted only Ruth Glacier had accelerated during the period from 1986-1987 to 2009-2010; the zone of acceleration was restricted to the ablation zone below the Great Gorge and no explanation was offered for this behavior. This unexplained behavior spurred interest in Ruth Glacier and prompted the following research. Ruth Glacier is a 58 km long alpine glacier in the Alaska Range of central Alaska, USA (Figure 2.1), residing in a subarctic continental climate (Shulski & Mogil, 2009) with a predominantly southern aspect. Ruth Glacier has a multilobed accumulation area consisting of a West Fork, Northwest Fork, and North Fork. The headwall of the Northwest Fork reaches 4300 m above sea level and is approximately 4 km from the summit of Mount McKinley, the highest peak in North America. The separate lobes of the accumulation area converge at the head of the Great Gorge, an approximately 12 km long, 1.5–2 km wide valley with 1500 m high steep-sided walls that forms the upper ablation area between the 12 km and 26 km marks (Figure 2.1). In 1983 the ice depth in the Great Gorge was measured using seismic methods and found to be up to 1150 m thick (unpublished data of K. Echelmeyer). The lower ablation area, below the Great Gorge, is approximately 31 km long and 3–4 km wide and ends in a small piedmont lobe roughly 8 km wide, which is partially covered by vegetation. The average ice surface slope within the Great Gorge is 2.6°, and below the gorge the average ice surface slope is half as much, 1.3°, per the National Elevation Dataset (Gesch et al., 2009). At the base of the Great Gorge there is some crevassing where the ice exits the gorge; the rest of the ablation area is free of major crevassing (as seen in the 30-m Landsat imagery used in this study), but the medial moraines exhibit a slightly wavy pattern. The Great Gorge, and parts of the West Fork, Northwest Fork, and lower ablation area are underlain by Tertiary (Paleocene) biotite-muscovite granite and quartz monzonite of the McKinley Sequence (delineated by the red polygons and denoted by the symbol Tpgr in Figure 2.1; Gamble & Reed, 1996; Reed & Nelson, 1980). The North Fork and the ablation area immediately below the Great Gorge are underlain by sedimentary rocks from the Cretaceous and Jurassic periods (denoted as KJf in Figure 2.1). These rocks are part of the Kahiltna Flysch sequence and are comprised of argillite, fine to coarse greywacke, conglomerates, and thin layers of chert and limestone (Csejtey & others, 1992; Reed & Nelson, 1980). Part of the piedmont lobe is underlain by Tertiary (Miocene) sedimentary bedrock comprised of sandstone, siltstone, shale, and claystone of the Tyonek Formation (delineated by the yellow dotted polygon and denoted as Tty in Figure 2.1), which is part of the Kenai Group (Solie et al., 1991).

Little has been published concerning Ruth Glacier. Mayo (1978) notes Ruth Glacier is a pulsing glacier and mentions the existence of small potholes in its surface that are the remnants of large crevasses. Hall and Ormsby (1983) examined Ruth Glacier using Landsat MSS and Seasat synthetic aperture radar data from the summer of 1978 and noted the firn zone was located within the Great Gorge. Burgess et al. (2013) used synthetic aperture radar offset tracking to measure the wintertime speed of all glaciers in the Alaska Range during the late 2000s; the exact year is not given for each glacier, varying from 2007 to 2010. It was found that Ruth Glacier was moving at 0.6 to 1.0 m/day (219 to 365 m/yr) in the Great Gorge, with the ice gradually decelerating from approximately 0.5 m/day (182.5 m/yr) immediately below the Great Gorge to being stagnant at the terminus. Ward et al. (2012) note the igneous bedrock (Tpgr) of the Denali massif is significantly less fractured than the surrounding tectonically deformed sedimentary bedrock (KJf and Tty). Fracture spacing in the granitic bedrock is on the order of decimeters to hectometers, while fracture spacing in the sedimentary bedrock is on the order of centimeters to decimeters. This difference in fracture spacing causes a large difference in rates of glacier erosion (plucking) between the two predominant bedrock types. The result is that the valley in which Ruth Glacier resides tends to be narrow, with steep-sided walls (often 60° or greater in slope) in regions underlain by the granitic bedrock (e.g., the Great Gorge and between the 41 and 48 km marks), and the valley tends to be wider with shallow-sloped walls (often 45° or less) when underlain by sedimentary bedrock (Ward et al., 2012). Thus, the geometry of the glacier, and consequently ice thickness and basal shear stress, are dictated partly by the underlying bedrock type.

2.2.2 Pulsing Glaciers

Mayo (1978) defines glacier pulses as periodic unstable flow that is lesser in magnitude than surges, and therefore, pulsing glaciers are intermediate between normal and surging glaciers. Pulsing glaciers may be identified by the existence of characteristic wavy medial moraines, large-scale wavy foliation, or boudinage that may be present on only part of the glacier, indicating only part of it pulses. If the characteristic pattern is continuous, it is suggested the glacier experiences regular, periodic pulses. Mayo (1978) noted that potholes (remnants of crevasses) probably form in the zone of ice loss on pulsing glaciers. Approximately 140 glaciers in Alaska have been identified with these characteristics in aerial photography from the 1960s and 1970s by Austin Post and L. R. Mayo. Most of these pulse-type glaciers occur in the same regions as surge-type glaciers, in the Alaska Range, Chugach Mtns., St. Elias Mtns., and Wrangell Mtns. Pulsing behavior may occur in conjunction with the drainage of large glacier-dammed lakes, suggesting a link between basal hydrology and pulsing flow. Mayo (1978) lists some pulsing glaciers and the dates of their observed pulses: West Gakona Glacier (1949), Nizina Glacier (1961), Trident Glacier (1970, 1971), MacLaren Glacier (1971, 1972), and Tokositna Glacier (1971, 1972). Additionally, undated pulses are listed for: Capps Glacier, Eureka Glacier, Hayes Glacier, Kahiltna Glacier, Miles Glacier, Ruth Glacier, Sanford Glacier, and the West Branch of Sheridan Glacier.

Sometime between 1974 and 1977 Trapridge Glacier, Yukon Territory, Canada, began a prolonged surge that lasted until 2005 (Frappé & Clarke, 2007). During the surge a string of five 4-year pulses were detected from 1981 to 2002, with amplitudes of roughly 10 m/yr, a 33% increase in velocity. Trapridge Glacier is a polythermal glacier with temperate upper ice and subzero basal ice, and it is underlain by a deformable, permeable till up to 10 m thick (Blake et al., 1992; Stone, 1993). Increased ice velocity during the surge, and by inference during the pulses, is attributed to sliding at the bed caused by failure of the basal till. Till failure reduces basal friction and transfers stress laterally to the glacier margins, thereby producing an area of plug-flow along the central portion of the glacier, allowing ice there to accelerate. During a similar time frame, from approximately 1980 to 2002, Black Rapids Glacier, a temperate glacier in the central Alaska Range (Harrison et al., 1975), experienced two consecutive 12-year pulses, with amplitudes of roughly 20–25 m/yr, representing velocity increases of 55–65% (Nolan, 2003). Black Rapids Glacier is underlain by a till 5–7 m thick (Nolan & Echelmeyer, 1999), and it has been shown via borehole tiltmeter measurements that up to 70% of the ice velocity during the pulses was due to deformation within the till at depths >2 m below the ice/till interface (Truffer et al., 2000). Again, it was theorized that till failure reduced stresses in the center of the glacier and transferred them towards the margins. This process promotes increased basal motion along the glacier centerline and increased ice deformation near the margins (Nolan, 2003; Truffer et al., 2001).

Ice dynamics influence the length, area, and volume of a glacier. Changes in ice dynamics, therefore, necessarily result in changes in the geometry of a glacier, which in turn affects its mass balance. For example, pulses and surges may rapidly transfer ice to lower altitudes where it is subject to increased air temperature and ablation, thereby promoting a reduction in mass balance. Knowing that dynamic instabilities such as pulses and surges are intimately tied to the basal conditions of a glacier, an improved understanding of the relationship between basal conditions and ice dynamics will further our understanding of the influences on a glacier’s mass balance. In this study we will examine the cyclical dynamic behavior of Ruth Glacier to determine the amplitude, frequency, and spatial extent of its pulses. Based on the spatial and temporal structure of the velocity fields during multiple pulse cycles, we will infer the basal conditions beneath Ruth Glacier and describe the influence of bedrock lithology on the behavior of its pulses.

2.3 Methods

2.3.1 Optical Feature Tracking

Optical feature tracking methods were used to produce a time-series of ice surface velocity maps spanning 1973–2012 for Ruth Glacier in order to delineate its periodic dynamic behavior. COSI-Corr feature tracking software (Leprince et al., 2007) was used in conjunction with Landsat MSS, TM, and ETM+ imagery to produce the velocity maps (see Table 2.1 for image dates). COSI-Corr was chosen due to its proven precision (Heid & Kääb, 2012b; Scherler et al., 2008), its ability to produce accurate displacement measurements in areas of low contrast or with light cloud cover (Heid & Kääb, 2012b), and its ease of use. COSI-Corr produces an initial estimate of the displacement of features between sequential images by use of the Fourier shift theorem which states the displacement is found in the phase portion of the normalized cross power spectrum computed from the Fourier transform of each image (Shekarforoush et al., 1996). Equal-sized subsets from each image centered on the same pixel, called reference and search windows, corresponding to the temporally first and second images, respectively, are matched to one another and a displacement measurement produced with 1-pixel accuracy. A reweighted least squares phase minimization algorithm is then applied to determine the final displacement. This algorithm minimizes the phase difference between the initial displacement estimate and an ideal theoretical one, thus producing subpixel accuracy. This process is repeated in a grid-like pattern across the entire image, producing individual displacement measurements at predefined intervals. The displacement measurements (vectors) produced by COSI-Corr are postprocessed using a neighborhood analysis routine to remove erroneous vectors. Any vector that is more than ±2 standard deviations away from the mean magnitude or direction of its local neighborhood, consisting of at least nine adjacent vectors, is deemed an anomaly and removed. Afterwards, the vector field is visually inspected and any remaining anomalies are manually removed. The individual vectors are interpolated using a linear inverse-distance weighting scheme to produce a velocity raster. In May, 2003, the Scan-Line Correction (SLC) mirror of Landsat-7 ETM+ failed, resulting in data voids in images acquired afterwards; these images are commonly called SLC-off images. Fortunately, the portion of Ruth Glacier in which the pulses are tracked (the ablation zone below the Great Gorge) lies near the center of the Landsat-7 images where the data voids do not exist. Therefore, more advanced feature tracking techniques, such as Ahn and Howat's (2011) null exclusion method or orientation correlation (Fitch et al., 2002; Haug et al., 2010) were not necessary when using SLC-off images for Ruth Glacier.

2.3.2 Accuracy

The accuracy of the velocity fields produced from feature tracking algorithms depends on the precision of the matching method and how well the two images being matched are aligned to one another. Heid and Kääb (2012b) evaluated the precision of COSI-Corr using Landsat-7 ETM+ 15-m panchromatic imagery and found the Root Mean Square Error (RMSE) of its displacement measurements to be ±0.9 m in the x-direction and ±0.8 m in the y-direction, for a total RMSE of ±1.2 m, or ±0.08 pixels. If we apply this same error (±0.08 pixels) to 30-m imagery, the expected error is ±2.4 m, and for 60-m imagery the expected error is ±4.8 m. Storey and Choate (2004) have shown the RMSE of the geometric accuracy of Landsat-5 TM data is ±5.5 m (±0.2 pixels), and Lee et al. (2004) showed the average geometric error of Landsat-7 ETM+ imagery is less than ± 5 m ($\pm 0.1\overline{6}6$ pixels). Table 2.2 (last column) shows the listed

RMSE of the geometric accuracy for each Landsat image used in this study, upon receipt from the U.S. Geological Survey; the mean of the 22 values for TM/ETM+ images is 0.16 ± 0.04 pixels (4.8 ± 1.2 m; mean ± 1 standard deviation), which compares well with the values given by Storey and Choate (2004) and Lee et al. (2004). For the 12 MSS images, the mean geometric error is 0.47 ± 0.12 pixels (28.2 ± 7.2 m).

For each image pair vectors on dry, snow-free, cloud-free land were analyzed to determine the mean georeferencing error between the two images (Table 2.2). The average of these mean georeferencing errors is 0.22 ± 0.09 pixels (7.0 ± 3.0 m) for 30-m TM and ETM+ imagery and 0.45 ± 0.15 pixels (24.1 ± 6.7 m) for MSS imagery (Table 2.3). The mean georeferencing error for each image pair was subtracted from the on-ice vectors to improve the accuracy of the velocity fields. The mean georeferencing error was also subtracted from the off-ice vectors, resulting in a residual error between images which represents their final misalignment (Tables 2.2, 2.3). We note the average of the mean residual errors for the TM/ETM+ image pairs, 0.15 ± 0.07 pixels (4.9 ± 2.6 m), compares well with values quoted above by Storey and Choate (2004), Lee et al. (2004), and with the mean geometric accuracy for an individual image. Thus, after removal of the mean georeferencing error, the TM/ETM+ image pairs are aligned to one another as precisely as each individual image is aligned to the ground control points used to geolocate it. We also note the image-to-image misalignment for each TM/ETM+ image pair is within 1 standard deviation of the precision of COSI-Corr (±0.08 pixels), which suggests that after removal of the mean georeferencing error the residual misalignment of the TM and ETM+ image pairs approaches the limits of detection by COSI-Corr. The mean georeferencing error for MSS data, as measured by COSI-Corr (Table 2.3) is 0.45 ± 0.15 pixels (24.1 ± 6.7 m), and after removal of this error, the residual image-to-image misalignment is 0.25 ± 0.07 pixels (14.1 ± 4.2 m). Thus, after removal of the georeferencing error, the MSS image pairs are aligned more precisely to one another than each individual image was originally aligned to its ground control points upon receipt from the U.S. Geological Survey (compare the average residual error of 0.25 pixels to the average geolocation error of 0.47 pixels). Using the root sum of squares method, we estimate the combined error in the velocity fields, resulting from the mean residual error and COSI-Corr's precision, to be 5.1 m (0.17 pixels) for the 30-m Landsat TM/ETM+ data, and 15.7 m (0.26 pixels) for the 60-m Landsat MSS data.

2.4 Results

COSI-Corr was unsuccessful in producing reliable displacement measurements within the Great Gorge and in the accumulation area due to snow cover and a lack of surface features to track, but it was quite successful below the Great Gorge. A time-series of 29 velocity maps (Figures 2.2 to 2.5) shows the evolution of the pulses of Ruth Glacier in time and space, below the Great Gorge. From 1973–1974 to 1976–1977 (Figure 2.2a–c) much of the ablation area below the Great Gorge is moving at 75 m/yr or less. Then in 1977–1978 (Figure 2.2d) the ice down to the 30 km mark accelerates to almost 200 m/yr. In 1978–1980 (Figure 2.2e) the ice between the 35 km and 40 km marks has accelerated relative to previous years, and by 1980–1981 (Figure 2.2f) all the ice down to the 45 km mark has accelerated, much of it moving 150 m/yr or more, indicating a doubling of ice velocity compared to the period from 1973 to 1977. From 1981–1982 (Figure 2.2g) to 1983–1984 (Figure 2.3a), the glacier gradually decelerates and returns to its prepulse velocity. In Figure 2.3 there are two pulses evident between 1984–1985 and 1995–1999 that show a similar pattern of gradual acceleration and deceleration of the ice, with peak velocities in 1987–1991 (Figure 2.3e) and 1995–1999 (Figure 2.3h). Due to lack of cloud-free imagery between 1987 and 1991, and lack of data acquisition during the late 1990s, these pulses are not well defined in time, but it is clear the two pulses did occur due to the increased velocities during these 4-year time spans. From 1999–2000 to 2001–2002 (Figure 2.4) the cyclical pattern has continued, with a gradual increase in velocity from roughly 50–75 m/yr in 1999–2000 (Figure 2.4a) to >100 m/yr in 2001–2002 (Figure 2.4c) between the 26 and 35 km marks. By 2002–2003 (Figure 2.4d) velocity reached a peak, with characteristic values of 150–200 m/yr between the 26 and 42 km marks, indicating the ice has more than doubled its speed compared to 3 years earlier. Afterwards, the ice decelerates to its prepulse velocity by 2005–2006 (Figure 2.4g). A fifth pulse is evident in Figure 2.5, which shows an acceleration of the ice from 2006–2007 (Figure 2.5a) to 2009–2010 (Figure 2.5d), with the peak occurring in 2009–2010, followed by deceleration in 2010–2011 and 2011–2012 (Figure 2.5e, f). Characteristic peak ice velocities during this last pulse, between the 26 and 42 km marks, are 150–200 m/yr, indicating a three- to four-fold increase in velocity compared to 2006–2007.

To help illustrate the evolution of the pulses through time, the velocity at two points along the glacier, 36 km and 43 km, are plotted in Figure 2.6. This graph clearly illustrates the periodic nature of the pulses and highlights the five individual peaks. It should be noted that for plotting purposes, velocity was assigned to the second year of each image pair used to produce a velocity field, or in the case of the 1987–1991 and 1995–1999 velocity fields, velocity was assigned to a middle year, 1989 and 1997, respectively. This scheme is employed (rather than assigning velocity to a particular day between image acquisition dates) so the plot of velocity versus time in Figure 2.6 has consistent units, meters-per-year versus year. Inspection of this graph yields characteristic pulse amplitudes (peak value minus trough value) in excess of 120 m/yr (a 300% increase in velocity) at the 36 km mark, and 60–70 m/yr (a 50–75% increase in velocity) at the 43 km mark for the 1981, 2003, and 2010 peaks. The amplitudes of the 1989 and 1997 pulses are not as great as the amplitudes of the other pulses. We infer this to be because their respective velocity fields were produced using image pairs spanning 4 years, thus their peak velocity values are averaged with surrounding years of lesser velocity, resulting in lower amplitudes. Based on the occurrence of the peaks as described here, the pulses of Ruth Glacier have a characteristic period of approximately 7 years.

To further aid in analyzing the pulses, longitudinal profiles of velocity, acceleration, and strain rate were produced for each velocity field (Figures 2.7–2.10). The longitudinal velocity and acceleration profiles in Figures 2.7a and 2.7b clearly show the extent of the pulse from 2009 to 2011. All the ice below the Great Gorge down to roughly the 52 km mark noticeably accelerated during this time. It is worthwhile to note that in the area of the 27 km mark, the 40–42 km marks, and the 49 km mark, there are inflections in velocity and acceleration, and prominent peaks (or troughs) in strain rate in 2009–2010, 2010–2011, and 2011–2012. The location of these inflections, peaks, and troughs approximately coincide with the transition from granitic to sedimentary bedrock at the 28 km mark, a change from sedimentary to granitic bedrock at the 41 km mark, and a change back to sedimentary bedrock at the 48 km mark, as seen in Figure 2.1. Examination of the acceleration profiles (Figure 2.7b) reveals the ice from the 26 km mark to roughly the 50 km mark accelerates (in varying amounts) simultaneously; there is no evidence of a wave front propagating downglacier. The strain rate between the 37 and 43 km marks changes from predominantly compressive before the pulse, to tensile during the pulse, and back to compressive afterwards; again, indicating the ice in this area is responding simultaneously to applied stresses. The longitudinal profiles in Figure 2.8 span the years 1999 to 2006 and highlight the behavior of Ruth Glacier immediately before, during, and after the 2002–2003 pulse. As with the 2009–2010 pulse, there are noticeable inflections in velocity and acceleration, and noticeable peaks or troughs in strain rate, near the transitions between granitic and sedimentary bedrock at 28 km, 41 km, and 48 km. Again, it is evident that the entire stretch of ice between 26 and 50 km has accelerated simultaneously, and the same pattern of changing strain rate, from compressive to tensile, and back to compressive, is evident before, during, and after the pulse, respectively. The 2003–2004 acceleration profile (Figure 2.8b) shows a well-defined area of acceleration between the 42 and 50 km marks, atop granitic bedrock; this same area also increased in acceleration in 2010–2011 (Figure 2.7b) while the rest of the ice upglacier decelerated. Both of these acceleration events occurred 1 year after, and downglacier, of the peak pulse events in 2003 and 2010, which occurred atop sedimentary bedrock. Figure 2.9 shows the longitudinal profiles for the years surrounding, and including, the 1987–1991 and 1995–1999 pulses. Although these two pulses are not as well defined as the 2002–2003 and 2009–2010 pulses, the same patterns are still evident. There are inflections in the velocity and acceleration profiles (Figure 2.9a,b), and peaks or troughs in the strain rate (Figure 2.9c), near the same locations as the later pulses, at 26 km, 40–42 km, and 50 km. Again, large portions of the ice between the 26 and 50 km marks accelerate and decelerate in unison. During the 1987–1991 and 1995–1999 pulses, there is no obvious acceleration of the ice between the 42 and 50 km marks (Figure 2.9b; as seen in the later pulses [Figure 2.7b, 2.8b]), probably due to the poor temporal resolution of these two pulses. Lastly, Figure 2.10 shows the longitudinal profiles for the years surrounding, and including, the 1980–1981 pulse. Again, inflection points in the velocity and acceleration profiles are seen at, or near, the 26 km, 40–42 km, and 50 km marks (Figure 2.10a, b), but the pattern of peaks and troughs in strain rate seen in the other pulses is not clear.

2.5 Discussion

To place our results in context with other surging and pulsing glaciers, we briefly discuss till deformation and flow instabilities with regards to glacier dynamics. In turn, these discussions help identify the likely basal conditions of Ruth Glacier during its pulses.

2.5.1 Glacier Motion by Till Deformation

The location of surging glaciers in Svalbard is positively correlated with areas of fine-grained sedimentary bedrock, which are easily eroded (Jiskoot et al., 2000), while in NW North America surging glaciers are often found in fault-shattered valleys (Post, 1969). Glaciers atop these areas are more likely to develop a soft bed than when atop intact crystalline metamorphic or igneous bedrock. Sedimentary bedrock will produce a fine-grained till that will have a low permeability which may be more prone to instabilities (Murray & Porter, 2001). Instability within a till may develop due to decreased effective pressure, via increased basal water input. As long as the discharge of water at the glacier bed is small, steady-state water pressure will approximate ice overburden pressure and the water will flow by Darcian transport through the till, or by a uniform water film at the base of the ice, and the till will remain consolidated. When pore-water pressure in the till equals or exceeds ice overburden pressure the till weakens and may dilate (Willis, 1995). Dilation of the till causes porosity and permeability to increase, thus decreasing water pressure and shear strength (Murray, 1997). When a till dilates it can no longer support shear stress and it deforms, allowing the glacier to accelerate. The increased ice motion may occur as slip at the ice/till interface in which shear strain in the till occurs in the uppermost layer of sediment. Shear strain may also occur within the till along a plane of weakness, or it may be distributed throughout the till by the process of dilatant hardening. When a till dilates, the pore volume increases, allowing water to flow towards the opening pores in the dilating sediment. If the rate of dilation is greater than the rate of pore-water flow then water pressure will decrease in the dilated sediment and it will harden (Reynolds, 1885). When the shear band hardens, the strain is focused elsewhere within the till; thus, the strain is distributed from one plane of weakness to the next.

Truffer et al. (2000) suggested surges could be triggered by widespread dilation of basal till as shear stresses exceed a critical value, along with attainment of a glacier geometry that produces large basal shear stresses. Failed tills are concentrated under thicker ice, such as along the glacier centerline, where driving stress is greatest and may exceed till yield strength. Nolan (2003), when investigating the behavior of Black Rapid Glacier, proposed the idea of waves of till failure (activation waves) that propagate underneath a glacier as follows: 1) Failed till along a section of glacier centerline causes increased stress laterally and longitudinally because the driving stress is redistributed elsewhere; 2) The glacier speed increases locally due to failed till; 3) When the driving stress is distributed elsewhere, any till that was at, or near, a point of failure will fail, thus increasing the area of the glacier with increased speed; 4) This process creates a wave of till failure and subsequent ice motion that propagates downglacier via a positive feedback loop by continuously placing increased stress on the downglacier till; 5) As the area of failed till increases longitudinally, the glacier moves faster everywhere because of reduced bed friction and greater basal motion. A similar mechanism was discussed by Frappé and Clarke (2007) to explain the behavior of Trapridge Glacier. The till deformation paradigm allows glacier velocity to increase greatly without requiring large changes in glacier geometry or the subglacial hydraulic system, assuming the till is near its failure threshold (Truffer et al., 2001).

Fowler et al. (2001) noted that if the till layer has a low transmissivity (i.e., the till is thin) and low permeability then oscillations in effective pressure, ice thickness, and ice flux can occur. Ice speed during a pulse depends primarily on basal roughness. If the basal roughness is large, then ice flow is sufficiently restricted to allow oscillatory behavior to occur; otherwise, a major surge can occur if the basal roughness is small, because there is little restriction to ice flow. Fowler et al. (2001) also suggest that if a glacier is temperate and resides atop a thin till, the ice may activate (i.e., the till fails beneath it) before any significant ice motion because the activation waves are faster than the ice motion; so, the ice slumps forward rapidly moving as a block, or plug. Therefore, there is no surge front that would otherwise separate fast-moving surging ice and slow-moving quiescent ice. Plug flow has been observed on Black Rapids Glacier (Harrison & Post, 2003) and Trapridge Glacier (Frappé & Clarke, 2007), both of which have surged atop a till. Once a surge has been initiated by till failure, less stress is required to keep the till in a failed state, allowing the surge to continue. This occurs because drag at the glacier base increases longitudinal shear stress that might cause a till to fail even when water pressures are less than the critical Coulomb threshold (Boulton et al., 2001). The accelerated ice motion will cease when the ice can no longer be shoved forward by driving stresses, either by obstacles restricting down glacier movement or by decreased upglacier stresses, then the basal shear stress decreases below the till failure point and the till heals. Additionally, the accelerated ice motion will cease if drainage of water from the till occurs, reducing water pressure and allowing the till to heal. However, a till with low permeability may not drain completely; thus, the till may not fully heal and it is left primed for another pulse episode when enough water is introduced again (Nolan, 2003). A thin till, which has lesser water storage capacity than a thick till, will refill quickly and surpass its Coulomb failure threshold sooner than a thick till would, resulting in more frequent pulses.

2.5.2 Basal Conditions beneath Ruth Glacier

Knowing that the sedimentary bedrock beneath Ruth Glacier is highly fractured and easily eroded, and the fact that Ruth Glacier exhibits a dynamic behavior similar to other glaciers known to reside atop deformable tills by accelerating and decelerating in a cyclical, plug-like fashion, it seems likely a deformable till exists beneath Ruth Glacier between the 28 km and 41 km marks. The area from the 41 km mark to the 48 km mark is underlain by granitic bedrock that will not as readily erode to produce a till, but there is likely some sediment beneath the glacier in this area that was transported from above, but which is spatially sparse and does not promote widespread increased ice motion via till dilation and deformation. The fact that the ice in this area (lying atop the granitic bedrock) has accelerated during the pulses, although to a lesser degree than ice atop sedimentary bedrock, is likely due to stress transfer and longitudinal coupling with the ice upglacier (note the lesser velocity at the 43 km mark in Figure 2.6 compared to the 36 km mark). The inferred existence of a deformable till requires the basal ice and the till to be at the pressure-melting point; therefore, we conclude the base of Ruth Glacier is temperate (its ice is at the pressure-melting point) below the Great Gorge. The simultaneous acceleration of the ice from the 26 km mark, immediately below the Great Gorge, to roughly the 50 km mark provide further evidence that Ruth Glacier is warm-based in this area. In addition, Fowler et al. (2001) theorize temperate glaciers atop deforming tills will slump forward without formation of a wave front, thus a lack of a wave front provides further proof that Ruth Glacier is temperate below the Great Gorge. The lack of a wave front is in contrast to observations of typical Alaska-style surging glaciers wherein a surge front separates quiescent ice from surging ice, as noted on Variegated Glacier (Kamb et al., 1985) and Bering Glacier (Roush et al., 2003; Turrin et al., 2013). The dynamic oscillating (pulsing) behavior of Ruth Glacier suggests the till is thin with a low permeability (Fowler et al., 2001).

2.5.3 Distinguishing Pulses from Surges

Alaska-style surges are controlled by the morphological evolution of the basal drainage system beneath temperate ice from a channelized system to a distributed cavity system (Kamb et al., 1985) and are traditionally assumed to occur atop a hard bed. Svalbard-style surges are controlled by the thermal evolution of the basal ice from sub-freezing to temperate (Fowler et al., 2001; Murray et al., 2003) and occur atop a soft bed (a basal till). Both Alaska-style and Svalbard-style surges can result in a surge front (kinematic wave) moving downglacier that separates quiescent ice, moving primarily by internal deformation of the ice column, from surging ice that moves primarily by slip at the ice/bed interface, or by deformation within a basal till (in the case of a Svalbard-style surge). Pulses are controlled by the evolution of the basal till from a healed state to a dilated state, and occur where the base is at the pressure-melting point. If the till beneath

Ruth Glacier froze between pulses, then a surge front would form in the manner of a typical Svalbard-style surge during each pulse, but the lack of any wave front suggests the base is perennially temperate. As noted above, Trapridge Glacier experienced five low-amplitude pulses during a prolonged surge (Frappé & Clarke, 2007), and Black Rapids Glacier, also a surge-type glacier, experienced two low-amplitude pulses during quiescence (Nolan, 2003). These studies suggest pulsing is a dynamic behavior apart from typical surging that may occur either during an active, low-amplitude surge or during quiescence. Ruth Glacier is not known to surge in the traditional sense, so pulsing may also occur on glaciers other than surge-type that have the requisite temperate base and till, and adequate shear stress and basal water pressure to dilate the till.

2.5.4 Implications for Decadal-scale Velocity Measurements

As mentioned above, Heid and Kääb (2012a) noted Ruth Glacier accelerated between 1986-1987 and 2009-2010. This perceived acceleration is a result of the years chosen for use in their velocity determinations. The 1986-1987 period falls between pulses, while the 2009-2010 period is at the peak of a pulse (Figure 2.3); thus, there is a perceived acceleration of >120 m/yr during this period. If one had instead chosen images acquired in 1980-1981 and 2007-2008 and performed the same analysis, the result would be a deceleration of >-120 m/yr, the opposite of what Heid and Kääb (2012a) reported. In either case, the pulses which occurred during the interval between velocity measurements are missed. Optical feature tracking methods have now matured to the point where decadal-scale regional, and perhaps global, studies of ice dynamics are possible, as exemplified by Heid and Kääb (2012a). When performing such work, it is important to be aware of any surging or pulsing glaciers in the chosen study area and how their periodic behavior might affect results. In some instances, such as on Ruth Glacier, basal conditions may exert a greater influence on ice dynamics than regional changes in climate on annual and decadal time frames.

2.6 Conclusions

From 1973 to 2012, a span of 39 years, Ruth Glacier experienced five pulses that have gone unnoticed until now. These pulses are of low amplitude compared to typical surges of glaciers in Alaska, and they occur without causing an advance of the terminus and without widespread crevassing, perhaps helping to explain their oversight. The pulses have occurred on a regular basis, approximately every 7 years, with peaks in 1981, 1989, 1997, 2003, and 2010, and with increases in ice velocity of >120 m/yr during the peaks in 1981, 2003, and 2010. The pulses occur in an area of the glacier underlain by sedimentary bedrock, and we suggest that the pulses are a result of enhanced basal motion due to deformation of a subglacial till. Therefore, we infer that the base of Ruth Glacier, in the area in which the pulses occur, must be temperate. Additionally, theory predicts that the manner in which the glacier moved during the pulses, with a 20 km section of ice accelerating and decelerating in unison, and the lack of a wave front, is suggestive of a perennial temperate base (Fowler et al., 2001). The oscillating dynamic behavior is theorized to be due to a thin till with low permeability that is just above a critical value (Fowler et al., 2001). The basal roughness is theorized to be great enough to restrict ice flow and prevent the occurrence of major surges. These findings illustrate the influence of bedrock lithology and a glacier’s basal thermal regime on its dynamics, the combination of which will ultimately affect its mass balance.

2.7 Acknowledgements

This project was funded by NASA grants NNX08APZ76 and NNX08AX88G. We thank Peter Haeussler of the U.S. Geological Survey for providing information on the geology of the Mount McKinley area.

Table 2.1. Landsat imagery for Ruth Glacier.

Image date	Sensor	Spatial resolution (m)
24 Sept. 1973	MSS 1	60
27 July 1974	MSS 1	60
23 Sept. 1975	MSS 2	60
7 July 1976	MSS 2	60
1 July 1977	MSS 2	60
2 Aug. 1978	MSS 2	60
22 July 1980	MSS 2	60
4 Aug. 1981	MSS 2	60
3 July 1982	MSS 3	60
18 Aug. 1983	MSS 4	60
28 Aug. 1984	MSS 5	60
16 Sept. 1985	MSS 5	60
16 Sept. 1985	TM 5	30
17 July 1986	TM 5	30
21 Aug. 1987	TM 5	30
29 June 1991	TM 5	30
26 Aug. 1992	TM 4	30
9 Sept. 1994	TM 5	30
8 June 1995	TM 5	30
19 June 1999	TM 5	30
16 Aug. 2000	ETM+ 7	30
2 July 2001	ETM+ 7	30
21 July 2002	ETM+ 7	30
9 Aug. 2003	ETM+ 7	30
10 July 2004	ETM+ 7	30
14 Aug. 2005	ETM+ 7	30
10 Sept. 2006	TM 5	30
28 Aug. 2007	TM 5	30
5 July 2008	ETM+ 7	30
8 July 2009	ETM+ 7	30
20 Aug. 2010	TM 5	30
6 July 2011	TM 5	30
18 Oct. 2011	ETM+ 7	30
20 Oct. 2012	ETM+ 7	30

Table 2.2 Georeferencing and residual error for Landsat TM/ETM+ image pairs.

Image Pair	Georef. Error (pixels)	Georef Error (m)	Residual Error (pixels)	Residual Error (m)	RMSE (pixels, image year)
16 Sept. 1985, 17 July 1986	0.45 ± 0.25	16.5 ± 9.1	0.38 ± 0.24	13.9 ± 8.8	0.228, 1985
17 July 1986, 21 Aug. 1987	0.44 ± 0.13	12.2 ± 3.7	0.21 ± 0.15	5.7 ± 4.3	0.184, 1986
21 Aug. 1987, 29 June 1991	0.20 ± 0.14	6.2 ± 4.4	0.16 ± 0.09	5.0 ± 2.8	0.155, 1987
29 June 1991, 26 Aug. 1992	0.28 ± 0.18	7.8 ± 5.0	0.21 ± 0.13	5.9 ± 3.5	0.191,1991, 0.132, 1992
9 Sept. 1994, 8 June 1995	0.24 ± 0.16	8.8 ± 6.1	0.19 ± 0.13	7.1 ± 5.0	0.143, 1994
8 June 1995, 19 June 1999	0.21 ± 0.09	6.5 ± 2.8	0.13 ± 0.03	4.0 ± 1.1	0.154, 1995
19 June 1999, 16 Aug. 2000	0.22 ± 0.16	6.0 ± 4.5	0.15 ± 0.13	4.3 ± 3.7	0.155, 1999
16 Aug. 2000, 2 July 2001	0.20 ± 0.14	7.0 ± 4.9	0.17 ± 0.15	5.8 ± 5.1	0.119, 2000
2 July 2001, 21 July 2002	0.30 ± 0.09	9.0 ± 2.7	0.06 ± 0.04	1.9 ± 1.2	0.141, 2001
21 July 2002, 9 Aug. 2003	0.14 ± 0.10	4.0 ± 2.9	0.12 ± 0.11	3.6 ± 3.3	0.187, 2002
9 Aug. 2003, 10 July 2004	0.13 ± 0.06	3.9 ± 1.8	0.11 ± 0.04	3.3 ± 1.4	0.125, 2003
10 July 2004, 14 Aug. 2005	0.13 ± 0.07	4.0 ± 2.2	0.10 ± 0.07	3.1 ± 2.1	0.151, 2004
14 Aug. 2005, 10 Sept. 2006	0.26 ± 0.19	7.2 ± 5.3	0.24 ± 0.14	6.6 ± 3.9	0.121, 2005
10 Sept. 2006, 28 Aug. 2007	0.17 ± 0.16	5.3 ± 5.0	0.15 ± 0.12	4.6 ± 3.6	0.165, 2006
28 Aug. 2007, 5 July 2008	0.18 ± 0.08	6.5 ± 2.8	0.16 ± 0.09	5.7 ± 3.4	0.127, 2007
5 July 2008, 8 July 2009	0.16 ± 0.07	4.8 ± 2.1	0.06 ± 0.03	2.0 ± 0.9	0.148, 2008
8 July 2009, 20 Aug. 2010	0.18 ± 0.06	5.6 ± 1.9	0.09 ± 0.04	2.7 ± 1.4	0.139, 2009
20 Aug. 2010, 6 July 2011	0.18 ± 0.13	5.6 ± 4.1	0.11 ± 0.11	3.5 ± 3.4	0.092,2010, 0.225, 2011
18 Oct. 2011, 20 Oct. 2012	0.21 ± 0.14	6.3 ± 4.3	0.18 ± 0.14	5.5 ± 4.4	0.243,2011, 0.290, 2012
Average for TM/ETM+ imagery	0.22 ± 0.09	7.0 ± 3.0	0.15 ± 0.07	4.9 ± 2.6	0.16 ± 0.04

Table 2.3 Georeferencing and residual error for Landsat MSS image pairs.

Image pair	Georef. Error (pixels)	Georef. Error (m)	Residual Error (pixels)	Residual Error (m)	RMSE (pixels, image year)
24 Sept 1973, 27 July 1974	0.50 ± 0.21	36.8 ± 15.4	0.26 ± 0.14	19.4 ± 10.4	0.386, 1973
27 July 1974, 23 Sept. 1975	0.44 ± 0.15	23.1 ± 8.1	0.20 ± 0.12	10.9 ± 6.4	0.396, 1974
23 Sept. 1975, 7 July 1976	0.41 ± 0.61	14.7 ± 21.7	0.35 ± 0.59	12.5 ± 20.9	0.397, 1975
7 July 1976, 1 July 1977	0.38 ± 0.10	22.8 ± 6.2	0.14 ± 0.07	8.8 ± 4.7	0.428, 1976
1 July 1977, 2 Aug. 1978	0.33 ± 0.13	18.5 ± 7.3	0.16 ± 0.07	9.0 ± 4.2	0.391, 1977
2 Aug. 1978, 22 July 1980	0.50 ± 0.24	30.2 ± 14.6	0.26 ± 0.12	15.8 ± 7.2	0.357, 1978
22 July 1980, 4 Aug. 1981	0.50 ± 0.22	30.5 ± 13.2	0.26 ± 0.15	15.7 ± 9.4	0.682, 1980
2 Aug. 1981, 3 July 1982	0.87 ± 0.87	28.4 ± 28.5	0.36 ± 0.34	21.5 ± 21.2	0.747, 1981
3 July 1982, 18 Aug. 1983	0.42 ± 0.19	23.2 ± 10.4	0.32 ± 0.17	17.4 ± 9.6	0.430, 1982
18 Aug. 1983, 28 Aug. 1984	0.26 ± 0.12	15.8 ± 7.3	0.16 ± 0.09	10.1 ± 5.9	0.564, 1983
28 Aug. 1984, 16 Sept. 1985	0.35 ± 0.16	21.1 ± 10.0	0.24 ± 0.18	14.6 ± 11.1	0.496,1984, 0.470, 1985
Average for MSS imagery	0.45 ± 0.15	24.1 ± 6.7	0.25 ± 0.07	14.1 ± 4.2	0.47 ± 0.12

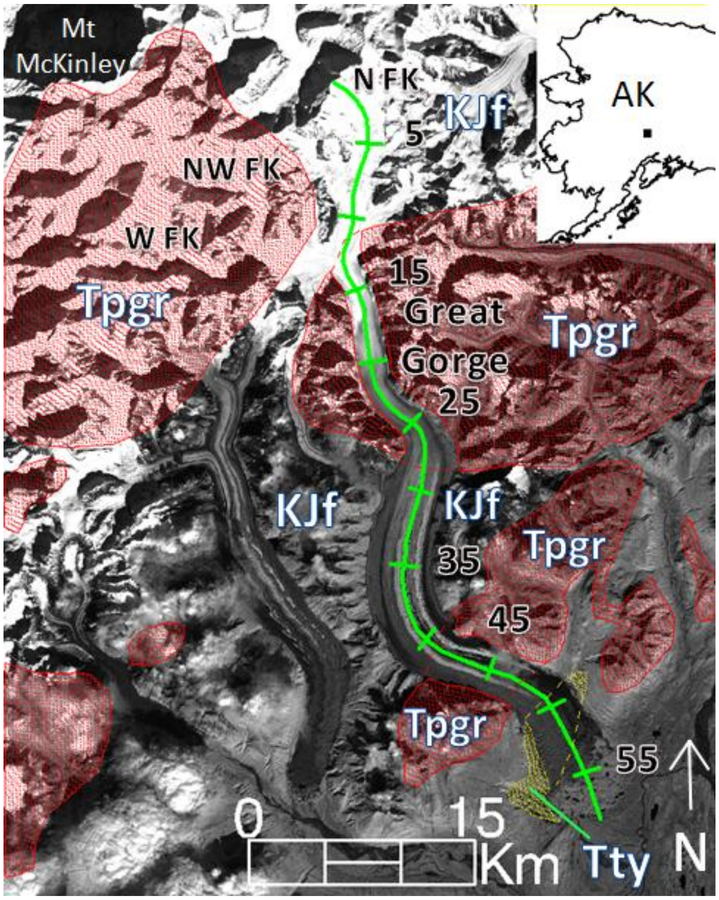

Figure 2.1. View of Ruth Glacier in the Alaska Range, Alaska. Red polygons indicate the extent of the granitic Tertiary age bedrock formations in the area, labeled Tpgr. KJf indicates Cretaceous/Jurassic age sedimentary bedrock, and Tty indicates Tertiary age sedimentary bedrock. The green line indicates a transect along the glacier centerline, beginning at the headwall of the North Fork, measured in km. The black rectangle within the inset indicates the position of the background image within Alaska.

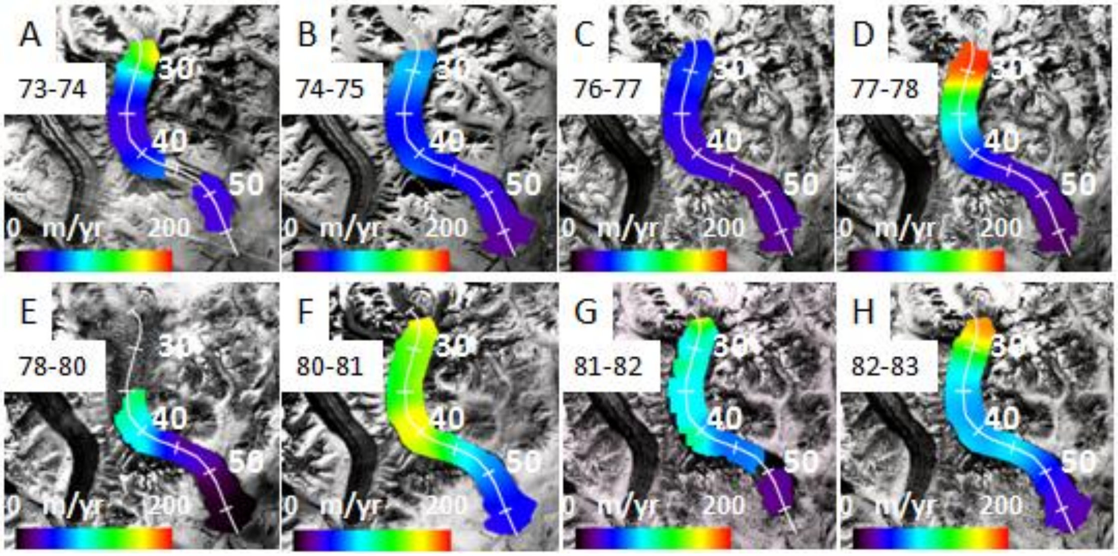

Figure 2.2. Velocity fields for Ruth Glacier, below the Great Gorge, from 1973 to 1983. Distances along the centerline transect are given in km from the headwall of the North Fork (See Figure 2.1). A) 1973–1974. B) 1974–1975. C) 1976–1977. D) 1977–1978. E) 1978–1980. F) 1980–1981. G) 1981–1982. H) 1982–1983.

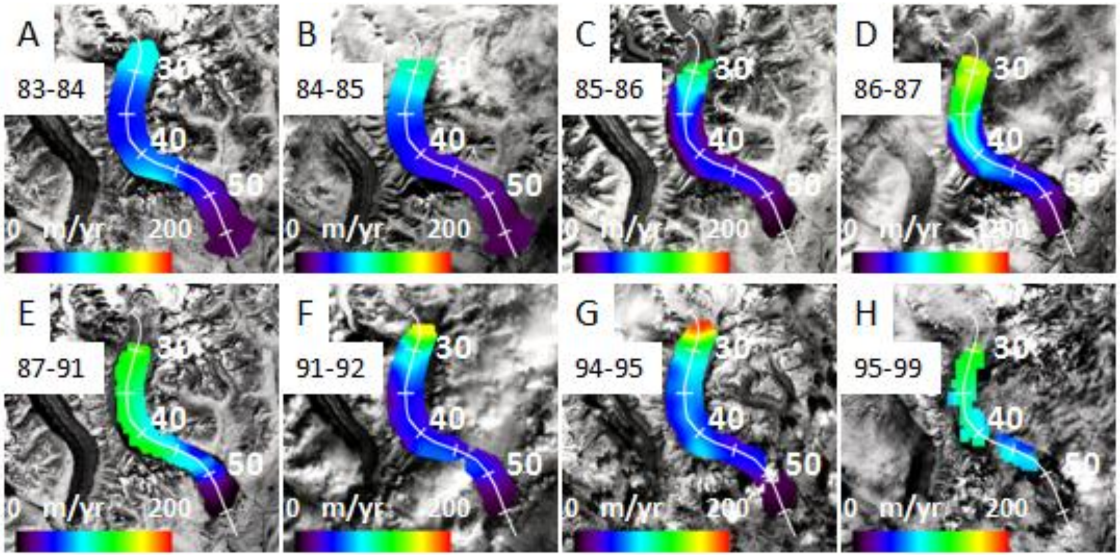

Figure 2.3. Velocity fields for Ruth Glacier, below the Great Gorge, from 1983 to 1999. Distances along the centerline transect are given in km from the headwall of the North Fork (See Figure 2.1). A) 1983–1984. B) 1984–1985. C) 1985–1986. D) 1986–1987. E) 1987–1991. F) 1991–1992. G) 1994–1995. H) 1995–1999.

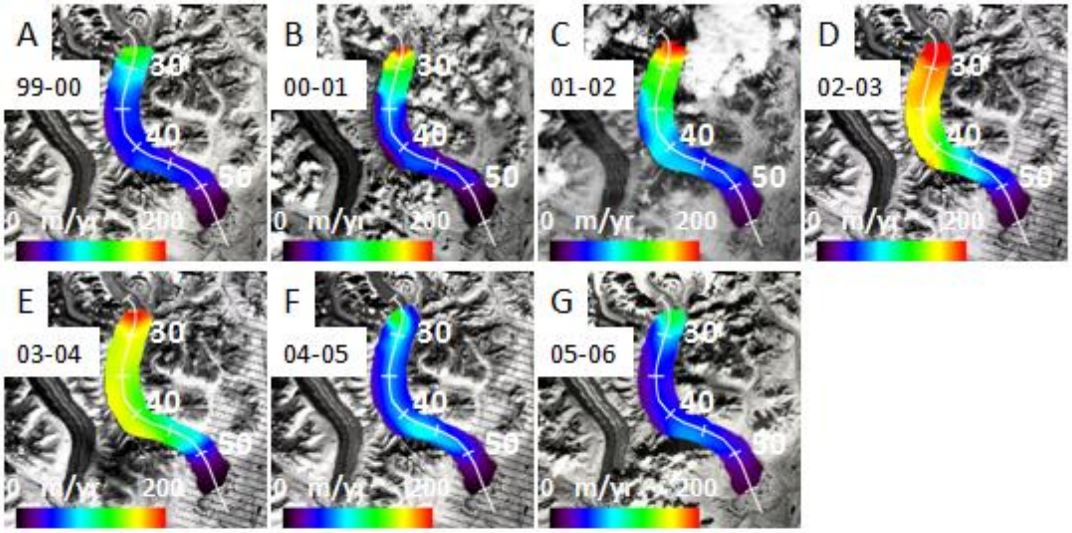

Figure 2.4. Velocity fields for Ruth Glacier, below the Great Gorge, from 1999 to 2006. Distances along the centerline transect are given in km from the headwall of the North Fork (See Figure 2.1). A) 1999–2000. B) 2000–2001. C) 2001–2002. D) 2002–2003. E) 2003–2004. F) 2004–2005. G) 2005–2006.

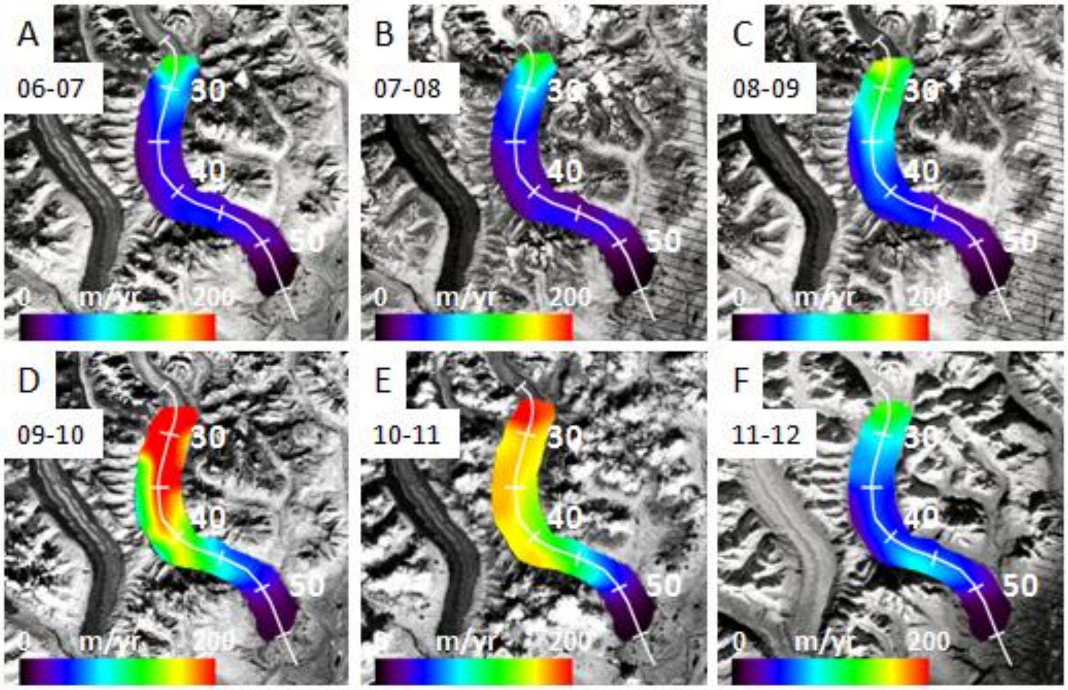

Figure 2.5. Velocity fields for Ruth Glacier, below the Great Gorge, from 2006 to 2012. Distances along the centerline transect are given in km from the headwall of the North Fork (See Figure 2.1). A) 2006–2007. B) 2007–2008. C) 2008–2009. D) 2009–2010. E) 2010–2011. F) 2011–2012.

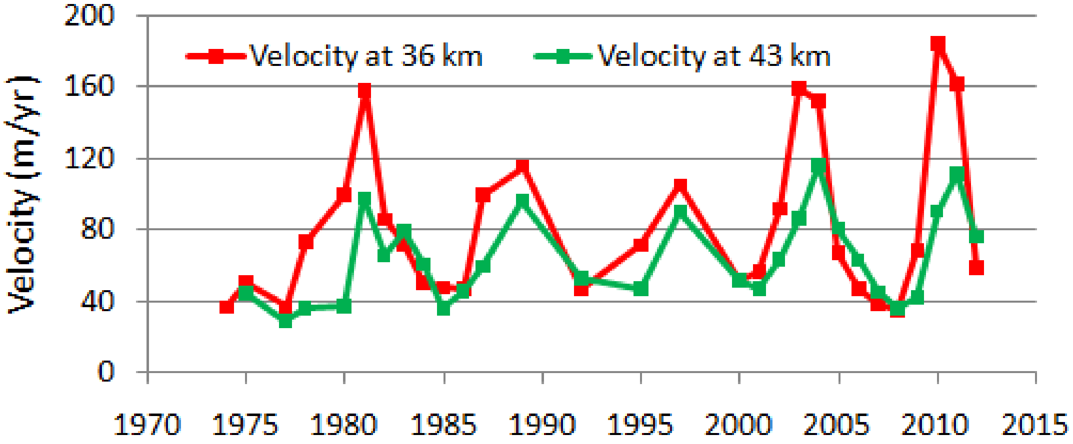

Figure 2.6. Temporal evolution of ice surface velocity on Ruth Glacier at the 36 km and 43 km marks from 1973 to 2012. Five pulses are evident, with peaks in velocity in 1981, 1989, 1997, 2003, and 2010, resulting in a characteristic pulse frequency of approximately 7 years.

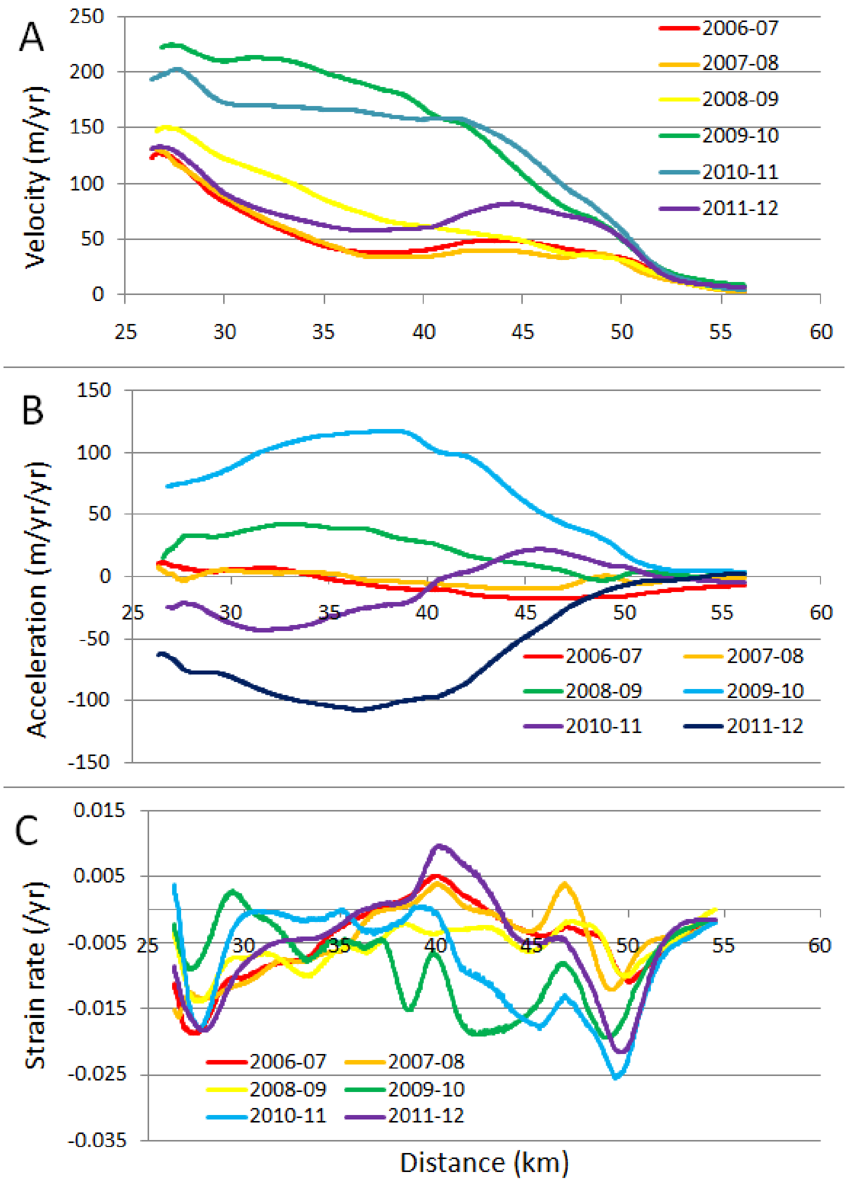

Figure 2.7. Longitudinal profiles of ice velocity, acceleration, and strain rate along the centerline transects shown in Figure 2.5, for the years 2006 to 2012, which surround the 2009–2010 pulse. A) Ice velocity. B) Ice acceleration. C) Longitudinal strain rate.

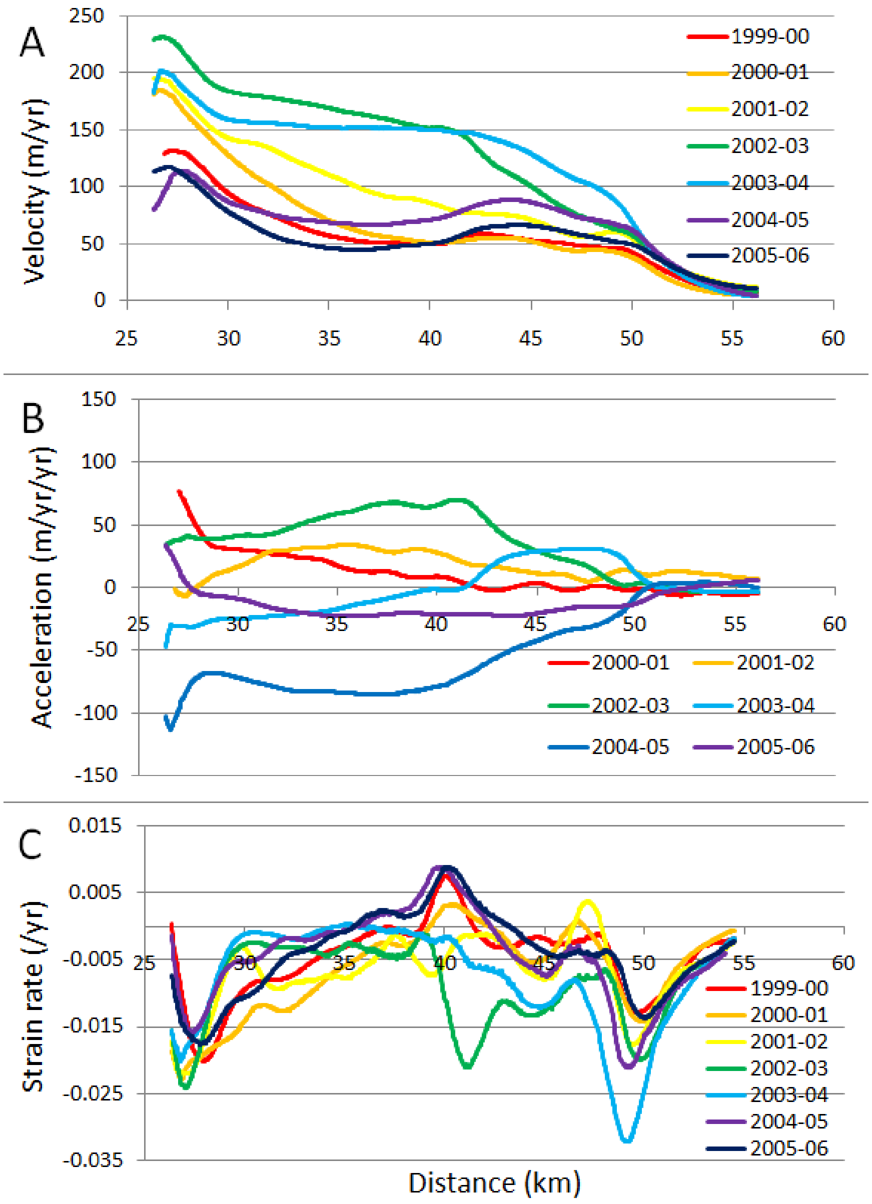

Figure 2.8. Longitudinal profiles of ice velocity, acceleration, and strain rate along the centerline transects shown in Figure 2.4, for the years 1999 to 2006, which surround the 2002–2003 pulse. A) Ice velocity. B) Ice acceleration. C) Longitudinal strain rate.

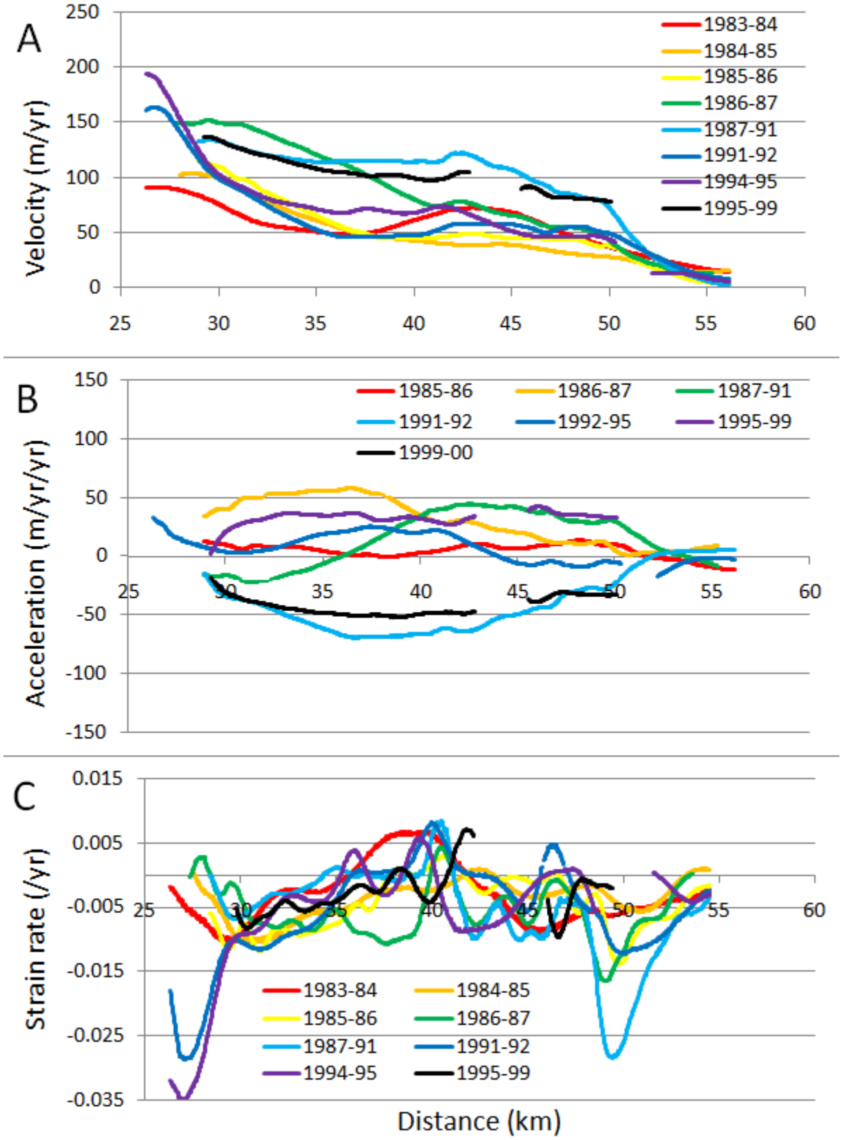

Figure 2.9. Longitudinal profiles of ice velocity, acceleration, and strain rate along the centerline transects shown in Figure 2.3, for the years 1983 to 1999, which surround the 1987–1991 and 1995–1999 pulses. A) Ice velocity. B) Ice acceleration. C) Longitudinal strain rate.

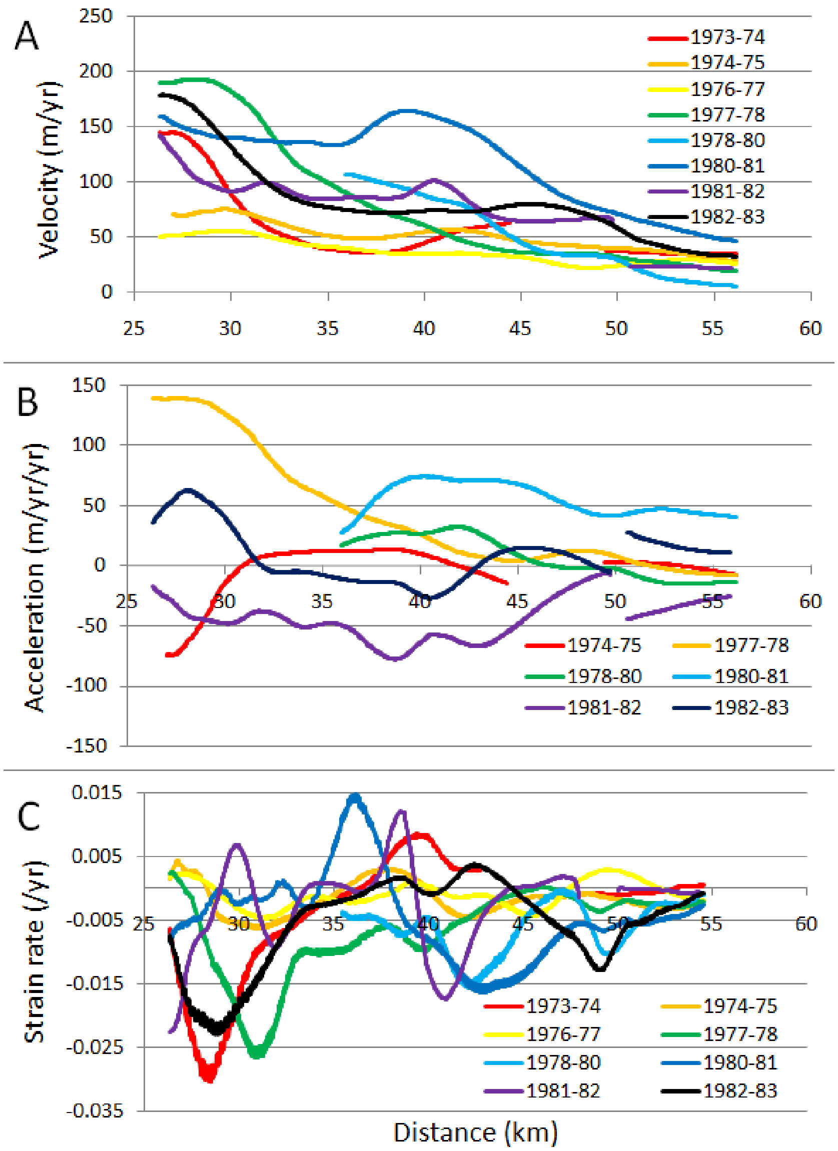

Figure 2.10. Longitudinal profiles of ice velocity, acceleration, and strain rate along the centerline transects shown in Figure 2.2, for the years 1973 to 1983, which surround the 1980–1981 pulse. A) Ice velocity. B) Ice acceleration. C) Longitudinal strain rate.

2.8 References

Ahn, Y., & Howat, I. (2011). Efficient automated glacier surface velocity measurement from repeat images using Multi-Image/Multichip and null exclusion feature tracking. *IEEE Transactions on Geoscience and Remote Sensing*, *49*(8), 2838–2846.

Blake, E. W., Clarke, G. K. C., & Gérin, M. C. (1992). Tools for examining subglacial bed deformation. *Journal of Glaciology, 38*(130), 388–396.

Boulton G. S., Dobbie K. E., & Zatsepin S. (2001). Sediment deformation beneath glaciers and its coupling to the subglacial system. *Quaternary International*, *86*(1), 3–28.

Burgess, E. W., Forster, R. R., & Larsen, C. F. (2013). Flow velocities of Alaskan glaciers. *Nature Communications, 4*, doi:10.1038/ncomms3146.

Csejtey, B. Jr, Mullen, M. W., Cox, D. P., & Stricker, G. D. (1992). Geology and geochronology of the Healy quadrangle, south-central Alaska: U.S. Geological Survey Miscellaneous Investigations Series Map 1961, 63 p., 2 sheets, scale 1:250,000.

Fitch, A. J., Kadyrov, A., Christmas, W. J., & Kittler, J. (2002). Orientation correlation. *British Machine Vision Conference*, 133–142.

Fowler, A. C., Murray, T., & Ng, F.S.L. (2001). Thermally controlled glacier surging. *Journal of Glaciology*, *47*(159), 527–538.

Frappé, T., & Clarke, G. K. C. (2007). Slow surge of Trapridge Glacier, Yukon Territory, Canada. *Journal of Geophysical Research*, *112*(F03S32), doi:10.1029/ 2006JF000607.

Gamble, B. M., & Reed, B. L. (1996). Preliminary geologic map of the eastern half of the Lime Hills quadrangle, Alaska: unpublished U.S. Geological Survey map compilation, scale 1:250,000.

Gesch, D., Evans, G., Mauck, J., Hutchinson, J., & Carswell Jr., W. J. (2009). *The National Map*—Elevation: U.S. Geological Survey Fact Sheet 2009–3053, 4 p.

Hall, D. K., & Ormsby, J. P. (1983). Use of SEASAT synthetic aperture radar and Landsat Multispectral Scanner Subsystem data for Alaskan glaciology studies. *Journal of Geophysical Research, 88*(C3), 1597–1607.

Harrison, W. D., Mayo, L. R., & Trabant, D. C. (1975). Temperature measurements of Black Rapids Glacier, Alaska, 1973. In Weller, G. and S. A. Bowling, eds. Climate of the Arctic. *Proceedings of the 24th Alaska Science Conference.* Fairbanks, AK, Univ. of Alaska, 350–352.

Harrison, W. D., & Post, A. S. (2003). How much do we really know about glacier surging? *Annals of Glaciology, 36*(1), 1–6.

Haug, T., Kääb, A., & Skvarca, P. (2010). Monitoring ice shelf velocities from repeat MODIS and Landsat data – A method study on the Larsen C ice shelf, Antarctic Peninsula, and 10 other ice shelves around Antarctica. *The Cryosphere, 4*(2), 161–178.

Heid, T., & Kääb, A. (2012a). Repeat optical satellite images reveal widespread and long term decrease in land-terminating glacier speeds. *The Cryosphere, 6*(2), 467–478.

Heid, T., & Kääb, A. (2012b). Evaluation of existing image matching methods for deriving glacier surface displacements globally from optical satellite imagery. *Remote Sensing of Environment, 118*, 339–355.

Jiskoot, H., Murray, T., & Boyle, P. (2000). Controls on the distribution of surge-type glaciers in Svalbard. *Journal of Glaciology*, *46*(154), 412–422.

Kamb, B., Raymond, C. F., Harrison, W. D., Engelhardt, H., Echelmeyer, K. A., Humphrey, N., Brugman, M. M., & Pfeffer, T. (1985). Glacier surge mechanism: 1982–1983 surge of Variegated Glacier, Alaska. *Science*, *227*(4686), 469–479.

Kavanaugh, J. L. (2009). Exploring glacier dynamics with subglacier water pressure pulses: Evidence for self-organized criticality? *Journal of Geophysical Research*, *114*(F01021), doi:10.1029/2008JF001036.

Lee, D. S., Storey, J. C., Choate, J., & Hayes, R. W. (2004). Four years of Landsat-7 on-orbit geometric calibration and performance. *IEEE Trans. on Geoscience and Remote Sensing*, *42*(12), 2786–2795.

Leprince, S., Barbot, S., Ayoub, F. & Avouac, J. P. (2007). Automatic and precise ortho-rectification, coregistration, and subpixel correlation of satellite images, application to ground deformation measurements. *IEEE Transactions on Geoscience and Remote Sensing*, *45*(6), 1529–1558.

Mayo, L. R. (1978). Identification of unstable glaciers intermediate between normal and surging glaciers. Academy of Sciences of the USSR. *Section of Glaciology of the Soviet Geophysical Committee and Institute of Geography, Data of Glaciological Studies Chronicle*, Discussion, Publication 133, 133–135, Moscow, May 1978.

Murray, T. (1997). Assessing the paradigm shift: Deformable glacier beds. *Quaternary Science Reviews*, *16*(9), 995–1016.

Murray, T., Stuart, G. W., Miller, P. J., Woodward, J., Smith, A. M., Porter, P. R., Jiskoot, H. (2000). Glacier surge propagation by thermal evolution at the bed. *Journal of Geophysical Research*, *105*(B6), 13,491–13,507.

Murray, T, & Porter P. R. (2001). Basal conditions beneath a soft-bedded polythermal surge-type glacier: Bakaninbreen, Svalbard. *Quaternary International*, *86*(1), 103–116.

Murray, T., Strozzi, T., Luckman, A., Jiskoot, H., & Christakos, P. (2003). Is there a single surge mechanism? Contrasts in dynamics between glacier surges in Svalbard and other regions. *Journal of Geophysical Research*, *108*(B5), 2237, doi:10.1029/2002JB001906.

Nolan, M. (2003). The "Galloping Glacier" trots: Decadal-scale speed oscillations within the quiescent phase. *Annals of Glaciology*, *36*(1), 7–13.

Nolan M., & Echelmeyer, K. (1999). Seismic detection of transient changes beneath Black Rapids Glacier, Alaska, USA: I. Techniques and observations. *Journal of Glaciology*, *45*(149), 119–131.

Post, A. (1969). Distribution of surging glaciers in western North America. *Journal of Glaciology*, *8*(53), 229–240.

Reed, B. L., & Nelson, S. W. (1980). Geologic map of the Talkeetna quadrangle, Alaska: U.S. Geological Survey, Miscellaneous Investigation Series Map I-1174, 15 pages, 1 plate, scale 1:250,000.

Reynolds, O. (1885). On the dilatancy of media composed of rigid particles in contact. With experimental observations. *Philosophical Magazine and Journal of Science 20*(127), 469–481.

Roush, J. J., Lingle, C. S., Guritz, R. M., Fatland, D. R., & Voronina, V. A. (2003). Surge-front propagation and velocities during the early 1993–95 surge of Bering Glacier, Alaska, USA, from sequential SAR imagery. *Annals of Glaciology*, *36*(1), 37–44.

Scherler, D., Leprince, S., & Strecker, M. (2008). Glacier-surface velocities in alpine terrain from optical satellite imagery – Accuracy improvement and quality assessment. *Remote Sensing of Environment*, *112*, 3806–3819.

Shekarforoush, M., Berthod, M., & Zerubia, J. (1996). Subpixel image registration by estimating the polyphase decomposition of cross power spectrum. *Proceedings: IEEE. Computer Society Conference on Computer Vision and Pattern Recognition.* San Francisco, CA., USA. June 18–20, 1996.

Shulski, M., & Mogil, H. M. (2009). Alaska's climate and weather. *Weatherwise*, *62*(1), 14-21.

Solie, D. N., Gilbert, W. G., Harris, E. E., Kline, J. T., Liss, S. A., & Robinson, M. S. (1991). Preliminary geologic map of Tyonek D-6 and eastern Tyonek D-7 quadrangles, Alaska: Alaska Division of Geological and Geophysical Surveys Public-data File 91-10, scale 1:63,360, 15 p., not paginated.

Stone, D. B. (1993). Characterization of the basal hydraulic system of a surge-type glacier: Trapridge Glacier, 1989–1992. Ph.D. Thesis, University of British Columbia, Vancouver, Canada.

Storey, J. C., & Choate, M. J. (2004). Landsat-5 bumper-mode geometric correction. *IEEE Transactions on Geoscience and Remote Sensing*, *42*(12), 2695–2703.

Truffer, M., Harrison, W. D, & Echelmeyer, K. A. (2000). Glacier motion dominated by processes deep in underlying till. *Journal of Glaciology*, *46*(153), 213–221.

Truffer, M, Echelmeyer, K. A., & Harrison, W. D. (2001). Implications of till deformation on glacier dynamics. *Journal of Glaciology*, *47*(156), 123–134.

Turrin, J., Forster, R. R., Larsen, C., & Sauber, J. (2013). The propagation of a surge front on Bering Glacier, Alaska, 2001–2011. *Annals of Glaciology*, *54*(63), 221–227.

Ward, J. D., Anderson, R. S., & Haeussler, P. J. (2012). Scaling the Teflon Peaks: Rock type and the generation of extreme relief in the glaciated western Alaska Range. *Journal of Geophysical Research*, *117*(F01031), doi:10.1029/2011JF002068.

Willis, I.C. (1995). Intra-annual variations in glacier motion: A review. *Progress in Physical Geography*, *19*(1), 61–106.

CHAPTER 3

A MECHANISM FOR CYCLICAL GLACIER FLOW IN OVERDEEPENINGS

3.1 Abstract

A nearly 4-decade, satellite-based velocity survey of the largest glaciers in the Alaska Range, Chugach Mountains, and the Wrangell Mountains of southern Alaska, spanning the early- to mid-1970s through the 2000s, reveals eight pulsing glaciers: Kahiltna, Eldridge, Capps, Matanuska, Copper, Nabesna, Nizina, and Sanford glaciers. The pulses increase velocity by up to 2449% (Capps Glacier) or as little as 77% (Nabesna Glacier), with velocity increases for the other six glaciers in the range of 100–250%. The pulses may last from between 6 years (Copper Glacier) to 12 years (Nizina Glacier) and consist of a multiyear acceleration phase followed by a multiyear deceleration phase during which significant portions of each glacier move en masse. The segments of each glacier affected by the pulses may be anywhere from 14 km (Sanford Glacier) to 36 km (Nabesna Glacier) in length and occur where the glaciers are either laterally constricted or joined by a major tributary. In addition, the surface slopes at these locations are very shallow, 1–2°, suggesting the pulses occur where the glaciers are overdeepened. A mechanism to explain the cyclical behavior of these pulsing glaciers is presented and incorporates the effects of glaciohydraulic supercooling, glacier dynamics, ablation, and

sediment erosion, deposition, and deformation in overdeepenings.

3.2 Introduction

3.2.1 Glacier Pulses

In this study a glacier pulse is defined as a type of dynamic behavior characterized by a multiyear acceleration phase in which the glacier progressively increases its velocity due to deformation of a subglacial till, immediately followed by a multiyear deceleration phase during which the glacier progressively slows as the till consolidates. This nomenclature is borrowed from the three phases of Svalbard-type surges, which have acceleration, deceleration, and quiescent phases (Murray et al., 2003), and which also accelerate due to till deformation. Pulses are cyclical in nature, as has been found on Black Rapids Glacier (Nolan, 2003), Trapridge Glacier (Frappé & Clarke, 2007), and Ruth Glacier (Turrin et al., in review), with the cycles lasting from 4 to 12 years. As discussed by Turrin et al. (in review), and based on theory by Fowler et al. (2001), the till at the base of a pulsing glacier is perennially temperate, not frozen, which allows almost instantaneous transfer of shear stresses. So, when a till dilates and can no longer support shear stress, the stress is immediately transferred to nearby locations that may also be near their threshold of failure and which will also dilate, deform, and again transfer the stress elsewhere. This process results in a cascade of till failure and stress transfer beneath a glacier that Nolan (2003) describes as activation waves. These activation waves move so rapidly beneath a glacier that the activated portion of the glacier slumps forward all at once, rather than forming a kinematic wave at the leading edge of the activation wave as it travels downglacier. Pulses end by depressurization of the subglacial drainage system and consolidation of the till. Again, this appears to happen without formation of a kinematic wave, so deactivation of the till must occur rapidly as well. Therefore, pulses are characterized by a spatiotemporal velocity signature in which a portion of a glacier accelerates and then decelerates en masse; no wave front is evident at the glacier surface as might be seen during a surge (e.g., Bering Glacier; Turrin et al., 2013). Instead, the surface of pulsing glaciers is characterized by wavy medial moraines, large-scale wavy foliation, boudinage (sausage-shaped structures in the ice formed by extension), and potholes (Mayo, 1978), each a result of pulses repeatedly compressing and extending the ice.

So, while pulses produce increased basal motion via a change in the state of a subglacial till from consolidated to dilated (and subsequent deformation), surges increase basal motion via slip at the ice/bed interface, and involve a transformation of the subglacial drainage system from low-pressure, fast flow in channels to high-pressure slow flow through distributed cavities (Kamb et al., 1985). The rate at which the subglacial changes occur determines whether a kinematic wave forms, or not. The slower process of reshaping the drainage system beneath a glacier results in the formation of a kinematic wave during a surge (e.g., Turrin et al., 2013), while the faster process of till dilation precludes the formation of a kinematic wave. Both processes are cyclical. The length of a surge cycle is dependent upon climate and the rate at which ice accumulates in the glacier’s upper reaches and the rate at which ice ablates in its lower reaches and may last decades or centuries (Post, 1969).

What causes pulses to be cyclical? Nolan (2003) suggests at the end of a pulse the subglacial till may be incompletely drained and hence only partially consolidated, leaving it primed for another pulse when subglacial water pressure rises again. However, this idea does not provide a mechanism to fully explain how or why periodicity exists on pulsing glaciers; it merely suggests a scenario in which a till might easily deform again. A complete answer to the question posed above is lacking. Therefore, the aim of this study is to provide a glaciologically sound, physical mechanism to explain the oscillatory nature of glacier pulses, based on observations and previous theory.

3.3 Study Region

To construct a theory that explains the cyclical behavior of pulsing glaciers, glaciers that have recently pulsed must be identified, their dynamic behavior studied, and their common characteristics analyzed. To help accomplish these tasks, velocity fields of the 90 largest glaciers in the Alaska Range, Chugach Mountains, and Wrangell Mountains were produced from the 1970s through the 2000s to identify glacier pulses and their common traits. Pulsing glaciers were identified by their spatiotemporal velocity signature consisting of a multiyear acceleration phase, followed by a multiyear deceleration phase in which a significant portion of the ablation zone moved en masse. In addition to those pulsing glaciers mentioned above, eight new glaciers were found to have experienced pulses within the past 4 decades, they are: Eldridge, Kahiltna, Capps, Matanuska, Copper, Nabesna, Nizina, and Sanford glaciers (Figure 3.1). Brief descriptions of the relevant features of each glacier are presented in the following sections, grouped by location. The bedrock lithology underlying each glacier is also noted within each glacier description, but the reader is referred to the Methods section for a more complete description of this data set. Of these eight glaciers, Mayo (1978) specifically lists four of them, Kahiltna, Capps, Nizina, and Sanford glaciers, as pulse-type glaciers. The other four glaciers are not mentioned, but Mayo (1978) counted approximately 140 pulse-type glaciers in southern Alaska and did not provide all their names. Post (1969) lists the North Fork of Eldridge Glacier as surge-type, but not the main branch, and he lists Capps Glacier as possibly being of surge-type.

3.3.1 Central Alaska Range

Eldridge Glacier (Figure 3.2) is approximately 50 km in length and 3–4 km in width throughout the ablation zone. Its accumulation zone is comprised of 4 major lobes and numerous smaller branches that converge near the 13 km mark to form the main glacier trunk. At the 34–35 km mark the North Fork of Eldridge Glacier converges with the main trunk from the north-northeast. The North Fork is approximately 30 km long and 1.5 km wide and has a convolute medial moraine, indicating past surging or pulsing behavior. Previous pulsing behavior is indicated on the main trunk by wavy patterns in medial moraines near the 30 and 38 km marks. From approximately the 35 km mark to the terminus, the surface of Eldridge Glacier is almost entirely covered by debris, indicative of surface downwasting. Eldridge Glacier is underlain by granite, crystalline tuff, and sedimentary bedrock, labeled as Tpgr, JTRct, and KJf in Figure 3.2, respectively (Wilson et al., 1998).

Kahiltna Glacier (Figure 3.3) is approximately 76 km in length and 3–5 km in width throughout the ablation zone. Its accumulation zone is comprised of at least 10 small cirques that combine between the 0–20 km marks to form the main trunk, with numerous other small tributaries joining in the upper ablation zone. The uppermost reaches of the accumulation zone have the southern flank and peak of Mt. McKinley as their headwall, at 6168 m above sea level. The whole length of the ablation zone, nearly down to the terminus, contains linear medial moraines, with some mild wavy patterns apparent beginning near the 65 km mark, indicating past pulsing behavior. Kahiltna

Glacier is underlain by granite, granodiorite, and two different formations of sedimentary bedrock, labeled as Tpgr, Toem, JCmd, and KJf in Figure 3.3, respectively (Wilson et al., 1998).

3.3.2 West Alaska Range

Capps Glacier (Figure 3.4) is approximately 42 km in length, 2.5 km wide in the upper ablation zone, and has an oblong piedmont lobe that is roughly 13 km long and 5 km wide. The accumulation zone is comprised of 6 lobes that merge between the 12 and 17 km marks to form the main trunk. The upper ablation zone contains linear medial moraines that become increasingly wavy in the piedmont lobe, indicating past pulsing behavior. Capps Glacier is underlain by granite, basalt, and three different sedimentary bedrock formations, labeled in Figure. 3.4 as Tpgr, QTv, Twf, Tty, and KJf, respectively (Wilson et al., 1998).

3.3.3 Chugach Mountains

Matanuska Glacier (Figure 3.5) is approximately 48.5 km in length and 3.0 km wide in the midablation zone. Its accumulation zone consists of two branches that merge at the 17 km mark to form the main trunk. A single major tributary joins the main trunk near the 32 km mark that is 19 km long and 1.5 km wide. The entire length of the ablation zone of Matanuska Glacier is embedded with linear medial moraines, and the very toe of the glacier is covered in sediment, indicating downwasting there. Matanuska Glacier is underlain by granite, various igneous ultramafic rocks, and three different sedimentary formations, labeled Ji, Jmu, JTRtk, Tch, and Kvs in Figure 3.5, respectively (Wilson et al., 1998).

3.3.4 Wrangell Mountains

Copper Glacier (Figure 3.6) is approximately 29.5 km in length and 1.0–1.5 km in width in the ablation zone, and it has a broad, flat accumulation zone without distinct lobes or cirques. Copper Glacier lacks any major tributaries, its ablation zone contains a few thin linear medial moraines, and it terminates in a small piedmont lobe approximately 4 km wide. It is underlain by three different formations of lava and some unlithified sediments, labeled in Figure 3.6 as QTw, Qwj, Qwws, and Qg, respectively (Richter et al., 2006).

Nabesna Glacier (Figure 3.7) is the largest glacier in the Wrangell Mountains at nearly 66 km in length, and it is 3.5 to 4.5 km wide in the ablation zone. Its accumulation zone consists of two large branches, each with multiple lobes, that span roughly 43 km from Mt. Regal in the east to Mt. Wrangell in the west (Capps, 1910) and which merge to form the main trunk near the 30 km mark. The ablation zone has no tributaries that merge with it, instead there are two locations along the eastern margin (at the 42 and 48 km marks), and two along the western margin (at the 35 and 42 km marks), where ice stagnates and ablates rather than being transported to the terminus. The main trunk of the ablation zone is embedded with numerous prominent linear medial moraines, some of which exhibit a broad curve near the terminus as the ice there flows around a nunatak just left of the glacier centerline near the 61 km mark. Nabesna Glacier is underlain by three different formations of lava and some granite, labeled in Figure 3.7 as QTw, Trn, PPt, and Tp, respectively (Richter et al., 2006).

Nizina Glacier (Figure 3.8) is approximately 33 km in length and 2.5 km wide in the ablation zone. Its accumulation zone consists of two large lobes that merge between the 5 and 10 km marks to form the main glacier trunk, and a small lobe that contributes ice to the main trunk along the southern margin near the 12 km mark. Nizina Glacier is joined by Rohn Glacier near the 22 km mark. Rohn Glacier is roughly equal in size to Nizina Glacier but moves slower, so it experiences greater surface lowering due to ablation, greater sediment retention on its surface and therefore has a lower albedo overall. Nizina Glacier is more active than Rohn Glacier and consequently transports its ice further down valley, forming most of the terminus of the combined glacier system, while the ice of Rohn Glacier completely ablates by the 28 km mark. Nizina Glacier is embedded with numerous prominent linear medial moraines that become slightly wavy around the 28 km mark indicating past pulsing behavior. Nizina and Rohn glaciers are underlain by two different formations of lava and four different formations of sedimentary bedrock, labeled as QTw, Trn, Kl, Ku, Pl, and Ph in Figure 3.8, respectively (Richter et al., 2006).

Sanford Glacier (Figure 3.9) is approximately 30 km long and 1.5 km wide in the ablation zone, and its accumulation zone consists of a broad nondescript snowfield that extends south to the flanks of Mt. Zanetti (3965 m) and Mt.Wrangell (4317 m) and east to the peak of Mt. Sanford (4949 m) at the 0 km mark. A major tributary merges with Sanford Glacier from the northeast near the 20 km mark which is nearly as wide as Sanford Glacier but appears stagnant, because it is entirely covered by debris and has numerous potholes. The upper ablation zone of Sanford Glacier, before the junction with its major tributary, has some prominent linear medial moraines, some of which exhibit boudinage, indicative of past extension, likely due to past pulsing behavior. The lower ablation zone is debris-covered and has numerous water-filled potholes, suggesting downwasting and stagnation. Sanford Glacier is underlain by lava flows of four different formations, labeled Qws, Qwws, Qtw, and Qwj in Figure 3.9 (Richter et al., 2006).

3.4 Methods

3.4.1 Optical Feature Tracking

COSI-Corr feature tracking software (Leprince et al., 2007) was used to produce velocity fields in conjunction with Landsat MSS, TM, ETM+, and Operational Land Imager (OLI) satellite imagery. See Table 3.1 (Central Alaska Range), Table 3.2 (West Alaska Range), Table 3.3 (Chugach Mountains), and Table 3.4 (Wrangell Mountains) for the date and sensor of the 148 images used to produce the velocity fields. When two Landsat-7 ETM+ images with scan-line voids were matched, which occurs for ETM+ images acquired after the May 2003 failure of the scan-line correction system, then orientation images were produced (Fitch et al., 2002) prior to insertion into COSI-Corr. The individual displacement measurements produced by COSI-Corr were processed to create velocity fields in the manner described by Turrin et al. (in review). The exception to this processing chain involves the use of OLI images which have a 12-bit quantization (4096 distinct brightness values may be recorded by the sensor for each optical band); whereas previous Landsat TM and ETM+ images have 8-bit quantization (256 distinct brightness values may be recorded). To rectify this difference, OLI images were requantized to 8 bits prior to insertion into COSI-Corr. The final product is a time-series of velocity rasters for the largest glaciers of each mountain range that allows identification of those glaciers which have recently pulsed and their common characteristics.

The accuracy of the velocity fields depends upon the precision of the feature tracking algorithm used to produce the displacement measurements and how well the two images being matched are aligned. COSI-Corr has been shown to have a measurement error of ±0.08 pixel (±1.2 m) for 15-m ETM+ panchromatic imagery (Heid and Kääb, 2012). If we extrapolate this same level of precision to 30-m imagery the expected error is ±2.4 m, and for 60-m imagery it is ±4.8 m. Turrin et al. (in review) showed the average misalignment between two MSS images with 60-m spatial resolution is 0.25 ± 0.07 pixel, or 14.1 ± 4.2 m, and for 30-m TM and ETM+ image pairs the average misalignment is 0.15 ± 0.07 pixel, or 4.9 ± 2.6 m, after removal of the systematic error. Only 1 OLI image was used in this study (see Table 3.4) and its geolocation error is 0.15 pixels (4.6 m), as listed in the metadata accompanying the image by the U.S. Geological Survey. This value is comparable to the average value of 0.16 ± 0.04 pixel of geolocation error for TM and ETM+ images found by Turrin et al. (in review), so we expect the velocity field produced using the OLI image to have an error similar in magnitude to those produced using TM and ETM+ images. The total error in the velocity fields is estimated from the precision of COSI-Corr and the final image misalignment using the root sum of squares method, because these variables are independent of one another. For 30-m TM, ETM+, and OLI imagery the error is estimated to be 5.1 m (0.17 pixel), and for 60-m MSS imagery the error is estimated to be 15.7 m (0.26 pixel).

The bedrock formations that underlie each of the eight glaciers were taken from either a U.S. Geological Survey Open-File Report (Wilson et al., 1998) or a U.S. Geological Survey Scientific Investigations Map (Richter et al., 2006). These maps are compilations and reinterpretations of many published and unpublished works and provide the geologic structure and bedrock lithology of each mountain range at a level appropriate for this study. Subsets of these geologic maps were georeferenced to a Landsat image by manually picking tie-points between the map and the satellite image. During the georeferencing routine the geologic maps were also resampled to 30-m spatial resolution to match the Landsat image. The subsequent location error of the georeferenced geologic maps is estimated to be up to 5 pixels (150 m) in some locations, but less in most locations. Using the georeferenced geologic maps as a backdrop, the bedrock formations underlying each glacier were outlined and overlaid upon the Landsat images (see Figures 3.2 to 3.9). Each bedrock formation is labeled using the same stratigraphic symbol as in the source map.

3.5 Results

3.5.1 Eldridge Glacier

Eldridge Glacier pulsed twice between 1982 and 2012 (Figure 3.10). The first pulse, spanning the period from 1982 to 1992, peaked in 1987 with a maximum velocity of 97.8 m/yr at the 35 km mark. This is a 146% increase in velocity compared to the velocity prior to the pulse in 1982 of 39.6 m/yr. The second pulse spanned the period from 2001 to 2008 and was lesser in magnitude, with a peak in 2004 of 68.8 m/yr at the 35 km mark that represents a 95% increase in velocity from a low of 35.2 m/yr in 2001. Both pulses caused a 25 km stretch of the glacier, between the 20 and 45 km marks, to accelerate then decelerate en masse (Figure 3.11a, b), and the surface slope of this part of the glacier is consistently < 2° (Figure 3.11c), which makes this the flattest part of the glacier. It is worth noting there are small inflections in velocity near the 34 km mark in the 1986-1987, 1987-1991, 2001-2002, 2002-2003, and 2004-2005 velocity profiles, where the bedrock changes from sedimentary (KJf) to crystalline tuff (JTRct); this is also the location where the North Fork merges with the main trunk. Velocity maps spanning 1982 to 1992 are provided in Figure 3.12 to illustrate the waxing and waning of the first pulse. The pulses do not affect the North Fork, but instead are confined to the main trunk.

3.5.2 Kahiltna Glacier

Kahiltna Glacier pulsed twice between 1995 and 2012 (Figure 3.13). The first pulse appears to span the time period from 1995 to 2004, but could not be temporally well-defined due to lack of imagery during the 1990s. The first pulse peaked in 2001, with a velocity of 131.4 m/yr at the 65 km mark, which is a 204% increase compared to the velocity prior to the pulse in 1995 of 43.2 m/yr. The second pulse is briefer in time, spanning 2008 to 2012, with a peak velocity of 157.5 m/yr in 2010. This represents a 177% increase compared to the velocity prior to the pulse in 2008 of 56.8 m/yr. The pulses affect the glacier approximately from the 60 km mark down to the terminus, a 16 km span; with the ice in this area accelerating then decelerating en masse (Figure 3.14a, b). Ice upglacier of this area seems relatively unaffected by the pulses. Goodwin et al. (2012) produced velocity fields of Kahiltna Glacier for the winters of 2007 and 2008 using speckle tracking on Synthetic Aperture Radar (SAR) images. The overall shape and magnitude of their velocity profiles agree quite well with the ones presented here, all of which show velocities below 25 m/yr at the terminus, increasing steadily to approximately 250 m/yr near the 50 km mark, then decreasing to roughly 200 m/yr near the 40 km mark, and then increasing to a peak of 400 m/yr near the 20 km mark. The agreement between the work of Goodwin et al. (2012) and the work presented here provides some confidence in the velocity measurements used in this study.

At approximately the 60 km mark the bedrock geology changes from granitic (Tpgr) to sedimentary (KJf) (Figure 3.3), so the area most affected by the pulses is underlain by the sedimentary rock. Kahiltna Glacier is a long, gently sloping glacier with a surface slope that is routinely below 2° along much of its ablation zone (Figure 3.14c), with an exception at the 56–57 km marks after the ice exits a constriction. The area of

Kahiltna Glacier that pulsed is even more gently inclined, with a surface slope of approximately 1.5°. Figure 3.15 displays velocity fields from 1994-1995 to 2004-2005, spanning the first pulse. Even with prior knowledge of the existence of the pulse and its location on the glacier, it is difficult to discern in this time-series. This illustrates the ease in which pulses may be overlooked without comparison of centerline profiles.

3.5.3 Capps Glacier

Evidence of three pulses was found in the time-series of velocity fields for Capps Glacier (Figure 3.16). The first pulse achieved the highest peak velocity of 623.2 m/yr in 1974 at the 35 km mark, but only the deceleration phase of the pulse was detected due to lack of imagery before this time. The second pulse spanned from 1981 to 1987 and peaked in 1985 at 537.9 m/yr at the 35 km mark. The peak velocity of the second pulse is a 2449% increase in velocity compared to the velocity prior to the pulse in 1981 of 21.1 m/yr. Both the 1974 and 1985 pulses ended abruptly, decelerating more than -500 m/yr from their peak velocities to quiescent phase velocities within 1 year. The third pulse is not temporally well-defined due to lack of available cloud-free imagery, but the peak and deceleration phase are evident. The peak of the third pulse occurred in 2001 with a velocity of 237.2 m/yr. The third pulse is noticeably different from the previous two pulses because its amplitude is significantly less and the deceleration phase lasted for 5 years, from 2001 until 2006 when the glacier slowed to 17.5 m/yr. Since 2008 Capps Glacier has been steadily accelerating and appears to be in the acceleration phase of a new pulse. The velocity fields (Figure 3.17) and velocity profiles (Figure 3.18a, b) of Capps Glacier show that the glacier, from the 18 km mark down to the terminus at the 42 km mark, a 24 km length, is affected by the pulses, with the ice in this region accelerating and then decelerating en masse. At the 28 km mark inflections are seen in the velocity profiles in the 1980-1981, 1981-1982, 1985-1986, 1999-2000, 2000-2001, 2001-2002, and 2002-2003 velocity profiles, and a velocity low is seen in the 1984-1985 velocity profile. The 28 km mark is approximately where the bedrock transitions from volcanic and granitic (QTv, Tpgr) to primarily sedimentary (KJf, Tty, Twf; Figure 3.4), but perhaps more importantly, the glacier widens from 2.5 km to 4.7 km after it exits its constraining valley. The surface slope of Capps Glacier is consistently about 1.5° from roughly the 15 km mark to near the terminus (Figure 3.18c), with the exception of a roughly 5 km stretch from the 23 to the 28 km marks where the valley is narrowest and which has a surface slope of approximately 2°.

3.5.4 Matanuska Glacier

Matanuska Glacier pulsed twice between 2000 and 2013 (Figure 3.19). The first pulse spanned from at least 2000 to 2006, but the entire acceleration phase was not captured due to lack of imagery. The first pulse achieved a greater maximum velocity than the second, with a peak in 2001 of 257.5 m/yr at the 41 km mark, followed by deceleration over a 5 year period to a low of 32.3 m/yr in 2006. The second pulse caused a 373% increase in velocity, from 32.3 m/yr in 2006 to the peak in 2010 at 154.5 m/yr, and since then has been steadily decelerating. The velocity fields (Figure 3.20) and velocity profiles (Figure 3.21a, b) show that for the first pulse, the glacier accelerated all at once, from approximately the 27 km mark down to the terminus at the 48 km mark, a 21 km length, while the second, weaker pulse affected a smaller stretch of the glacier, from approximately the 34 km mark to the terminus, a 14 km length. Almost all the velocity profiles have an inflection near the 28–29 km marks, coinciding with a small constriction of the glacier (see Figure 3.5). Several velocity profiles associated with the second pulse have inflections at the 34 km mark (2008-2009, 2009-2010, 2010-2011, 2011-2012) which coincides with a change in bedrock geology from metasedimentary rocks (Kvs) to a mix of primarily crystalline bedrock (Jmu, JTRtk, Ji) and some sedimentary bedrock (Tch). The first, stronger pulse does not show any evidence of being affected by the underlying bedrock at this location. Many velocity profiles also have inflections near the 42–43 km marks (2000-2001, 2001-2002, 2002-2003, 2006-2007, 2008-2009, 2009-2010, 2010-2011), which roughly coincides with the end of the crystalline bedrock and the beginning of the portion of the terminus that has overridden unlithified sediment. The surface slope of Matanuska Glacier steadily declines from 4° near the 10 km mark (Figure 3.21c) to 2° near the 30 km mark, followed by a roughly 5 km stretch of glacier inclined at about 1° between the 34 and 39 km marks. It is worth noting that near the 32 km mark a tributary joins the main trunk on the west side, just up glacier of the flattest portion of Matanuska Glacier.

3.5.5 Copper Glacier

The velocity fields and velocity time-series for Copper Glacier show a pulse between 1999 and 2004 (Figures 3.22, 3.23). The peak of the pulse occurred in 2002, with a velocity of 220.2 m/yr at the 23 km mark; this is an increase of 181% compared to the velocity prior to the pulse in 1999 of 78.2 m/yr (Figure 3.23). It appears Copper Glacier is currently in the acceleration phase of a second pulse; its velocity has been steadily increasing from a low of 57.4 m/yr in 2005 to 172.0 m/yr in 2013, with an anomalous spike in velocity in 2009 of 162.3 m/yr that may be the result of a spring sliding event. The pulses affect the glacier from at least the 12 km mark (the beginning of the glacier's confining valley), down to the terminus at the 29 km mark, a 17 km span that accelerates and then decelerates en masse (Figure 3.24a, b). The velocity profiles of 1995-1996, 1997-1998, 2000-2001, 2001-2002, 2007-2008, 2008-2009, 2009-2010, and 2011-2012 all show an inflection near the 18–19 km marks; this coincides with a change in bedrock geology along the eastern margin from consisting entirely of lava flows (Qwj) to a mix of lava flows and sedimentary rock (QTw). Copper Glacier also narrows slightly in the same area from a width of 1.9 km at the 17 km mark to 1.4 km at the 19 km mark. The surface slope of Copper Glacier is relatively steep before the glacier enters its confining valley, with slopes in excess of 7° near the 12 km mark (Figure 3.24c). After the glacier enters its valley the surface slope decreases significantly; at the 17 km mark the surface slope has reduced to 3° and near the 24 km mark it has reduced to 2°.

3.5.6 Nabesna Glacier

The velocity fields and velocity time-series for Nabesna Glacier (Figures 3.25 and 3.26) show evidence of a single pulse, from 1997 to 2005, an 8 year span, with both the acceleration and deceleration phases each lasting 4 years. The pulse peaked in 2001 at 190.6 m/yr at the 55 km mark. This peak is a 77% increase compared to the velocity prior to the pulse in 1997 of 107.5 m/yr. The pulse appears to affect almost the entire ablation zone of Nabesna Glacier, with the ice from approximately the 30 km mark to the terminus at the 66 km mark (a 36 km span) accelerating and then decelerating en masse. The velocity profiles (Figure 3.27a) show prominent inflections at the 30 km mark, and the surface slope is < 1° here (Fig. 3.27b); this is where ice from the two main lobes of the accumulation area join to form the main trunk of the glacier. At the 44–45 km marks the velocity attains its maximum value for each year; this is where the glacier narrows from approximately 5 km in width up glacier, to roughly 4 km, and it is also where the surface slope increases from roughly 1° up glacier to roughly 2° down glacier. Li et al. (2008) used Interferometric Synthetic Aperture Radar (InSAR) techniques to produce velocity fields for Nabesna Glacier for January and March, 1994, December, 1995, and March/April and May, 1996. The centerline profiles extracted from the InSAR-derived velocity fields are of similar shape and magnitude to the velocity profiles presented here for the mid- to lower ablation zone of Nabesna Glacier, which provides some confidence in the velocity measurements presented in this study. Near the 50 km mark the velocity profiles show a small inflection where the bedrock geology changes from a mix of andesitic lava flows and sedimentary rock (QTw) to basalt lava flows (Trn; Figure 3.7). Further down the glacier, at the 60 km mark, the velocity profiles again show an inflection at a transition in bedrock geology, this time from basalt lava (Trn) to a mix of dacite lava, lahar flows, and volcanic tuff (PPt).

3.5.7 Nizina Glacier

The velocity fields (Figure 3.28) and velocity time-series (Figure 3.29) for Nizina Glacier show that since 1996 it has experienced one complete pulse cycle and is currently in the acceleration phase of a second pulse. From 1998 to 2002 Nizina Glacier slowly increased in velocity from 21.5 m/yr to 66.0 m/yr at the 24 km mark (Figure 3.29), then from 2002 to 2004 the glacier accelerated significantly, increasing its velocity to a peak value of 221.1 m/yr at the 24 km mark, a 235% increase. The glacier decelerated just as rapidly, with its velocity decreasing to 55.5 m/yr by 2006, and then further decreasing to 35.0 m/yr in 2009. The complete pulse cycle, from one local velocity minimum to the next, 1998 to 2009, lasted 11 years. Since 2009 Nizina Glacier has been steadily accelerating in a manner very similar to the acceleration phase of the 1998–2009 pulse. All the ice from the 12 km mark to the terminus at the 30 km mark, an 18 km span, is affected by the pulses, with the ice accelerating and then decelerating en masse (Figure 3.30a, b). Rohn Glacier, which converges with Nizina Glacier at the 22 km mark (see Figure 3.8), is not affected by the pulses (Figure 3.28). However, the convergence of the slower-moving ice of Rohn Glacier does affect Nizina Glacier, as indicated by local velocity minima in the velocity profiles (Figure 3.30a, b) at the 22 km mark. At, or near, the 26 km mark several velocity profiles (2002-2003, 2003-2004, 2004-2005, 2005-2006, and 2011-2012) show a peak velocity. This location coincides with a transition in bedrock geology from basalt lava (Trn) to sedimentary bedrock (Kl, Ku, and Pl). From roughly the 14 km mark to the 25 km mark the surface slope of Nizina Glacier is < 2°, with much of this stretch dipping even more gently at an angle of 1.5°; by the 26–27 km marks the surface slope has increased to 2°, coinciding with the velocity maxima seen in the velocity profiles.

3.5.8 Sanford Glacier

A single pulse was observed to occur on Sanford Glacier from 2000 to 2008, as is seen in the velocity fields (Figure 3.31) and in the velocity time-series (Figure 3.32). Although 1 year of velocity measurements is missing from the time-series (2006) due to lack of available cloud-free imagery, it seems evident from the temporal trajectory of the velocity measurements at the 20.5 km mark (Figure 3.32) that the pulse did occur. However, due to the missing data, it is not clear when the peak of the pulse occurred, whether it was in 2005 or 2006; and it is not clear whether the deceleration phase lasted 3 years (from 2005 to 2008) or only 2 years (from 2006 to 2008). The observed part of the acceleration phase lasted from 2000 to 2005, and represents a 216% increase in velocity, from 32.1 m/yr to 101.7 m/yr at the 20.5 km mark. The ice from the 13 km mark to approximately the 27 km mark was affected by the pulse, a 14 km span that accelerated and then decelerated en masse; the lowest 3 km of the glacier nearest the terminus was unaffected by the pulse. The velocity profiles (Figure 3.33a) show a local velocity minimum at the 18 km mark where a slower-moving tributary joins the main trunk of Sanford Glacier along the northeast margin (see Figure 3.9). Immediately down glacier, at the 21 km mark, the velocity profiles show a local velocity maximum that coincides with a change in bedrock geology along the northern margin from andesite and dacite lava flows (Qws) to a mix of andesite and dacite lava flows and sedimentary bedrock (QTw). In this same area the surface slope of Sanford Glacier is at its minimum, 1.8°; at all other locations on the glacier the surface slope is > 2° (Figure 3.33b).

3.6 Discussion

Sections 3.6.1 through 3.6.4 discuss accepted or proposed glaciologic theory concerning the characteristics of pulsing glaciers, overdeepenings, basal hydrology, glaciohydraulic supercooling, and till deposition, deformation and erosion. These processes are then linked in a chain of events to explain why pulses are cyclical in Section 3.6.5.

3.6.1 Physical Characteristics of Pulsing Glaciers

Given the spatial and temporal patterns in velocity and physical descriptions of the eight glaciers in this study, as well as Ruth Glacier (Turrin et al., in review), it is possible to identify some common characteristics of pulsing glaciers. The part of the glaciers in which the spatiotemporal pattern of velocity indicates pulsing behavior (i.e., a multiyear acceleration phase followed by a multiyear deceleration phase, and the lack of a kinematic wave) is always located where the ice surface has the shallowest slope, which is generally in the range of 1–2°. The exception to this is Nabesna Glacier which has a surface slope of 2° where the pulse most strongly affected the glacier, but a shallower slope of 1° up glacier, near the 30 km mark (Figure 3.27b) where the effect of the pulse diminishes. The pulses of Capps, Copper, Kahiltna, Nabesna, and Ruth glaciers all occur where the glacier either increases in width after exiting a constricted area (Ruth, Kahiltna), or after exiting its confining valley (Capps), or within its confining valley (Copper). In all these instances, the constrictions appear to be controlled by the underlying bedrock lithology and involve a transition from crystalline bedrock, such as granite or basalt, to sedimentary bedrock. Again, the exception is Nabesna Glacier, which involves a transition from a mix of lava and sedimentary bedrock to strictly lava. The pulses of Eldridge, Matanuska, Nizina, and Sanford glaciers all occur where one or more tributary glaciers merge with the main ice trunk. In each case the tributary glaciers are moving slowly compared to the main trunks they join, and in each case the tributary glaciers are of noteworthy size and likely contributed significant mass to the main trunks during previous ice ages. Although there are some transitions in bedrock lithology that coincide with the union of tributary glaciers and their main trunks (Eldridge, Nizina), it does not appear that the merging of glaciers is controlled by the underlying bedrock lithology.

3.6.2 Formation and Characteristics of Overdeepenings

A glacial overdeepening is a bowl-shaped depression beneath a glacier with a bottom that is lower in elevation than the glacier base immediately down valley; thus, the glacier is “overly deep” at this location. Overdeepenings typically have steeply inclined headwalls at their up glacier extents and gently inclined slopes at their down valley extents that dip opposite in direction of the glacier surface slope (Hooke, 2005); thus, the down valley slope is often referred to as the adverse slope (Figure 3.34a). Overdeepenings can be found in cirques, at glacier confluences, valley constrictions, beneath glacier termini, or where a change in geologic structure or lithology occurs (Cook & Swift, 2012). In each of these cases, the overdeepening is formed due to increased erosion beneath the glacier, caused either by an increase in ice flux or a decrease in the ability of the bedrock to withstand erosive forces. The circumstances listed above that can lead to the formation of overdeepenings are common in alpine environs; therefore, overdeepenings are common and can be found at all elevations in the glacial landscape (Hooke, 2005).

An overdeepening begins as a basal step beneath a glacier, for instance, just down glacier from where a tributary merges with a main glacier trunk. The increase in ice flux at the confluence of the two ice masses causes increased erosion at the glacier base, forming the step (Penck, 1905). The convex shape of the basal step causes extension of the ice surface as the glacier flows over it, resulting in crevasses above the step. The crevasses act as preferential waterways, directing melt water to the head of the step, increasing basal sliding locally at the base of the headwall of the step, thus further increasing erosion there. Increased erosion at the base of the headwall increases its slope and enhances its convex shape, thus increasing ice surface extension and crevassing above it (Hooke, 2005). This positive feedback promotes transformation of basal steps into overdeepenings. The ice surface above overdeepenings tends towards shallow slopes because the ice velocity is greater in the overdeepening relative to down glacier, due to basal slip and till deformation. The increased velocity causes ice extension within the overdeepening and ice compression immediately down glacier that reduces the ice surface slope locally (Cook & Swift, 2012).

Glacier overdeepenings form in the same type of locations in which glacier pulses are observed to occur (at glacier confluences, valley restrictions, or changes in bedrock lithology), and overdeepenings are known to have flat ice surface slopes, just as observed at the locations where pulses occur. Consequently, it is concluded that pulses occur where glaciers are overdeepened. There is some field evidence to prove a few of the glaciers discussed above are overdeepened in the location of the pulses. There is a single ice depth measurement of Ruth Glacier within the Great Gorge via seismic methods (unpublished data by K. Echelmeyer) that found the ice to be up to 1150 m thick in 1983. As Ward et al. (2012) note, ice this thick places the bottom of the Great Gorge at approximately the same elevation as the terminus, nearly 40 km further down valley. This strongly suggests the Great Gorge of Ruth Glacier is overdeepened. The ice thickness of Capps Glacier was measured using a monopulse ice-radar (March et al., 1997). It was found to be between 700 and 800 m thick in its main trunk between the 20 and 27 km marks, where the glacier is most narrow, before it spreads laterally and forms the piedmont lobe. The surface elevation along this part of the glacier is between 600 and 800 m above sea level (m.a.s.l.) and the glacier terminus is approximately 150 m.a.s.l. (Figure 3.18c). Therefore, the base of the glacier is at, or below, sea level between the 20 and 27 km marks and definitely overdeepened there. In fact, the data suggest the overdeepening extends well into the piedmont lobe to at least the 35 km mark, because the ice thickness is still greater than the surface elevation there, indicating the glacier base resides below sea level and must be overdeepened. It is worth noting this is the portion of Capps Glacier that pulsed.

3.6.3 Basal Hydrology and Supercooling in Overdeepenings

The subglacial hydraulic system beneath overdeepenings is a distributed cavity system with high water pressure and slow flow that transitions to a channelized system with faster flow at the distal parts of the adverse slope (Alley, et al., 2003; Creyts et al, 2013; Hooke, 2005). High water pressures have been observed via field studies of overdeepenings on Storglaciären, Sweden (Jansson, 1996) and Washmawapta Glacier, British Columbia (Dow et al., 2011), and have also been predicted by numerical modeling (Creyts et al., 2013). The high water pressure beneath an overdeepening is a result of constriction of the drainage channels along the adverse slope due to glaciohydraulic supercooling. Supercooling of subglacial water occurs within overdeepenings due to the increased ice thickness there depressing the pressure-melting point (at a rate of -0.001° C/m), which allows subglacial water to remain liquid below 0° C. As an example, beneath the Great Gorge of Ruth Glacier, the pressure-melting point would be reduced to -1.15° C, based on its previously stated ice thickness. As the supercooled water traverses the adverse slope to exit the overdeepening, the glacier thins along the slope (Figure 3.34) and the pressure-melting point rises faster than the water can warm via viscous heating, so the water freezes onto the walls of the drainage channels, constricting them, or clogging them with frazil ice (ice platelets). Consequently, the water pressure rises and water is forced to spread laterally in the distributed cavity system within the overdeepening (Alley et al., 2003; Hooke, 2005).

Whether the supercooled water actually freezes as it traverses the adverse slope, or not, depends upon the rate at which the pressure-melting point rises, which in turn is determined by the ratio of the angle of the adverse slope to the angle of the ice surface slope. The supercooling threshold is defined as the critical angle of the adverse slope such that water moving along it will freeze. Hooke (1989) estimated the supercooling threshold to be between 1.5 and 2.0, and Clarke (2005) estimated it to be between 1.3 and 1.6. So, if the adverse slope is approximately 1.3 to 2.0 times steeper than the ice surface slope directly above, water will freeze in its subglacial channels rather than exiting the overdeepening. Based on these supercooling threshold values and the surface slopes mentioned previously, the adverse slopes necessary for supercooling to occur range from 1.9°–3.0° for Ruth, Kahiltna, and Nizina glaciers, 2.6°–4.0° for Eldridge, Capps, Nabesna, Matanuska, and Sanford glaciers, and from 3.9°–6.0° for Copper Glacier. All of these scenarios require only gentle adverse slopes (only twice the surface slope, or less), suggesting the supercooling condition is easily met. Evidence for supercooling, such as frazil ice and ice growth around subglacial discharge vents, has been found on Matanuska (Evenson et al., 1999a), Malaspina, and Bering glaciers in Alaska (Evenson et al., 1999b), and Skeidaràrjökull, Skaftafellsjökull, and Kviarjökull, which are outlet glaciers of the Vatnajökull icecap, Iceland (Evenson et al., 2001). Also, evidence for constricted flow in an overdeepening has been found on Storglaciären, Sweden (Hooke & Pohjola, 1994) by the slow movement of tracer dyes through cavities beneath the glacier, observed via boreholes drilled into the base of the overdeepening.

3.6.4 Till Deposition, Deformation, and Erosion

As glaciohydraulic supercooling causes subglacial drainage channels along an adverse slope to become constricted, thereby elevating water pressure in the distributed cavity system within the overdeepening, the hydraulic gradient within the overdeepening decreases. The reduced gradient results in slower water flow such that sediment is no longer evacuated from the overdeepening; instead, it is deposited as a subglacial till. Thus, the overdeepening is transformed from an area of sediment erosion and transportation, to one of sediment deposition (Alley et al., 2003). The till will accumulate until the rate of down glacier sediment transport by deformation and entrainment within the ice is equal to the rate of erosion. Eventually, the till layer becomes thick enough to protect the bedrock beneath the overdeepening and adverse slope from further erosion, allowing erosion to concentrate at the headwall (Hooke, 2005).

Water pressure within an overdeepening can approach flotation levels, indicating that the weight of the overlying ice is supported by the water pressure, thus the effective pressure upon the till is zero. When this occurs, the till dilates (Willis, 1995) because it is no longer being compacted by the weight of the overlying glacier. A dilated till cannot support the shear stress between the overlying glacier (which wants to flow down valley due to longitudinal stresses) and underlying bedrock (which is stationary), so the till deforms. Till deformation allows the glacier to accelerate locally, transferring shear stress to the immediate surroundings, and assuming the till in the immediate neighborhood is at or near its deformation threshold (due to high water pressure), these areas also deform and allow ice acceleration. The result is a cascade of till failure, ice acceleration, and stress transfer that activates more and more distant areas within the overdeepening (Frappé & Clarke, 2007; Nolan, 2003; Truffer et al., 2000); thus, a pulse occurs.

Alley et al. (2003) proposed a theory of subglacial sediment deposition and erosion within overdeepenings that promotes equilibrium between the two processes. The theory is based upon field work performed mostly on the terminus of Matanuska Glacier where the ice has overridden unlithified sediment and an overdeepening exists (Alley, et al., 1998; Lawson et al., 1998). As sediment accumulates in the overdeepening, the angle of the adverse slope is reduced, changing the ratio of the adverse slope to the ice surface slope and eventually halting supercooling, because the supercooling threshold is no longer surpassed. Once supercooling ceases, the drainage pathways along the adverse slope can open because the water no longer freezes, there is sufficient viscous heating to keep the water liquid and to melt channel walls and keep them open and expand them. The free-flowing hydraulic system sufficiently drains the deeper parts of the overdeepening to reduce water pressure there and cause the till to consolidate. The increased water flow begins the process of sediment erosion and transport. Over time, enough sediment is evacuated that the angle of the adverse slope is increased again to the supercooling threshold. Thus, sediment deposition and erosion work in tandem to continually arrange the longitudinal profile of an overdeepening to be at or near the supercooling threshold (Alley et al., 2003). Results from numerical modeling seem to confirm this theory. Creyts et al. (2013) used a 1-dimensional model to simulate water flow and sediment transport through an overdeepening. The model showed that when the angle of the adverse slope is less than the supercooling threshold, sediment deposition occurs in the overdeepening and along the adverse slope, ice does not accrete via supercooling in channels, and water flow is relatively fast through the overdeepening and up the adverse slope, as predicted by Alley et al. (2003). Alternatively, if the angle of the adverse slope is at the supercooling threshold, then sediment deposition occurs in the overdeepened area and along most of the adverse slope. Maximum deposition occurs where the adverse slope begins and tapers along the slope until there is minor erosion at its most distal part; the net effect is to reduce the overall angle of the adverse slope and cause supercooling to cease, also as predicted by Alley et al. (2003).

3.6.5 Mechanism for Cyclical Pulses

The theory presented by Alley et al. (2003) for stabilization of the basal longitudinal profile of overdeepened glaciers at the supercooling threshold (summarized above) is for overdeepenings carved into unlithified sediment near the glacier terminus, where ice velocity is slowest and dynamic effects may be ignored. The pulses observed in this study and on Ruth Glacier (Turrin et al., in review) occur in the mid- to upper ablation zone where the glaciers are moving rapidly compared to their termini, so dynamic effects must be accounted for. Presented next is a mechanism to explain the cyclical dynamic behavior of some pulsing glaciers that incorporates the theory of Alley et al. (2003) and which also includes the effects of glacier dynamics.

First, begin with an overdeepening that contains a consolidated till within the deeper parts of the overdeepening and along the adverse slope (Figure 3.34a, profile view), a distributed cavity drainage system along much of the overdeepening and a channelized drainage system along part of the adverse slope (Figure 3.34a, plan view), and a ratio of adverse slope to ice surface slope at the supercooling threshold. In this configuration water pressure is relatively low, there is no till deformation and the glacier is in between pulses, and so ice motion is slow.

Second, supercooling causes the channelized drainage system along the adverse slope to become constricted (Figure 3.34b, plan view) by freezing of water as it exits the overdeepening. This causes high water pressure in the drainage system that in turn causes the till to dilate and deform. The resulting shear in the till allows the glacier to accelerate, beginning a pulse. Transfer of shear stress allows the area of till failure beneath the glacier to expand; accelerating the glacier further. This is the acceleration phase of a pulse (Figure 3.34d). As the glacier accelerates, the increased compressive strain rate above the adverse slope causes ice to thicken there, and thicker ice from deeper parts of the overdeepening is transported into locations previously occupied by thinner ice along the adverse slope, thickening the ice further (Figure 3.34b, profile view); at the same time the constricted channels along the adverse slope cause an increase in water velocity that results in sediment erosion. So, while the glacier is accelerating, these two processes (ice thickening and sediment erosion) are working in tandem to change the ratio of adverse slope to surface slope.

Third, eventually the ratio of the angles of adverse slope to surface slope is reduced such that supercooling no longer occurs. When this happens the pressure-melting point has been sufficiently reduced along the adverse slope so that water traversing it has enough viscous energy to melt channel walls, expanding them (Figure 3.34c, plan view). The expanded drainage channels allow free flow of water out of the overdeepening, de-pressurizing the distributed cavity system and causing the till to consolidate, which causes the glacier to decelerate. This is the deceleration phase of the pulse (Figure 3.34d). Deceleration reduces the compressive strain rate above the adverse slope and slows the transport of thicker ice up the adverse slope so that ice-thickening decreases, and eventually ceases, and ablation begins to thin the ice there (Figure 3.34c, profile view). Meanwhile, the slower water flow of the depressurized drainage system allows sediment accumulation along the adverse slope. Eventually, ablation of the ice surface, and sediment deposition along the adverse slope, return the glacier to its prepulse geometry at the supercooling threshold, and the cycle repeats.

This model combines the processes of till transportation, erosion and deposition, basal hydraulics and thermodynamics, ice dynamics, surface mass balance and glacier geometry in a chain of events that produces periodic ice motion in an overdeepening. In spite of the diversity of surface and subglacial processes that are incorporated into the model, it is primarily dependent upon climate and bedrock lithology. For instance, climate determines ice accumulation and ablation on the glacier surface, which in turn determines the rate at which the surface slope returns to its prepulse angle after supercooling stops; so climate helps determine the rate at which pulses cease. Accumulation and ablation rates also determine ice flux (ice thickness multiplied by the rate of ice flow) and the amount of melt water available to enter the subglacial hydraulic system, which combine to determine the rates of bedrock erosion, and sediment production and transport. Climate also influences the rate at which a pulse will achieve its peak by influencing strain thickening (velocity gradient multiplied by ice thickness) above the adverse slope. Greater strain thickening causes greater changes in surface slope and a more rapid end to supercooling. As shown in the Results section, bedrock lithology directly influences glacier geometry (width, thickness, and surface slope), which in turn affects glacier velocity, strain thickening, bedrock erosion, and sediment transport. Thus, bedrock lithology can influence where overdeepenings occur, the amount of till accumulation, deformation and erosion, the angle of the adverse slope, the supercooling threshold, and how rapidly pulses begin and end. In general, temperate glaciers with a high mass turnover (high snow accumulation in winter plus high ablation in summer), and a combination of valley configuration and bedrock lithology that produces an overdeepening, are most likely to pulse. Outside of southern Alaska, some regions that may have the requisite conditions include Patagonia, New Zealand, and Iceland.

3.6.6 Characteristics of Nonpulsing Glaciers

Of the 90 glaciers examined in Alaska, nine were positively identified as pulse-type, leaving 81 glaciers as either nonpulsing or possibly (but not positively) of pulse-type. As noted earlier, the pulsing glaciers have physical characteristics that suggest they are overdeepened at the location of the pulses, such as low surface slopes, and lateral constrictions or junctions with major tributaries. It is worthwhile to examine the non-pulsing glaciers to determine whether they have similar or different physical characteristics and compare them to the pulsing glaciers.

Fifty-three glaciers had velocity fields that were spatially or temporally too incomplete to identify pulses even if they did occur, so the physical characteristics of these glaciers were not examined. Clouds, cloud shadows, and a lack of suitable surface features to track were the main factors contributing to the incomplete velocity fields for these glaciers. A few glaciers are tidewater (Columbia, Harvard) or lake-calving (Knik) glaciers that appear to be moving too rapidly for pulsing to occur, so the physical characteristics of these glaciers were not examined because their behavior is determined by tidewater dynamics.

Eighteen glaciers had velocity fields of sufficient spatiotemporal density to identify pulses if they occurred, yet pulsing behavior was not observed on them. Of these 18 glaciers, 6 glaciers had none of the physical characteristics associated with an overdeepening. Seven of the 18 glaciers have junctions with major tributaries, but lack the shallow surface slope associated with an overdeepening where the tributary joins with the main glacier trunk. These glaciers widen their valleys to accommodate the additional ice flux from their tributaries, instead of deepening their valleys, so no overdeepenings are formed. The lone exception among this group of 7 glaciers is Yentna Glacier, in the Central Alaska Range, which does not widen where tributaries join it in the upper ablation zone, instead the ice velocity steadily increases as one progresses downglacier to accommodate the additional ice flux from the tributaries. The increased ice velocity will cause Yentna Glacier to carve deeper into its valley, but the lack of any significant flattening of the surface slope suggests there is no overdeepening. Instead, Yentna Glacier probably has basal steps that coincide with each tributary. The medial moraines in the upper ablation zone of Yentna Glacier are not wavy, nor convolute, so it has no sign of past pulsing or surging behavior.

Five of the 18 glaciers with spatially and temporally dense velocity fields possessed both characteristics of overdeepenings, having either a lateral constriction or a major tributary, and a shallow surface slope at the same location. It is suggested these glaciers are overdeepened, but do not pulse. This could occur if the overdeepenings are not deep enough, or the ice not thick enough, to sufficiently depress the pressure-melting point and adequately supercool the basal water; consequently, the water will not freeze as it exits the overdeepening. The absence of pulsing behavior might also be due to an adverse slope so gently inclined that the pressure-melting point changes slowly enough along its length to allow viscous heating to warm the water fast enough to prevent freezing in the drainage channels. It is also possible the drainage system in an overdeepening is sufficiently isolated from the rest of the glacier such that the water pressure is never great enough to cause till dilation. This may happen when englacial drainage conduits bypass the overdeepening by going around or above the overdeepening, and causing it to be hydraulically isolated (Fountain & Walder, 1998). Without sufficient water influx, the linked-cavity system within an overdeepening may never pressurize sufficiently to cause till dilation and the glacier will not pulse. It is also possible these 5 glaciers did pulse, but the pulses were not detected. As noted above, Black Rapids Glacier pulsed twice during the 1980s and 1990s (Nolan, 2003), but these pulses could not be detected in the velocity fields produced in this study, due to a lack of suitable surface features to track, occasionally patchy snow cover, clouds, and lack of available imagery during the 1990s. If the pulses of Black Rapids Glacier could not be detected using optical feature tracking, then it is possible other glaciers observed in this study also pulsed, but their pulses were not detected.

Of the 81 nonpulsing glaciers, 6 of them are suspected to have pulsed: Triumvirate Glacier and an unnamed glacier east of Barrier Glacier at 61° 16’ 00” North latitude, -152° 5’ 21.89” West longitude in the West Alaska Range, Trident Glacier in the East Alaska Range, Stephens Glacier and Tazlina Glacier in the Chugach Mountains, and an unnamed glacier in the Wrangell Mountains west of Copper Glacier at 62° 6’ 55.01” North latitude, -143° 51’ 4.73” West longitude. Each of these 6 glaciers has an obvious lateral constriction or junction with a major tributary, and all have an associated shallow surface slope indicating the presence of an overdeepening at the same location. The velocity fields for these 6 glaciers suggest they have pulsed, but their spatiotemporal velocity signatures are not sufficiently well-defined to positively identify pulsing behavior, therefore they were excluded from the group of 8 pulsing glaciers presented here.

All 9 glaciers discussed in this study that definitely pulsed have obvious physical characteristics indicating the presence of an overdeepening. All glaciers with spatially and temporally complete velocity fields and only 1, or 0, physical characteristics of an overdeepening definitely did not pulse. Eleven glaciers were identified with both characteristics of overdeepenings, but either they did not pulse, or their pulses could not be positively identified. So, it appears pulsing behavior requires a glacier to be overdeepened (as shown above), but the presence of an overdeepening does not guarantee pulsing behavior.

3.6.7 Pulse Synchronicity and Climate

Four glaciers, Kahiltna, Capps, Matanuska, and Nabesna, all had pulses that peaked in 2001, while 3 glaciers, Kahiltna, Matanuska, and Ruth each had pulses that peaked in 2010, and 2 glaciers, Eldridge and Nizina, both had pulses that peaked in 2004 (Figure 3.35). So, there appears to be some limited synchronicity of the pulse cycles among the 9 glaciers across mountain ranges. Fowler and Schiavi (1998) suggest that synchronicity among surging ice streams of the Laurentide Ice Sheet (as proposed by Bond and Lotti [1995]) is not surprising because they were coupled via climate, and they note that even weakly coupled nonlinear dynamic systems become synchronized. This same argument can be made for glaciers of southern Alaska; they are coupled by the predominant flow of weather patterns around the Gulf of Alaska. Even though glaciers further inland, such as in the Alaska Range, experience drier, colder conditions, they are still (perhaps weakly) coupled to glaciers along the coast, and thus over time they can synchronize with their counterparts to the south.

Considering the extent to which climate influences so many of the individual processes constituting the complete pulse mechanism described herein, it should be no surprise that some limited synchronicity among pulsing glaciers exists. As an example of how annual meteorological conditions can influence the pulse cycle and cause synchronicity among glaciers, Positive Degree Days (PDDs) at the Talkeetna Airport (62.3° N, -150.1° W, 107.9 m.a.s.l.; http://www.ncdc.noaa.gov/oa/climate/ghcn-daily) were compared to the normalized velocity of the 9 pulsing glaciers (Figure 3.35). PDDs are a measure of the accumulated temperature above freezing at a location and are often used as a proxy for melt water production on the surface of a glacier. A spike in PDDs occurred in 2010, the same year pulses of Kahiltna, Matanuska, and Ruth glaciers peaked. These three glaciers were already in their acceleration phases, so additional melt water entering the glacier and reaching the base would enhance the process of till dilation and deformation, allowing the glacier to accelerate further, producing greater thickening of the ice such that the supercooling threshold is no longer surpassed. Thus, the pulse reaches its peak and the deceleration phase begins. The fact that 4 glaciers' pulses peaked in 2001, yet there is no obvious peak in PDDs that year, and the correlation between PDDs and the number of pulse peaks per year yields an R-squared value of 0.05, both indicate there are other unidentified variables that influence pulse synchronization.

3.7 Conclusions and Future Work

A systematic velocity survey of the largest glaciers of the Alaska Range, Chugach Mountains, and Wrangell Mountains in southern Alaska revealed 8 glaciers that have pulsed within the past 4 decades. These 8 glaciers, Kahiltna, Eldridge, Capps, Copper, Sanford, Nizina, Nabesna, and Matanuska, have common characteristics where their pulses occurred. Each of them has shallow surface slopes in the range of 1 to 2°, and they are either constricted by their confining valleys or joined by a major tributary at these same locations, suggesting the pulses occur where the glaciers are overdeepened. Based on the idea that the glaciers are overdeepened, and incorporating a previous theory that says adverse slopes of glacier overdeepenings tend towards the supercooling threshold (Alley et al., 2003), a mechanism to explain the cyclical behavior of pulsing glaciers is presented. The mechanism accounts for the effects of glacier dynamics, ablation, and sediment transport to show that the pressure-melting point along an adverse slope oscillates above and below the supercooling threshold due to sediment accumulation and erosion and ice thickening and thinning. The effect of this oscillation is to periodically pressurize the subglacial drainage system sufficiently to allow the till to dilate and deform, causing the glacier to accelerate, followed by deceleration after supercooling ceases and the drainage system depressurizes, allowing the till to consolidate. The entire cycle typically lasts 6 to 9 years and is controlled primarily by climate and bedrock lithology. The widespread existence of such pulsing glaciers, and the ease in which their behavior may be overlooked, suggests caution should be exercised when interpreting velocity changes over years or decades, because not all changes in glacier motion are a direct result of local meteorological conditions. Basal conditions can exert a greater influence on glacier dynamics than climate over the life of a pulse cycle.

Time-series of velocity maps for glaciers of other mountain ranges, such as the St. Elias Mountains in southern Alaska or those listed earlier, would help refine, or refute, the model presented here. A mathematical or computer simulation of an overdeepening that incorporated the processes described herein could help validate the model, assuming it produces cyclical flow as predicted, and would also help identify which processes are most influential and sensitive dependencies among variables. A field campaign to a glacier in midpulse would provide the strongest evidence for, or against, the proposed model. For example, Nizina Glacier currently appears to be in the acceleration phase and would be a good choice. Airborne or ground-based radar, or seismic methods, could be used to map the basal topography and ice thickness and confirm the presence of an overdeepening. A steam drill could be used to drill boreholes through the ice to the glacier base. This would help confirm the presence of a subglacial till, and the till's thickness, lithology, and grain size distribution could be measured. Borehole water pressure measurements could be taken to verify that water pressures are near flotation levels during the pulse, and the water temperature could be measured to verify it is supercooled. A plough-meter could be installed down the borehole and into the till to verify and measure the amount of glacier motion due to till deformation. Along the glacier margins and at the terminus, evidence could be sought to verify that the supercooling threshold is currently, or has been previously exceeded. This evidence might include emergence of supercooled water along the glacier margins, frazil ice surrounding the springs that emit supercooled water, or the existence of sediment and frazil ice-filled bottom crevasses or stratified debris-laden basal ice (Lawson et al., 1998).

Table 3.1 Landsat image pairs used to produce velocity fields for the Central Alaska Range.

Path/Row	Date 1	Sensor	Path/Row	Date 2	Sensor
WRS1 76/16	24-Sep-73	MSS 1	WRS1 76/16	27-Jul-74	MSS 1
WRS1 76/16	27-Jul-74	MSS 1	WRS1 76/16	23-Sep-75	MSS 2
WRS1 76/16	23-Sep-75	MSS 2	WRS1 76/16	7-Jul-76	MSS 2
WRS1 76/16	7-Jul-76	MSS 2	WRS1 76/16	1-Jul-77	MSS 2
WRS1 76/16	1-Jul-77	MSS 2	WRS1 76/16	2-Aug-78	MSS 2
WRS1 76/16	2-Aug-78	MSS 2	WRS1 76/16	22-Jul-80	MSS 2
WRS1 76/16	22-Jul-80	MSS 2	WRS1 76/16	4-Aug-81	MSS 2
WRS1 76/16	4-Aug-81	MSS 2	WRS1 76/16	3-Jul-82	MSS 3
WRS1 76/16	3-Jul-82	MSS 3	WRS2 70/16	18-Aug-83	MSS 4
WRS2 70/16	18-Aug-83	MSS 4	WRS2 70/16	28-Aug-84	MSS 5
WRS2 70/16	28-Aug-84	MSS 5	WRS2 70/16	16-Sep-85	MSS 5
WRS2 70/16	16-Sep-85	TM 5	WRS2 70/16	17-Jul-86	TM 5
WRS2 70/16	17-Jul-86	TM 5	WRS2 70/16	21-Aug-87	TM 5
WRS2 70/16	21-Aug-87	TM 5	WRS2 70/16	29-Jun-91	TM 5
WRS2 70/16	29-Jun-91	TM 5	WRS2 70/16	26-Aug-92	TM 4
WRS2 70/16	26-Aug-92	TM 4	WRS2 70/16	9-Sep-94	TM 5
WRS2 70/16	9-Sep-94	TM 5	WRS2 70/16	8-Jun-95	TM 5
WRS2 70/16	8-Jun-95	TM 5	WRS2 70/16	19-Jun-99	TM 5
WRS2 70/16	19-Jun-99	TM 5	WRS2 70/16	16-Aug-00	ETM+7
WRS2 70/16	10-Apr-00	ETM+7	WRS2 70/16	29-Apr-01	ETM+7
WRS2 70/16	29-Apr-01	ETM+7	WRS2 70/16	16-Apr-02	ETM+7
WRS2 70/16	16-Apr-02	ETM+7	WRS2 70/16	3-Apr-03	ETM+7
WRS2 70/16	9-Aug-03	ETM+7	WRS2 70/16	10-Jul-04	ETM+7
WRS2 70/16	10-Jul-04	ETM+7	WRS2 70/16	14-Aug-05	ETM+7
WRS2 70/16	14-Aug-05	ETM+7	WRS2 70/16	10-Sep-06	TM 5
WRS2 70/16	10-Sep-06	TM 5	WRS2 70/16	28-Aug-07	TM 5
WRS2 70/16	28-Aug-07	TM 5	WRS2 70/16	5-Jul-08	ETM+7
WRS2 70/16	5-Jul-08	ETM+7	WRS2 70/16	8-Jul-09	ETM+7
WRS2 70/16	8-Jul-09	ETM+7	WRS2 70/16	20-Aug-10	TM 5
WRS2 70/16	20-Aug-10	TM 5	WRS2 70/16	6-Jul-11	TM 5
WRS2 70/16	18-Oct-11	ETM+7	WRS2 70/16	20-Oct-12	ETM+7

Table 3.2 Landsat image pairs used to produce velocity fields for the West Alaska Range.

Path/Row	Date 1	Sensor	Path/Row	Date 2	Sensor
WRS1 76/17	24-Sep-73	MSS 1	WRS1 76/17	14-Aug-74	MSS 1
WRS1 76/17	14-Aug-74	MSS 1	WRS1 76/17	23-Sep-75	MSS 2
WRS1 76/17	23-Sep-75	MSS 2	WRS1 76/17	30-Aug-76	MSS 2
WRS1 76/17	30-Aug-76	MSS 2	WRS1 76/17	2-Aug-78	MSS 2
WRS1 76/17	2-Aug-78	MSS 2	WRS1 76/17	24-Aug-79	MSS 3
WRS1 76/17	24-Aug-79	MSS 3	WRS1 76/17	22-Jul-80	MSS 2
WRS1 76/17	22-Jul-80	MSS 2	WRS1 76/17	4-Aug-81	MSS 2
WRS1 76/17	6-May-81	MSS 2	WRS1 76/17	4-Apr-82	MSS 3
WRS1 76/17	3-Jul-82	MSS 3	WRS2 70/17	2-Aug-83	MSS 4
WRS2 70/17	2-Aug-83	MSS 4	WRS2 70/17	12-Aug-84	MSS 5
WRS2 70/17	12-Aug-84	MSS 5	WRS2 70/17	16-Sep-85	MSS 5
WRS2 70/17	16-Sep-85	TM 5	WRS2 70/17	17-Jul-86	TM 5
WRS2 70/17	17-Jul-86	TM 5	WRS2 70/17	21-Aug-87	TM 5
WRS2 70/17	15-Sep-99	ETM+7	WRS2 70/17	16-Aug-00	ETM+7
WRS2 70/17	12-May-00	ETM+7	WRS2 70/17	29-Apr-01	ETM+7
WRS2 70/17	16-Jun-01	ETM+7	WRS2 70/17	18-May-02	ETM+7
WRS2 70/17	5-Jul-02	ETM+7	WRS2 70/17	9-Aug-03	ETM+7
WRS2 70/17	9-Aug-03	ETM+7	WRS2 70/17	10-Jul-04	ETM+7
WRS2 70/17	10-Jul-04	ETM+7	WRS2 70/17	14-Aug-05	ETM+7
WRS2 70/17	24-Apr-05	ETM+7	WRS2 70/17	27-Apr-06	ETM+7
WRS2 70/17	27-Apr-06	ETM+7	WRS2 70/17	30-Apr-07	ETM+7
WRS2 70/17	28-Aug-07	TM 5	WRS2 70/17	6-Aug-08	ETM+7
WRS2 70/17	6-Aug-08	ETM+7	WRS2 70/17	30-Jun-09	TM 5
WRS2 70/17	30-Jun-09	TM 5	WRS2 70/17	20-Aug-10	TM 5
WRS2 70/17	8-May-10	ETM+7	WRS2 70/17	9-Apr-11	ETM+7
WRS2 70/17	20-Aug-10	TM 5	WRS2 70/17	15-Aug-11	ETM+7
WRS2 70/17	9-Apr-11	ETM+7	WRS2 70/17	27-Apr-12	ETM+7
WRS2 70/17	27-Apr-12	ETM+7	WRS2 70/17	14-Apr-13	ETM+7

Table 3.3 Landsat image pairs used to produce velocity fields for the Chugach Mountains.

Path/Row	Date 1	Sensor	Path/Row	Date 2	Sensor
WRS1 73/17	8-Sep-72	MSS 1	WRS1 73/17	16-Aug-73	MSS 1
WRS1 73/17	16-Aug-73	MSS 1	WRS1 73/17	6-Jul-74	MSS 1
WRS1 73/17	25-Apr-74	MSS 1	WRS1 73/17	11-Apr-75	MSS 2
WRS1 73/17	10-Jul-75	MSS 2	WRS1 73/17	2-Oct-76	MSS 2
WRS1 73/17	2-Oct-76	MSS 2	WRS1 73/17	22-Aug-77	MSS 2
WRS1 73/17	22-Aug-77	MSS 2	WRS1 73/17	26-Aug-78	MSS 3
WRS1 73/17	26-Aug-78	MSS 3	WRS1 73/17	8-Sep-79	MSS 3
WRS1 73/17	8-Sep-79	MSS 3	WRS1 73/17	24-Aug-80	MSS 2
WRS1 73/17	24-Aug-80	MSS 2	WRS1 73/17	21-May-81	MSS 2
WRS1 73/17	21-May-81	MSS 2	WRS1 73/17	25-May-82	MSS 3
WRS1 73/17	23-Aug-82	MSS 3	WRS2 67/17	28-Jul-83	MSS 4
WRS1 70/17	28-Jul-83	MSS 4	WRS1 70/17	20-Jun-84	MSS 5
WRS1 70/17	20-Jun-84	MSS 5	WRS1 70/17	11-Sep-85	MSS 5
WRS2 67/17	11-Sep-85	MSS 5	WRS2 67/17	28-Jul-86	TM 5
WRS2 67/17	28-Jul-86	TM 5	WRS2 67/17	15-Jul-87	TM 5
WRS2 67/17	15-Jul-87	TM 5	WRS2 67/17	12-Jul-89	TM 4
WRS2 67/17	10-Sep-99	ETM+7	WRS2 67/17	11-Aug-00	ETM+7
WRS2 67/17	11-Aug-00	ETM+7	WRS2 67/17	15-Sep-01	ETM+7
WRS2 67/17	15-Sep-01	ETM+7	WRS2 67/17	1-Aug-02	ETM+7
WRS2 67/17	1-Aug-02	ETM+7	WRS2 67/17	19-Jul-03	ETM+7
WRS2 67/17	19-Jul-03	ETM+7	WRS2 67/17	30-Aug-04	TM 5
WRS2 67/17	30-Aug-04	TM 5	WRS2 67/17	9-Aug-05	ETM+7
WRS2 67/17	9-Aug-05	ETM+7	WRS2 67/17	13-Sep-06	ETM+7
WRS2 67/17	13-Sep-06	ETM+7	WRS2 67/17	28-Jun-07	ETM+7
WRS2 67/17	28-Jun-07	ETM+7	WRS2 67/17	1-Aug-08	ETM+7
WRS2 67/17	1-Aug-08	ETM+7	WRS2 67/17	5-Sep-09	ETM+7
WRS2 67/17	5-Sep-09	ETM+7	WRS2 67/17	16-Sep-10	TM 5
WRS2 67/17	16-Sep-10	TM 5	WRS2 67/17	11-Sep-11	ETM+7
WRS2 67/17	11-Sep-11	ETM+7	WRS2 67/17	27-Jul-12	ETM+7
WRS2 67/17	27-Jul-12	ETM+7	WRS2 67/17	30-Jul-13	ETM+7

Table 3.4 Landsat images used to produce velocity fields for the Wrangell Mountains.

Path/Row	Date 1	Sensor	Path/Row	Date 2	Sensor
WRS1 71/16	24-Sep-72	MSS 1	WRS1 71/16	19-Sep-73	MSS 1
WRS1 71/16	19-Sep-73	MSS 1	WRS1 71/17	4-Jul-74	MSS 1
WRS1 71/17	4-Jul-74	MSS 1	WRS1 71/16	8-Jul-75	MSS2
WRS1 71/16	8-Jul-75	MSS 2	WRS1 71/16	25-Aug-76	MSS 2
WRS1 71/16	25-Aug-76	MSS 2	WRS1 71/16	20-Aug-77	MSS 2
WRS1 71/16	20-Aug-77	MSS 2	WRS1 71/16	10-Jul-78	MSS 2
WRS1 71/16	10-Jul-78	MSS 2	WRS1 71/16	19-Aug-79	MSS 3
WRS1 71/16	15-May-80	MSS 3	WRS1 71/16	1-May-81	MSS 2
WRS1 71/16	17-Aug-81	MSS 2	WRS2 65/17	12-Aug-82	MSS 4
WRS2 65/17	12-Aug-82	MSS 4	WRS2 65/17	16-Sep-83	MSS 4
WRS2 65/17	25-Apr-83	MSS 4	WRS2 65/17	5-May-84	MSS 5
WRS2 65/17	5-May-84	MSS 5	WRS2 65/17	22-Apr-85	MSS 5
WRS2 65/17	27-Jul-85	TM 5	WRS2 65/17	16-Sep-86	TM 5
WRS2 65/17	16-Sep-86	TM 5	WRS2 65/17	2-Aug-87	TM 5
WRS2 65/17	2-Aug-87	TM 5	WRS2 65/17	12-Aug-88	TM 4
WRS2 65/17	7-Jul-95	TM 5	WRS2 65/17	23-Jun-96	TM 5
WRS2 65/17	23-Jun-96	TM 5	WRS2 65/17	29-Aug-97	TM 5
WRS2 65/17	29-Aug-97	TM 5	WRS2 65/17	29-Jun-98	TM 5
WRS2 65/17	29-Jun-98	TM 5	WRS2 65/17	2-Jul-99	TM 5
WRS2 65/17	29-Apr-99	TM 5	WRS2 65/17	9-May-00	TM 5
WRS2 65/17	9-May-00	TM 5	WRS2 65/17	12-May-01	ETM+7
WRS2 65/17	15-Jul-01	ETM+7	WRS2 65/17	3-Aug-02	ETM+7
WRS2 65/17	3-Aug-02	ETM+7	WRS2 65/17	6-Aug-03	ETM+7
WRS2 65/17	6-Aug-03	ETM+7	WRS2 65/17	16-Aug-04	TM 5
WRS2 65/17	16-Aug-04	TM 5	WRS2 65/17	11-Aug-05	ETM+7
WRS2 65/17	11-Aug-05	ETM+7	WRS2 65/17	13-Jul-06	ETM+7
WRS2 65/17	8-Apr-06	ETM+7	WRS2 65/17	26-Mar-07	ETM+7
WRS2 65/17	17-Aug-07	ETM+7	WRS2 65/17	11-Aug-08	TM 5
WRS2 65/17	11-Aug-08	TM 5	WRS2 65/17	29-Jul-09	TM 5
WRS2 65/17	29-Jul-09	TM 5	WRS2 65/17	18-Sep-10	TM 5
WRS2 65/17	21-May-10	ETM+7	WRS2 65/17	24-May-11	ETM+7
WRS2 65/17	12-Aug-11	ETM+7	WRS2 65/17	14-Aug-12	ETM+7
WRS2 65/17	8-Apr-12	ETM+7	WRS2 65/17	21-May-13	OLI 8

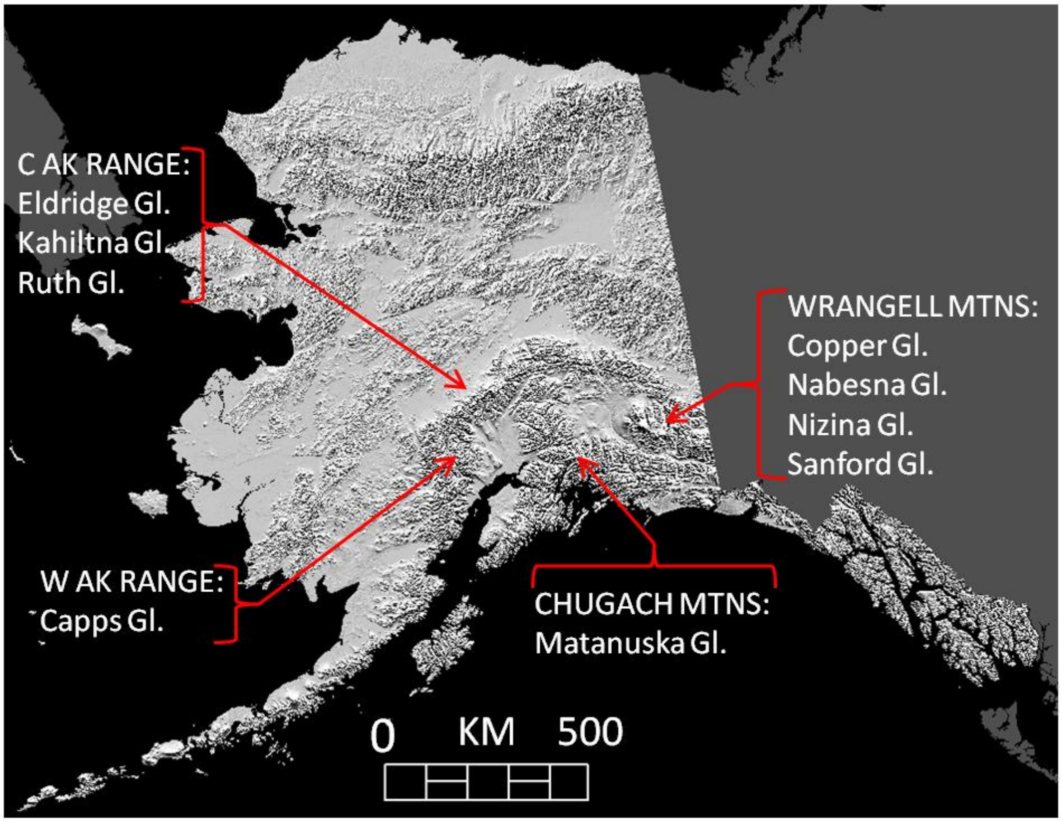

Figure 3.1. Location of pulsing glaciers in this study and the mountain ranges of southern Alaska that contain them.

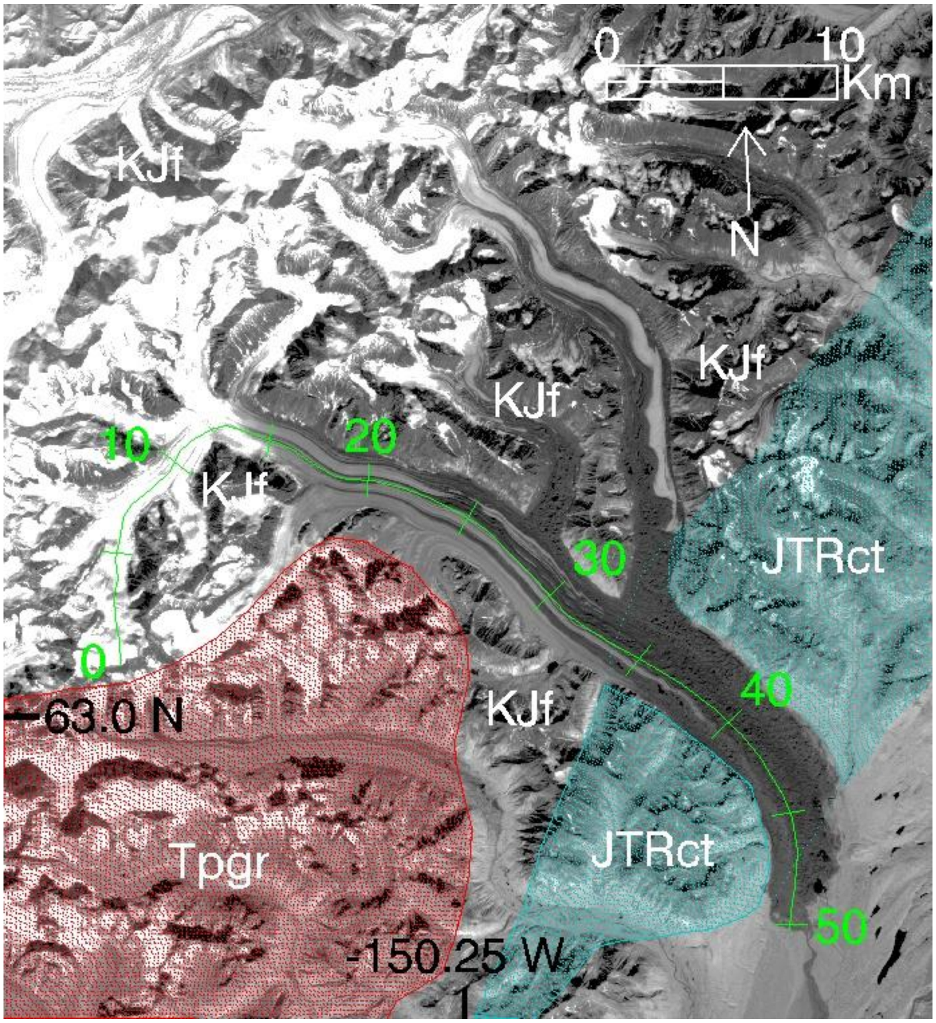

Figure 3.2. Eldridge Glacier. Transect along glacier centerline (shown in green) indicates the location of the velocity profiles shown in Figure 3.11, units are km. Areas highlighted in aqua and labeled JTRct indicate the location of bedrock composed primarily of crystalline tuff. Areas highlighted in red and labeled Tpgr indicate the location of bedrock composed of granite. Areas labeled KJf are underlain by sedimentary bedrock (Data source: Wilson et al., 1998).

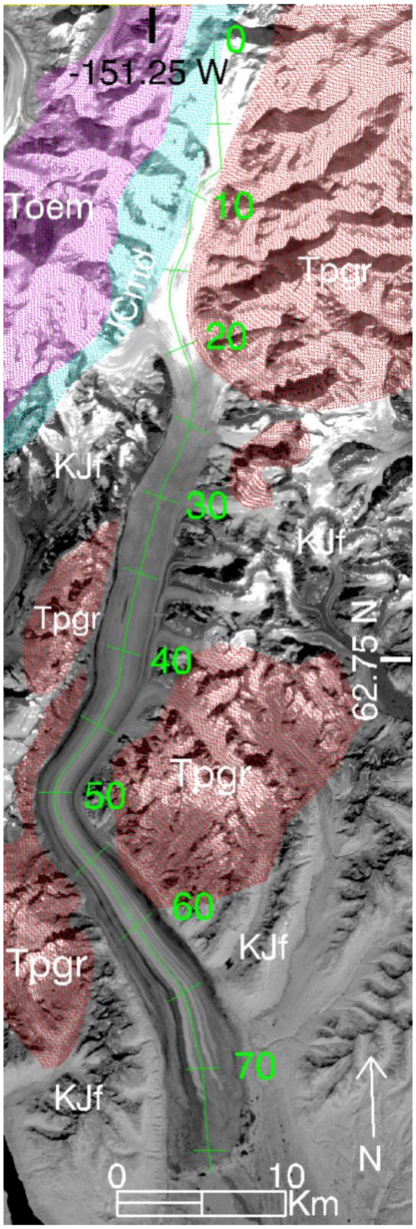

Figure 3.3. Kahiltna Glacier. Transect along glacier centerline (shown in green) indicates the location of the velocity profiles shown in Figure 3.14, units are km. Areas highlighted in red (Tpgr) and magenta (Toem) indicate areas underlain by crystalline bedrock composed of granite or granodiorite, respectively. Areas highlighted in aqua (JCmd) or labeled KJf indicate areas underlain by sedimentary bedrock (Data source: Wilson et al., 1998).

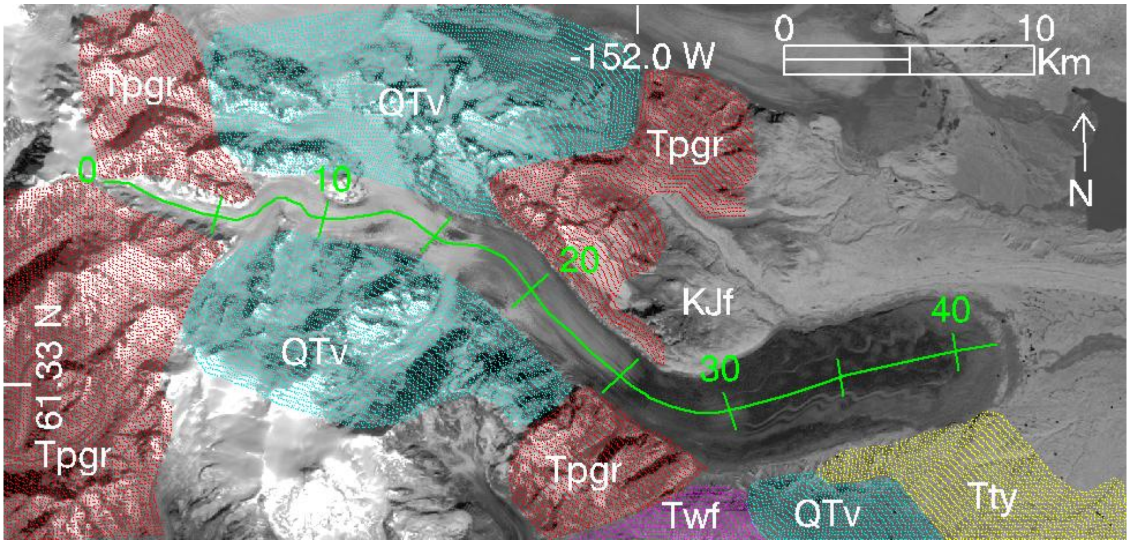

Figure 3.4. Capps Glacier. Transect along glacier centerline (shown in green) indicates the location of the velocity profiles shown in Figure 3.18, units are km. Areas highlighted in red or aqua indicate areas underlain by crystalline bedrock composed of granite (Tpgr) or basalt (QTv), respectively. Areas highlighted in magenta (Twf) or yellow (Tty), or labeled KJf, indicate areas underlain by sedimentary bedrock (Data source: Wilson et al., 1998).

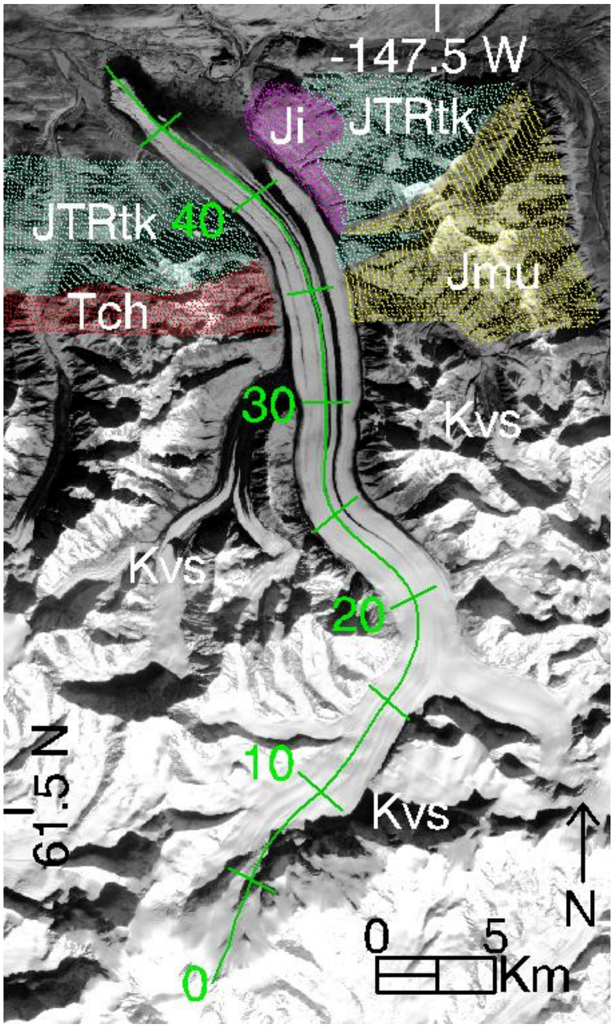

Figure 3.5. Matanuska Glacier. Transect along glacier centerline (shown in green) indicates the location of the velocity profiles shown in Figure 3.21, units are km. Areas highlighted in magenta (Ji) or yellow (Jmu) indicate areas underlain by crystalline bedrock composed of granite or various igneous ultramafic rocks, respectively. Areas highlighted in aqua (JTRtk) or red (Tch), or labeled Kvs, indicate areas underlain by sedimentary bedrock (Data source: Wilson et al., 1998).

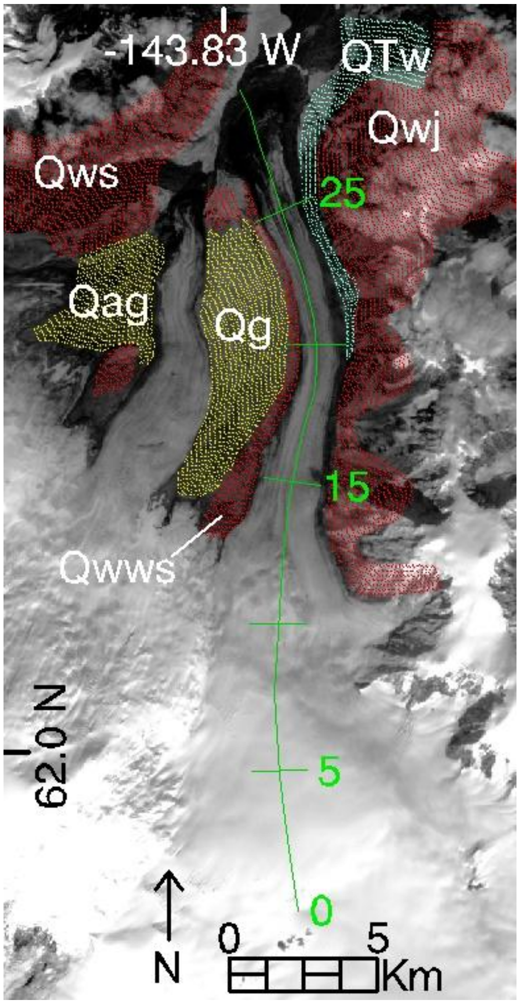

Figure 3.6. Copper Glacier. Transect along glacier centerline (shown in green) indicates the location of the velocity profiles shown in Figure 3.24, units are km. Areas highlighted in aqua (QTw) or red (Qwj, Qwws) indicate areas underlain by crystalline bedrock composed of andesitic lava flows. Areas highlighted in yellow (Qag, Qg) indicate areas underlain by unlithified sediments of Holocene or Pleistocene age, respectively (Data source: Richter et al., 2006).

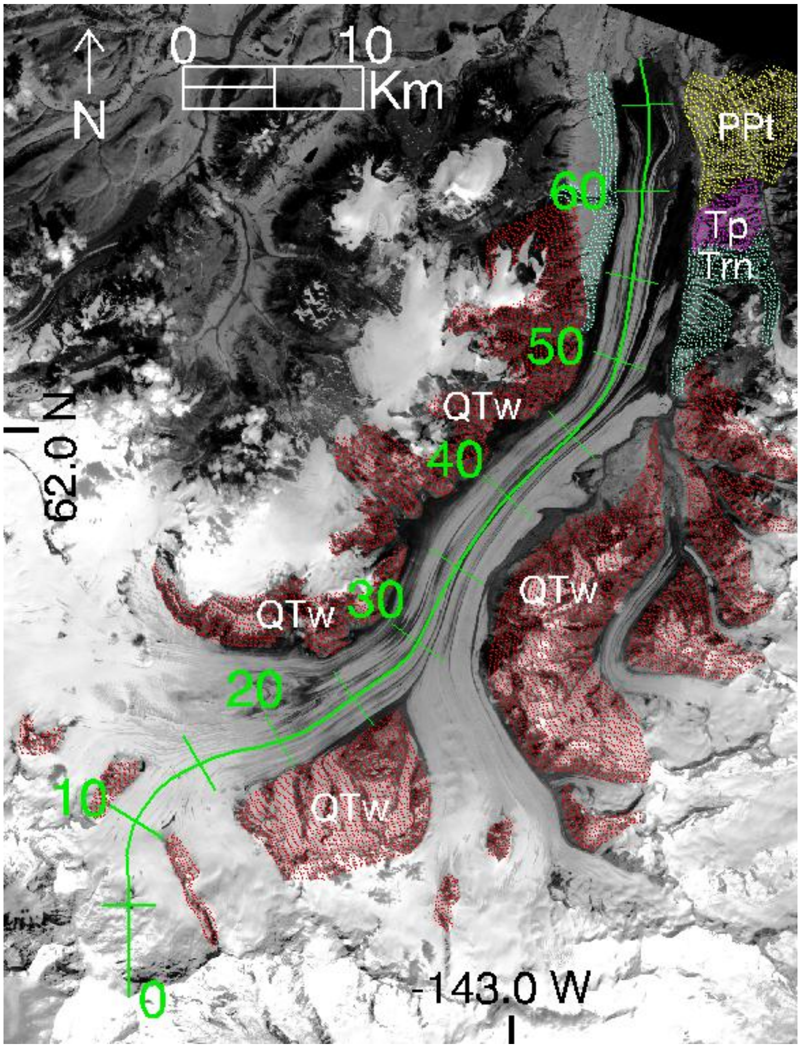

Figure 3.7. Nabesna Glacier. Transect along glacier centerline (shown in green) indicates the location of the velocity profiles shown in Figure 3.27, units are km. Areas highlighted in red (QTw), aqua (Trn), or yellow (PPt) indicate areas underlain by crystalline bedrock composed of lava. Areas highlighted by magenta (Tp) indicate areas underlain by granitic bedrock (Data source: Richter et al., 2006).

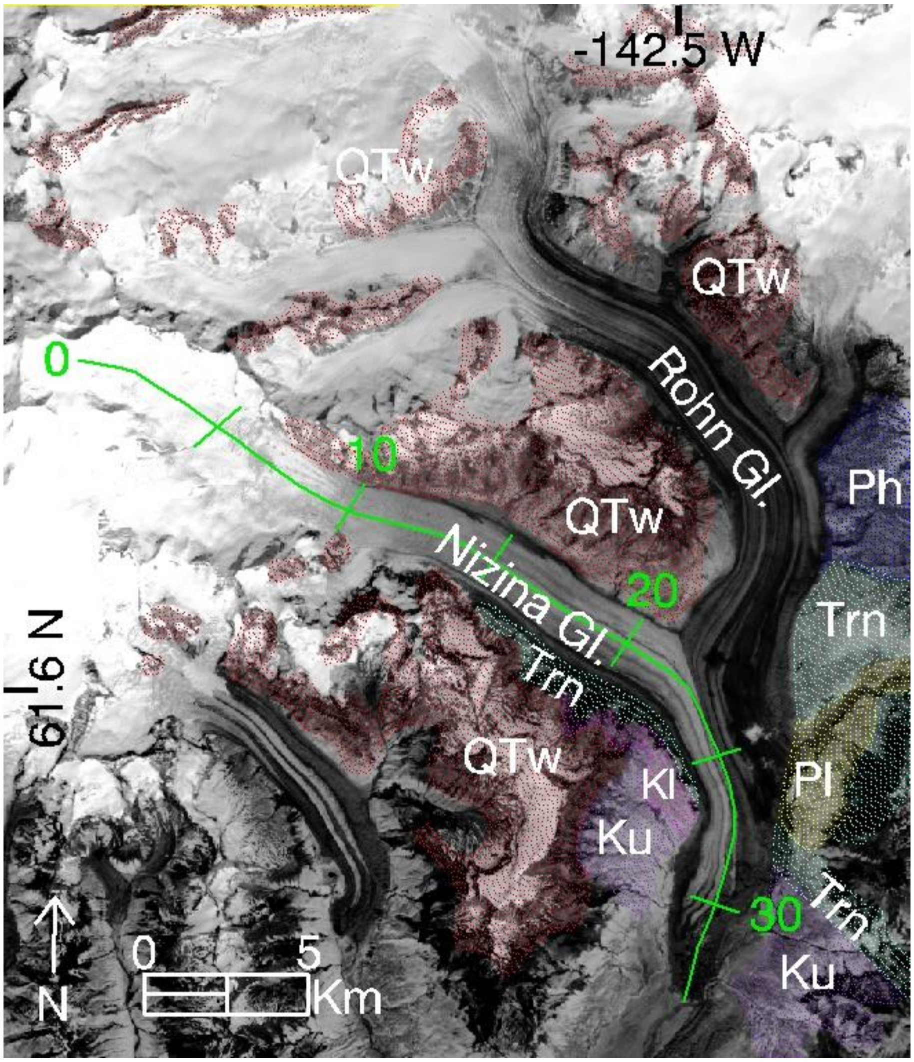

Figure 3.8. Nizina Glacier. Transect along glacier centerline (shown in green) indicates the location of the velocity profiles shown in Figure 3.30, units are km. Areas highligted in red (QTw) or aqua (Trn) indicate areas underlain by crystalline bedrock composed of lava. Areas highlighted in magenta (Kl), purple (Ku), yellow (Pl), or blue (Ph) indicate areas underlain by sedimentary bedrock (Data source: Richter et al., 2006).

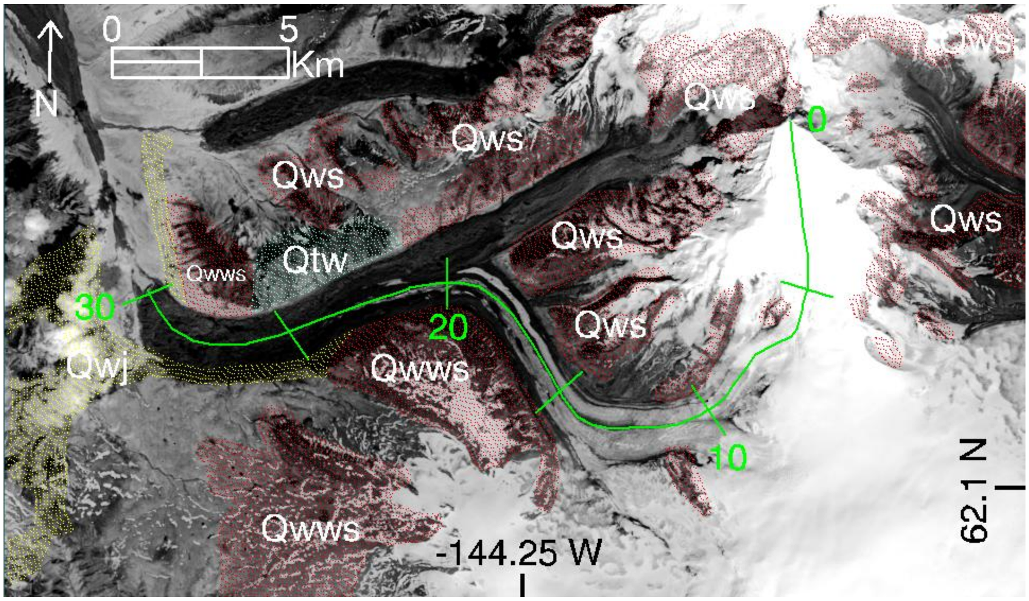

Figure 3.9. Sanford Glacier. Transect along glacier centerline (shown in green) indicates the location of the velocity profiles shown in Figure 3.33, units are km. Areas highlighted in red (Qws, Qwws), aqua (Qtw), or yellow (Qwj) indicate areas underlain by crystalline bedrock composed of lava (Data source: Richter et al., 2006).

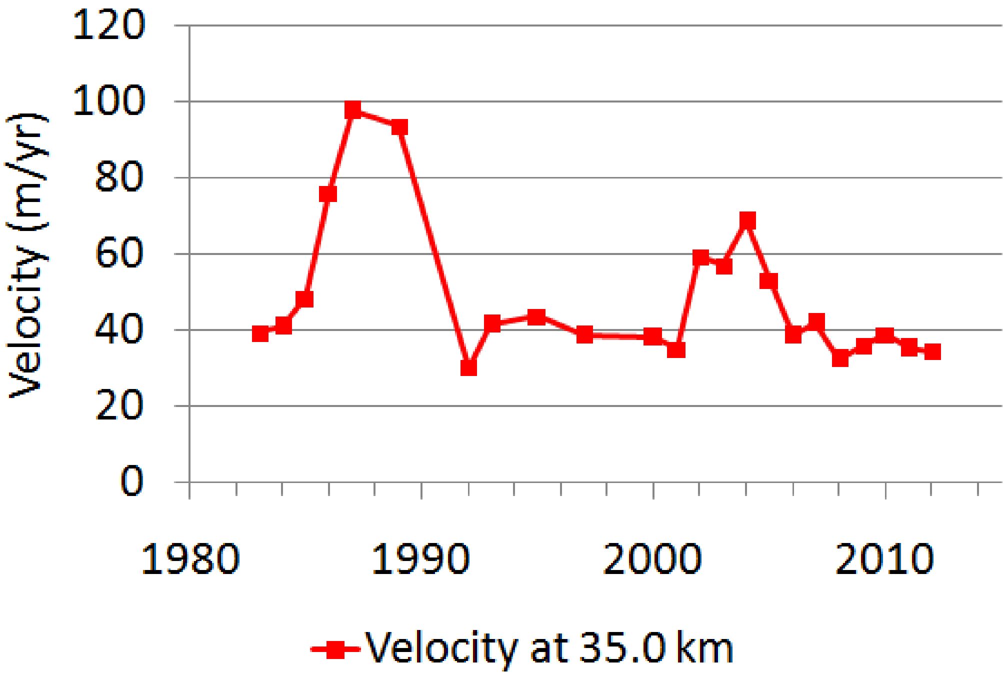

Figure 3.10. Velocity of Eldridge Glacier through time, at the 35 km mark. Two pulses are seen; the first pulse peaked in 1987 at 97.8 m/yr, and the second pulse peaked in 2004 at 68.8 m/yr.

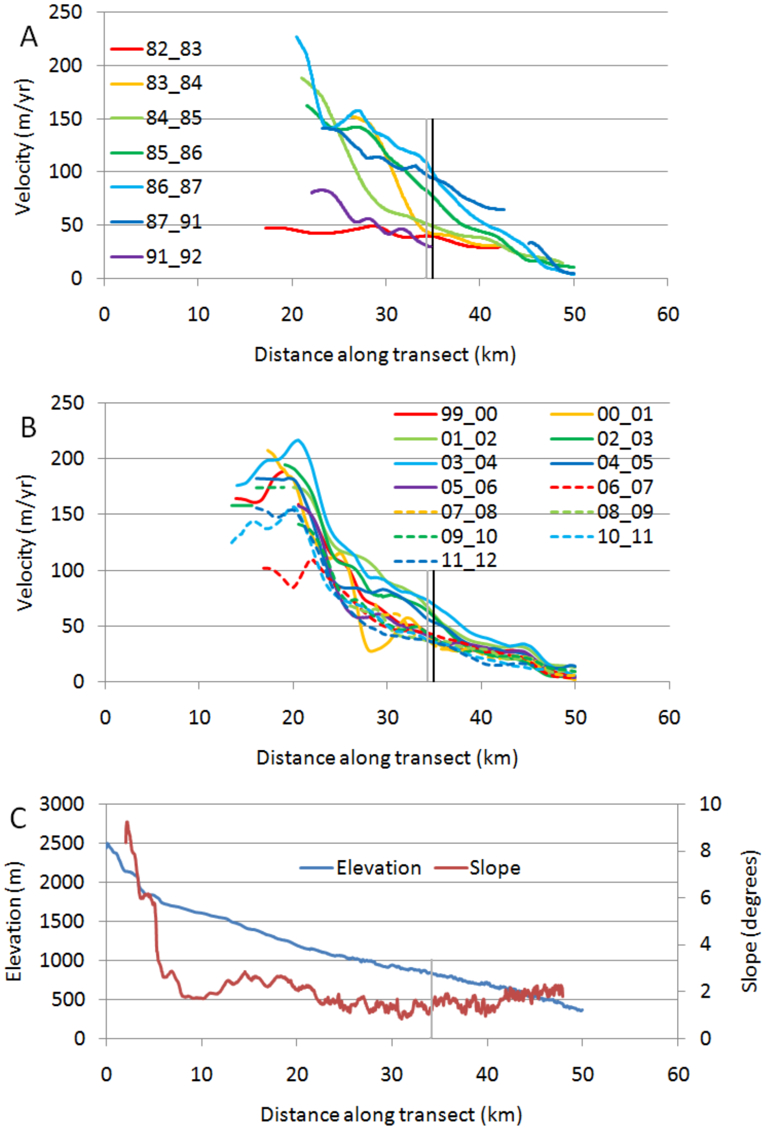

Figure 3.11. Centerline profiles for Eldridge Glacier. A) Velocity from 1982–1983 to 1991–1992 showing the first pulse. B) Velocity from 1999–2000 to 2011–2012 showing the second pulse. C). Elevation and slope of the glacier surface. Vertical black line at the 35 km mark in panels A and B indicates position at which velocity values were taken to create time-series in Figure 3.10. Vertical gray line at the 34 km mark indicates location of change in bedrock lithology discussed in Section 3.5.1.

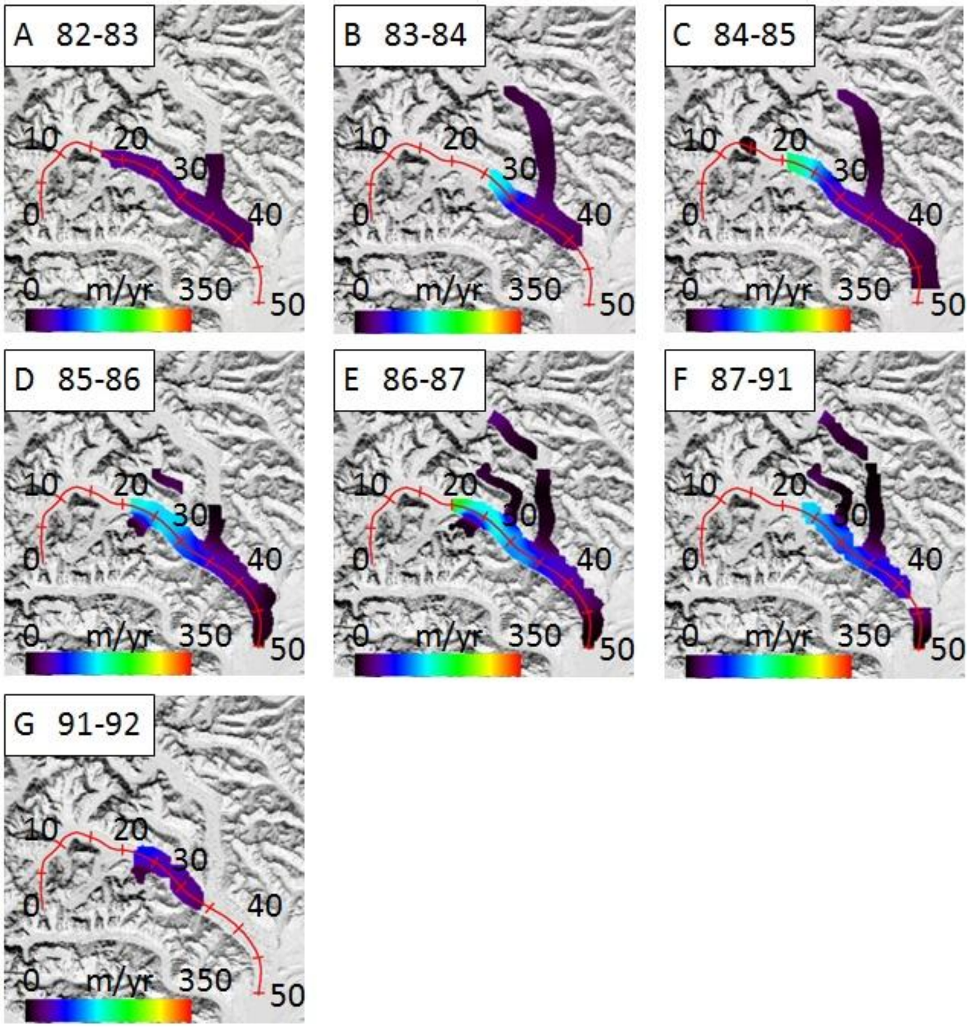

Figure 3.12. Velocity fields for Eldridge Glacier encompassing the first pulse from 1982–1983 to 1991–1992. A) 1982–1983 velocity. B) 1983–1984 velocity. C) 1984–1985 velocity. D) 1985–1986 velocity. E) 1986–1987 velocity. F) 1987–1991 velocity. G) 1991–1992 velocity. Velocity fields for the second pulse of Eldridge Glacier are not shown. Locations on glacier that are not colored indicate areas where feature tracking program failed to produce reliable measurements.

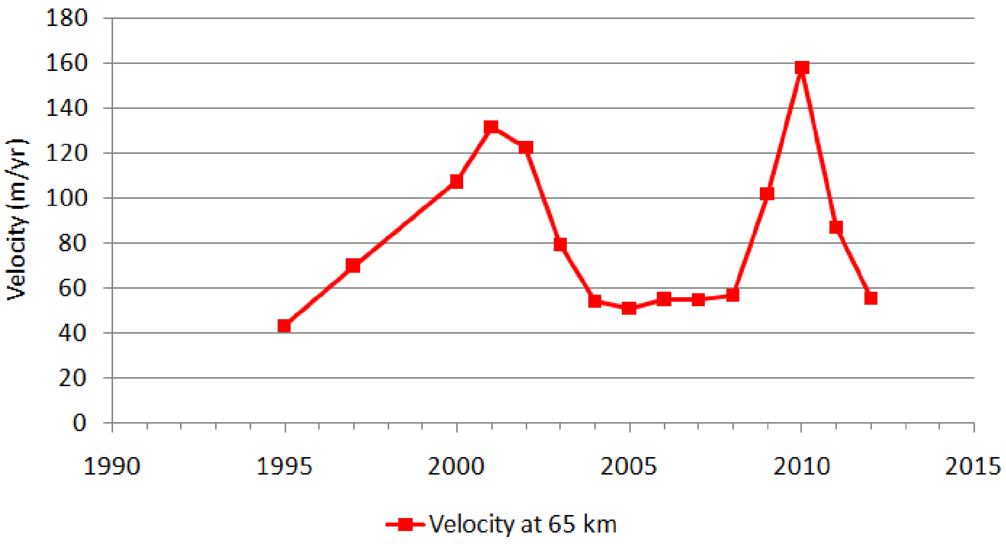

Figure 3.13. Velocity of Kahiltna Glacier through time, at the 65 km mark. Two pulses are seen; the first pulse peaked in 2001 at 131.4 m/yr, and the second pulse peaked in 2010 at 157.5 m/yr.

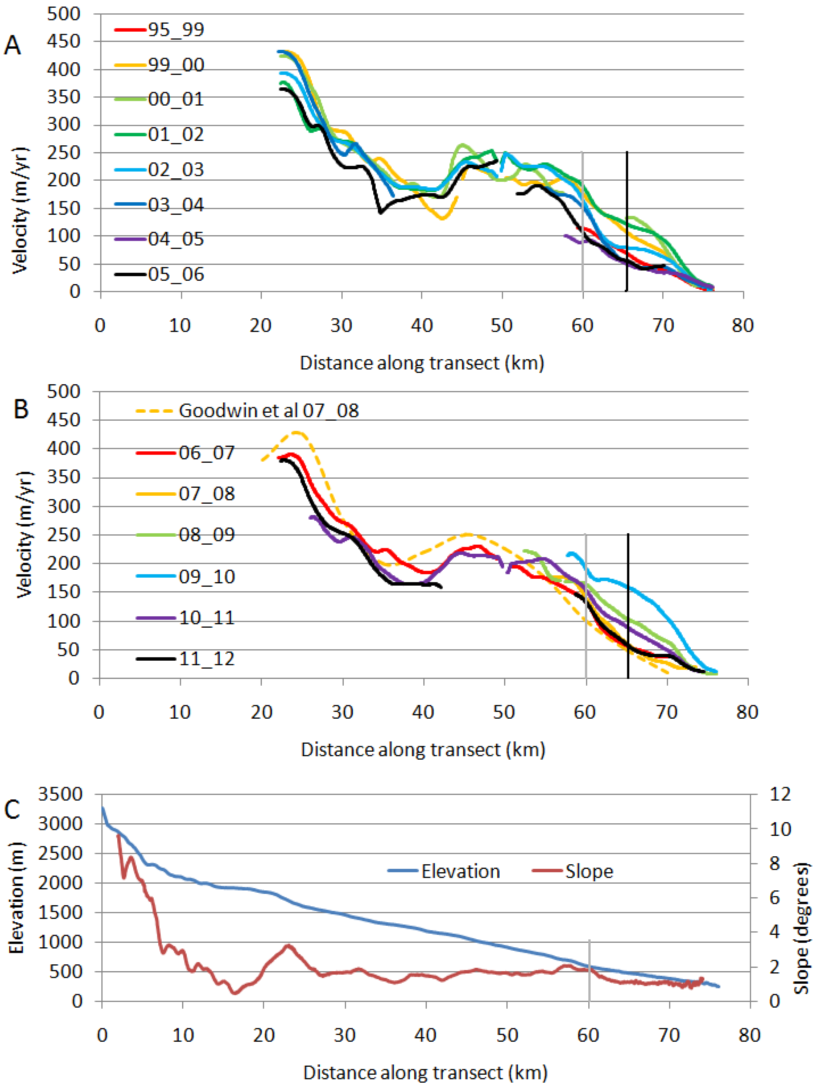

Figure 3.14. Centerline profiles for Kahiltna Glacier. A) Velocity from 1995–1999 to 2005–2006 showing the first pulse. B) Velocity from 2006–2007 to 2011–2012 showing the second pulse. Dashed orange profile represents velocity measurements in 2007-2008 by Goodwin et al. (2012). C). Elevation and slope of the glacier surface. Vertical black line at the 65 km mark in panels A and B indicates position at which velocity values were taken to create time-series in Figure 3.13. Vertical gray line at the 60 km mark indicates location of change in bedrock lithology discussed in Section 3.5.2.

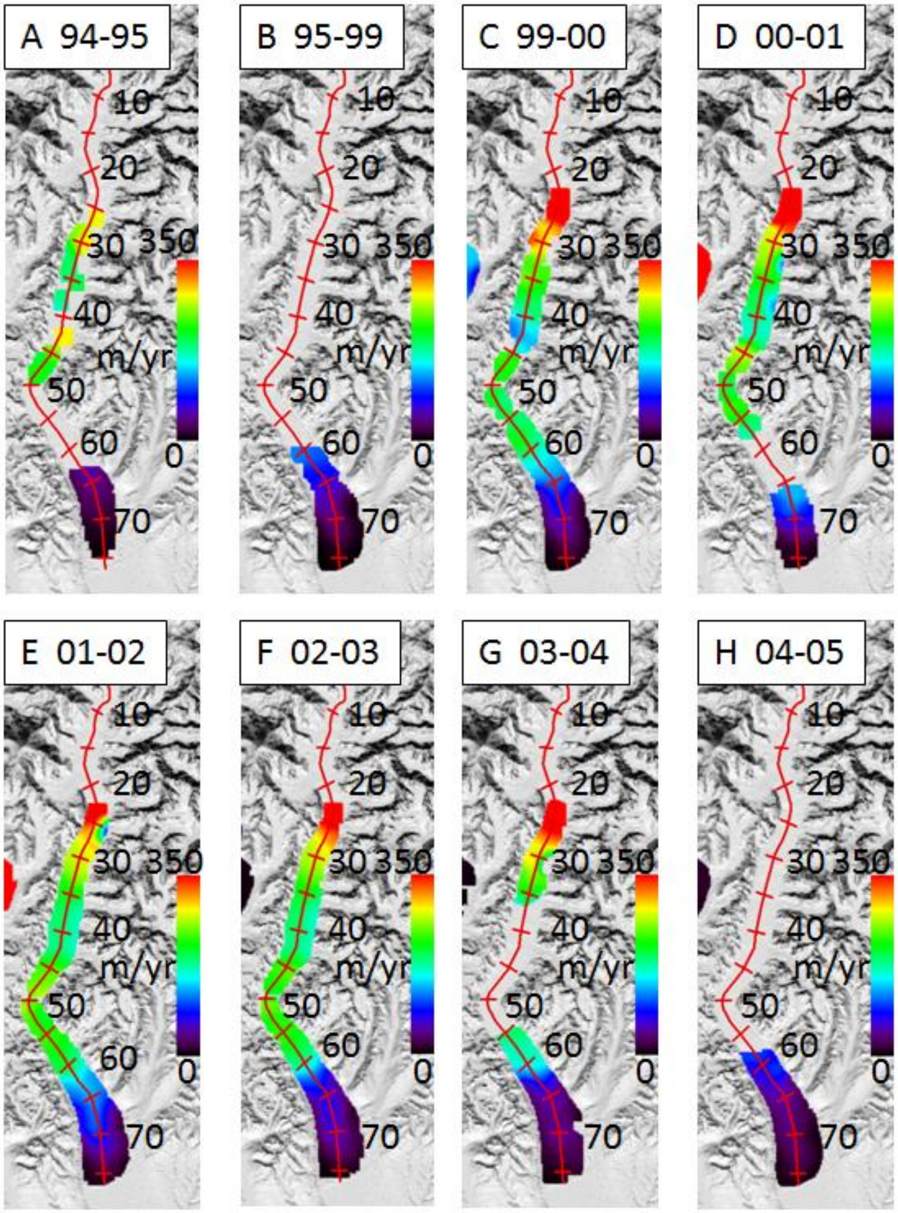

Figure 3.15. Velocity fields for Kahiltna Glacier encompassing the first pulse from 1994–1995 to 2004–2005. A) 1994–1995 velocity. B) 1995–1999 velocity. C) 1999–2000 velocity. D) 2000–2001 velocity. E) 2001–2002 velocity. F) 2002–2003 velocity. G) 2003–2004 velocity. H) 2004–2005 velocity. Velocity fields for the second pulse of Kahiltna Glacier are not shown.

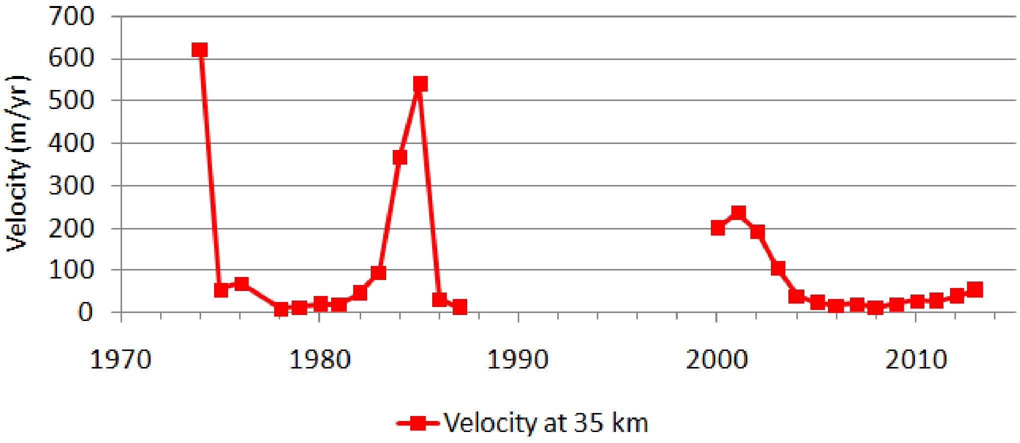

Figure 3.16. Velocity of Capps Glacier through time, at the 35 km mark. Three pulses are seen; the first pulse peaked in 1974 at 632.2 m/yr, the second pulse peaked in 1985 at 537.9 m/yr, and the third pulse peaked in 2001 at 237.2 m/yr.

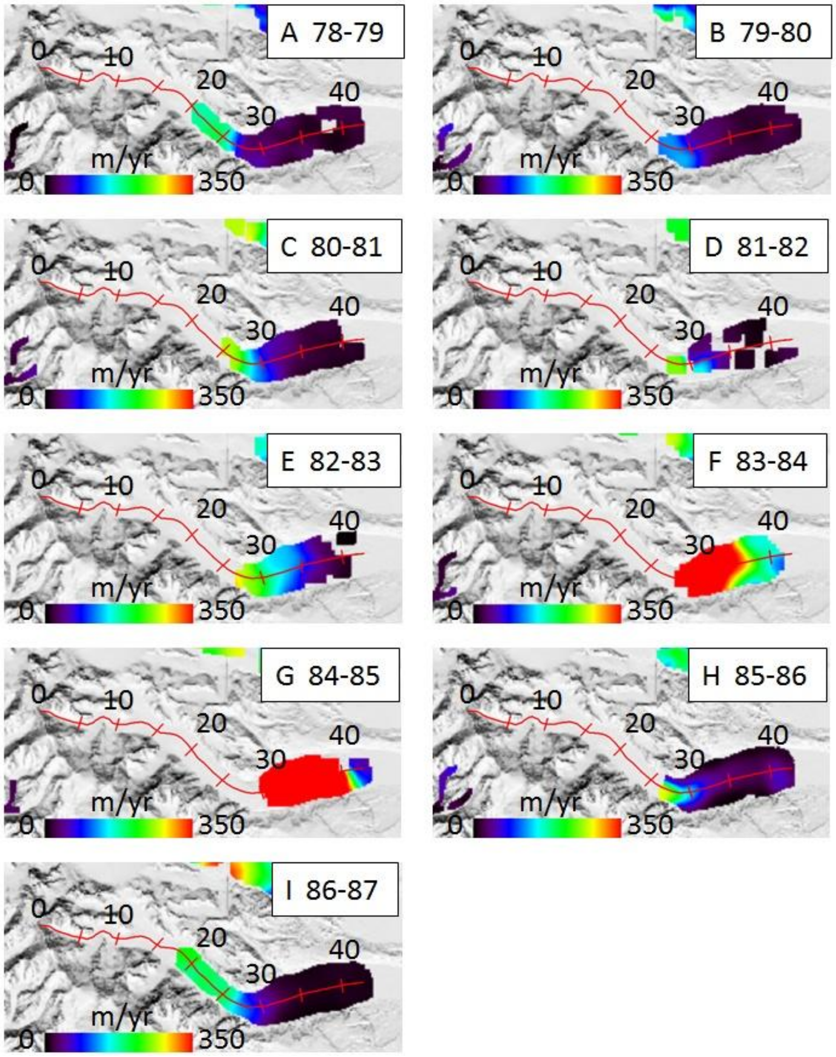

Figure 3.17. Velocity fields for Capps Glacier encompassing the second pulse from 1978–1979 to 1986–1987. A) 1978–1979 velocity. B) 1979–1980 velocity. C) 1980–1981 velocity. D) 1981–1982 velocity. E) 1982–1983 velocity. F) 1983–1984 velocity. G) 1984–1985 velocity. H) 1985–1986 velocity. I) 1986–1987 velocity. Velocity fields for the first and third pulses of Capps Glacier are not shown.

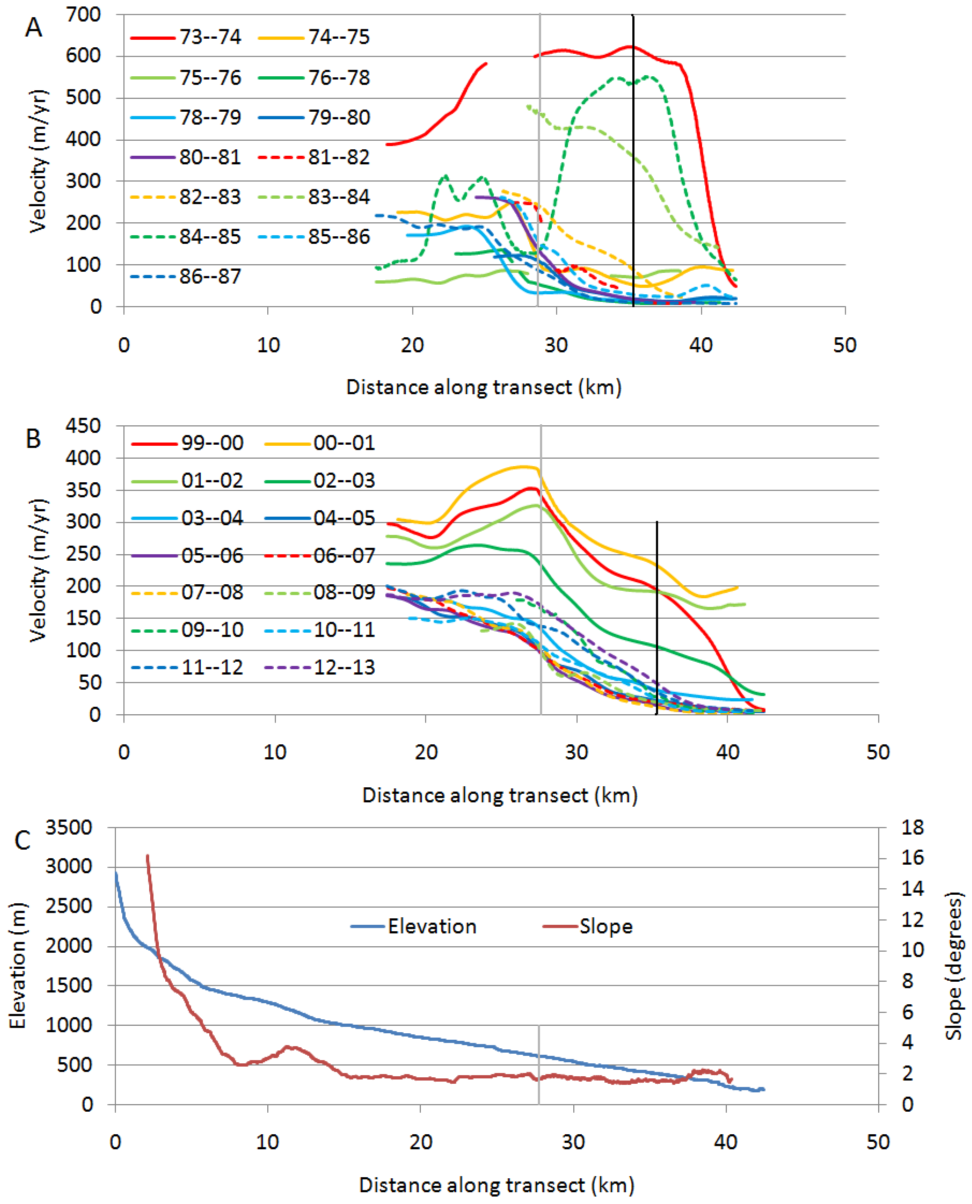

Figure 3.18. Centerline profiles for Capps Glacier. A) Velocity profiles from 1973–1974 to 1986-1987 showing the first and second pulses. B) Velocity profiles from 1999–2000 to 2012–2013 showing the third pulse. C) Elevation and slope of the glacier surface. Vertical black line at the 35 km mark in panels A and B indicates position at which velocity values were taken to create time-series in Figure 3.16. Vertical gray line at the 28 km mark indicates location of change in bedrock lithology discussed in Section 3.5.3.

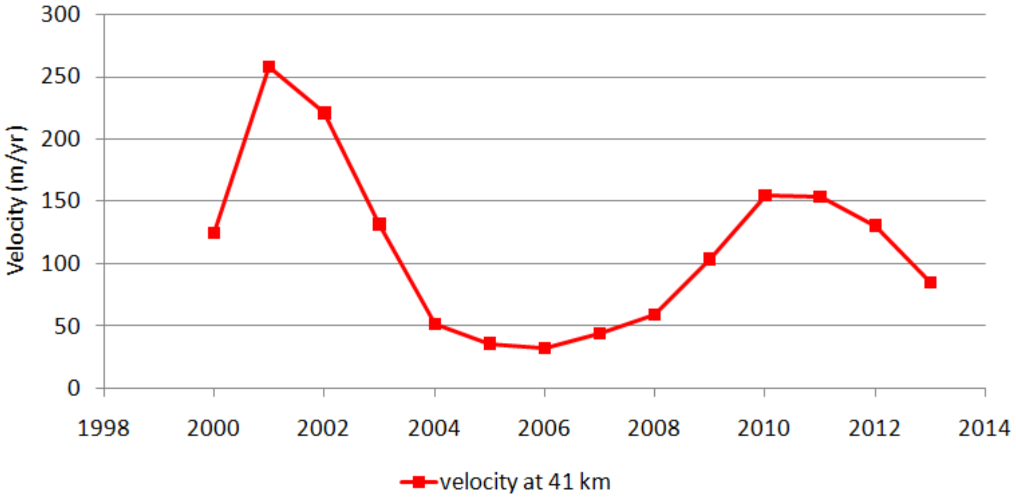

Figure 3.19. Velocity of Matanuska Glacier through time, at the 41 km mark. Two pulses are seen; the first pulse peaked in 2001 at 257.5 m/yr, and the second pulse peaked in 2010 at 154.5 m/yr.

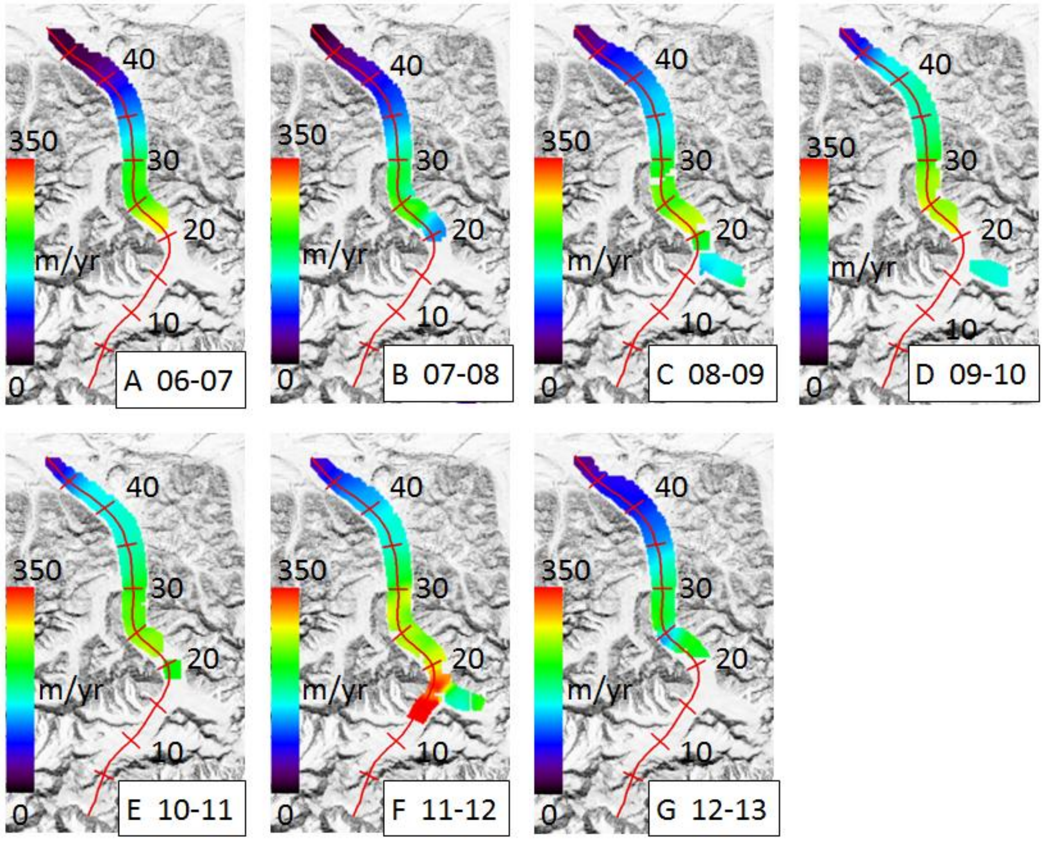

Figure 3.20. Velocity fields for Matanuska Glacier encompassing the second pulse from 2006–2007 to 2012–2013. A) 2006–2007 velocity. B) 2007–2008 velocity. C) 2008–2009 velocity. D) 2009–2010 velocity. E) 2010–2011 velocity. F) 2011–2012 velocity. G) 2012–2013 velocity. Velocity fields for the first pulse of Matanuska Glacier are not shown.

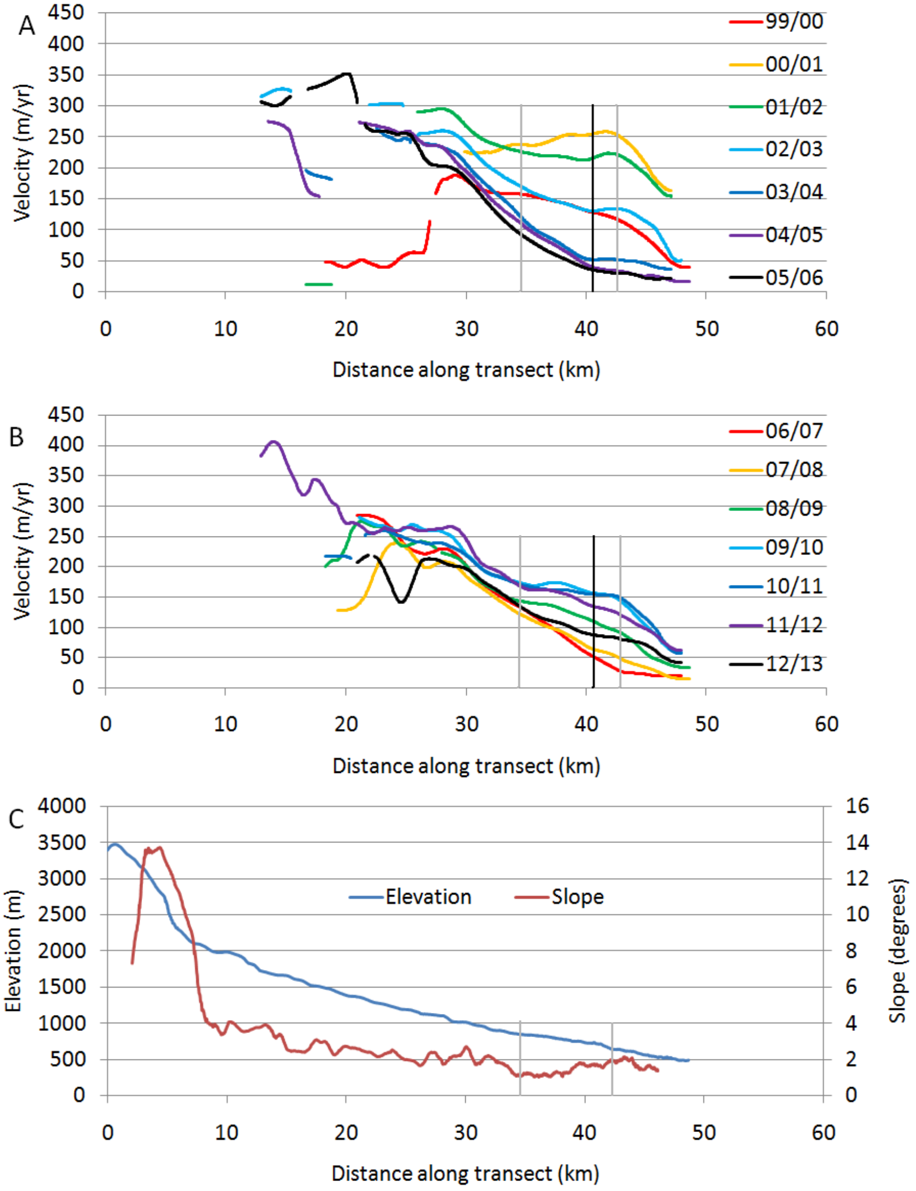

Figure 3.21. Centerline profiles for Matanuska Glacier. A) Velocity profiles from 1999–2000 to 2005–2006 showing the first pulse. B) Velocity profiles from 2006–2007 to 2012–2013 showing the second pulse. C). Elevation and slope of the glacier surface. Vertical black line at the 41 km mark in panels A and B indicates position at which velocity values were taken to create time-series in Figure 3.19. Vertical gray lines at the 34 and 43 km marks indicate locations of change in bedrock lithology discussed in Section 3.5.4.

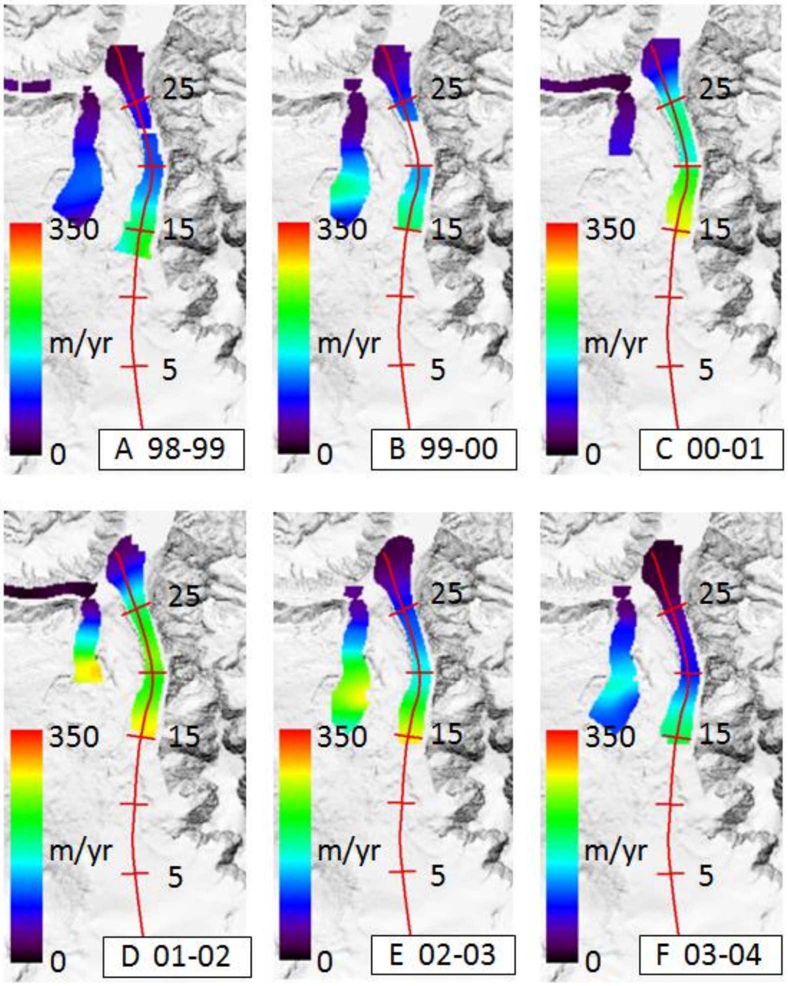

Figure 3.22. Velocity fields for Copper Glacier encompassing its pulse from 1998–1999 to 2003–2004. A) 1998–1999 velocity. B) 1999–2000 velocity. C) 2000–2001 velocity. D) 2001–2002 velocity. E) 2002–2003 velocity. F) 2003–2004 velocity. Velocity fields from 2004–2005 to 2012–2013 are not shown.

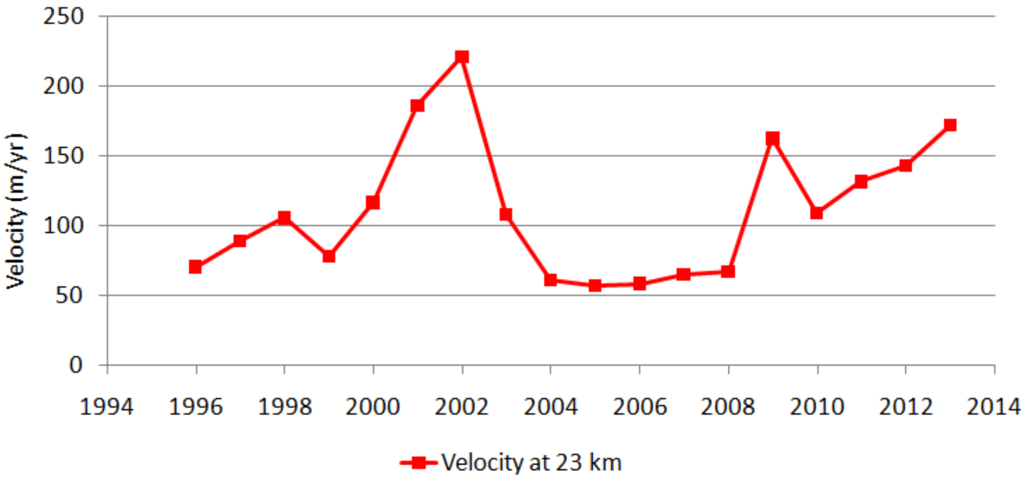

Figure 3.23. Velocity of Copper Glacier through time, at the 23 km mark. One complete pulse cycle is seen, with a peak in 2002 of 220.2 m/yr, and the acceleration phase of a second pulse is seen, with its current peak in 2013 of 172.0 m/yr.

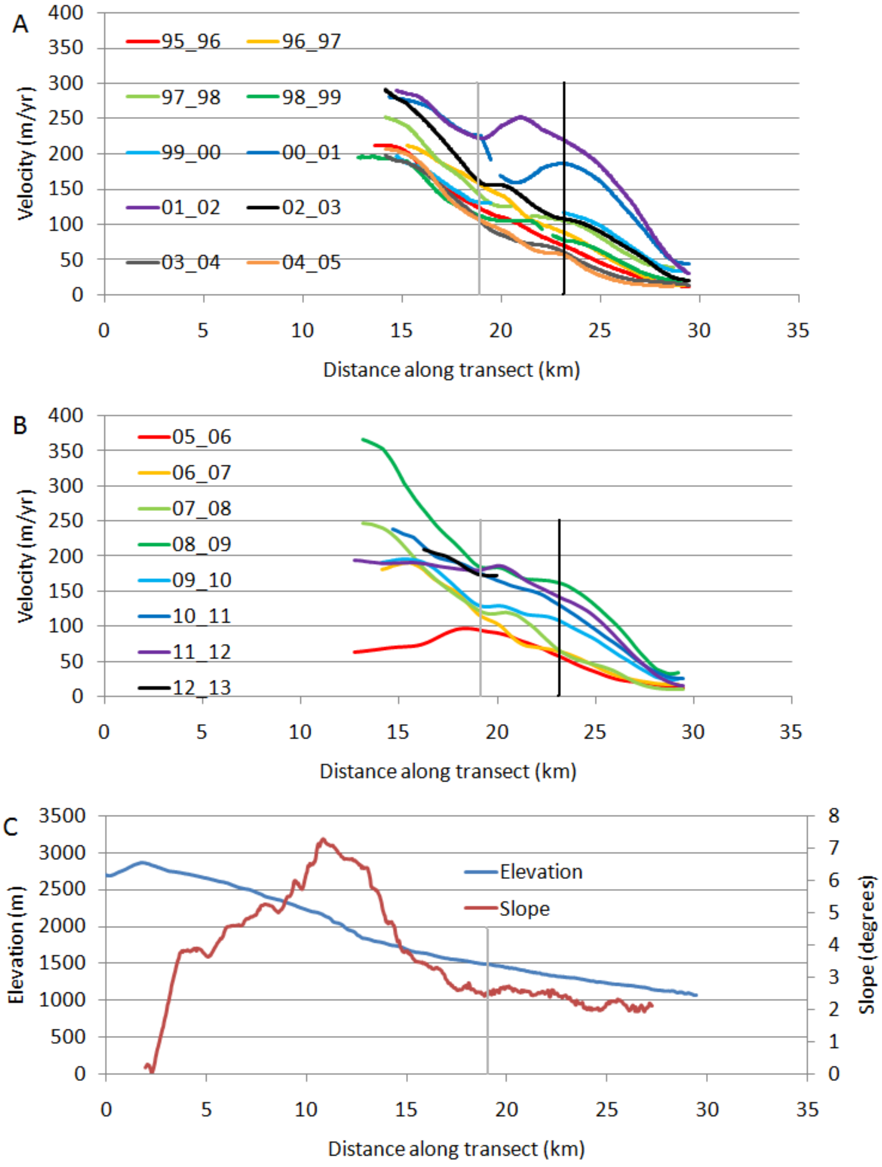

Figure 3.24. Centerline profiles for Copper Glacier. A) Velocity profiles from 1995–1996 to 2004–2005 showing the first pulse. B) Velocity profiles from 2005–2006 to 2012–2013 showing the acceleration phase of the second pulse. C). Elevation and slope of the glacier surface. Vertical black line at the 23 km mark in panels A and B indicates position at which velocity values were taken to create time-series in Figure 3.23. Vertical gray line at the 19 km mark indicates location of change in bedrock lithology discussed in Section 3.5.5.

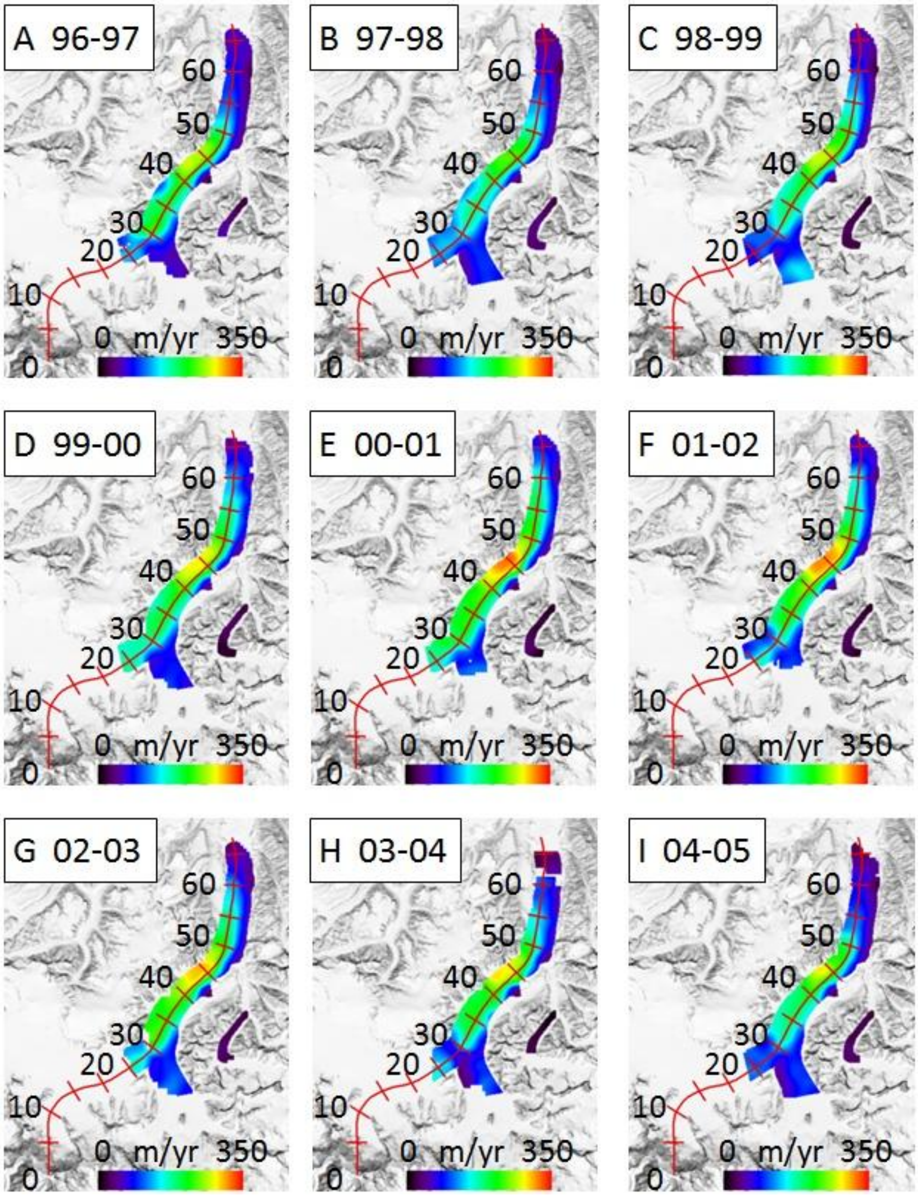

Figure 3.25. Velocity fields for Nabesna Glacier encompassing its pulse from 1996–1997 to 2004–2005. A) 1996–1997 velocity. B) 1997–1998 velocity. C) 1998–1999 velocity. D) 1999–2000 velocity. E) 2000–2001 velocity. F) 2001–2002 velocity. G) 2002–2003 velocity. H) 2003–2004 velocity. I) 2004–2005 velocity. Velocity fields from 2005–2006 to 2012–2013 are not shown.

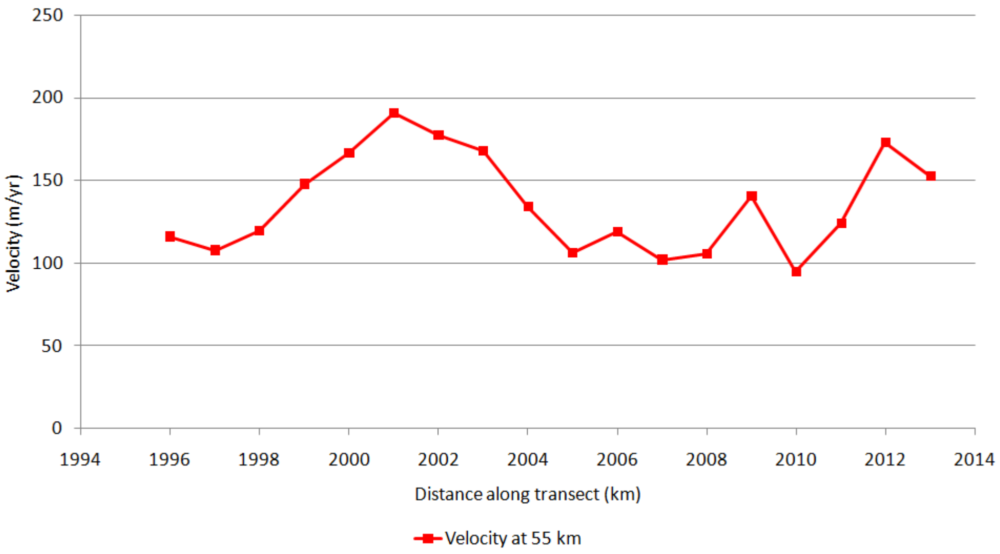

Figure 3.26. Velocity of Nabesna Glacier through time, at the 55 km mark. One complete pulse cycle is seen, with a peak in 2001 of 190.6 m/yr.

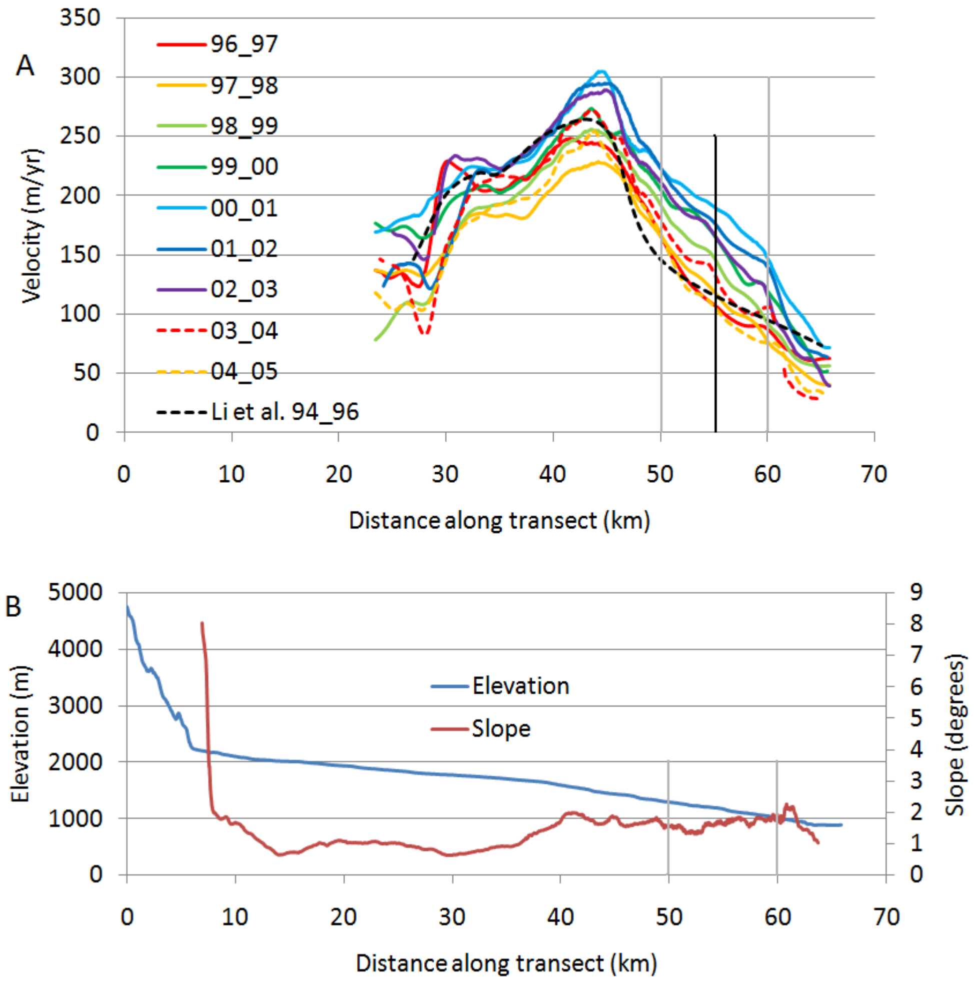

Figure 3.27. Centerline profiles for Nabesna Glacier. A) Velocity profiles from 1996–1997 to 2004–2005 showing the pulse. Dashed black profile represents a composite of velocity measurements by Li et al. (2008) spanning January, 1994 to May, 1996. B). Elevation and slope of the glacier surface. Vertical black line at the 55 km mark in panel A indicates position at which velocity values were taken to create time-series in Figure 3.26. Vertical gray lines at the 50 and 60 km marks indicate locations of change in bedrock lithology discussed in Section 3.5.6.

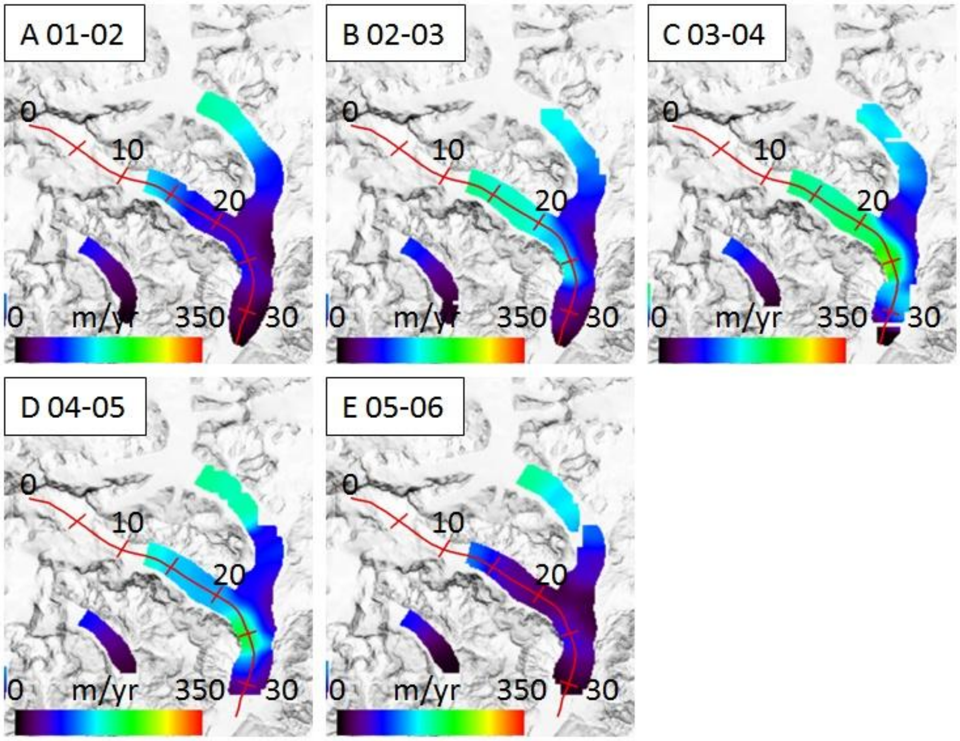

Figure 3.28. Velocity fields for Nizina Glacier encompassing its pulse from 2001–2002 to 2005–2006. A) 2001–2002 velocity. B) 2002–2003 velocity. C) 2003–2004 velocity. D) 2004–2005 velocity. E) 2005–2006 velocity. Velocity fields from 2006–2007 to 2012–2013 are not shown.

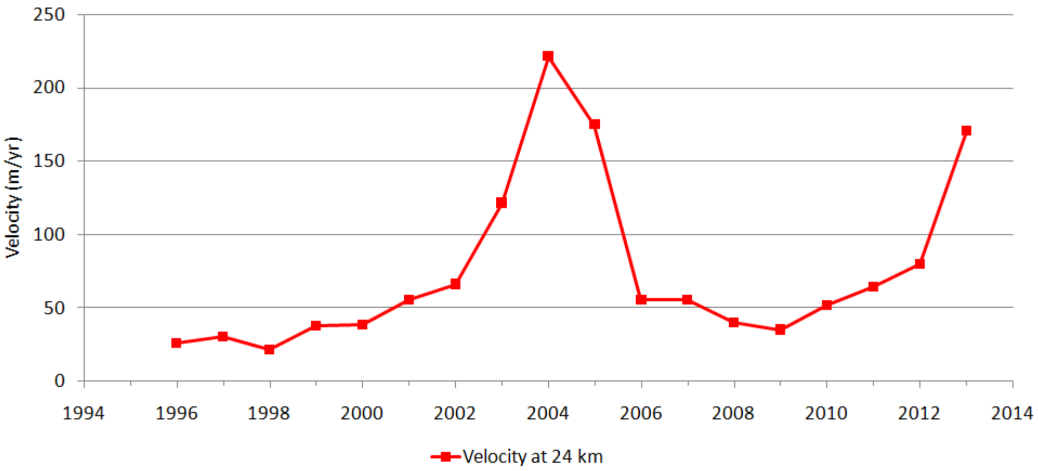

Figure 3.29. Velocity of Nizina Glacier through time, at the 24 km mark. One complete pulse cycle is seen, with a peak in 2004 of 221.1 m/yr, and the acceleration phase of a second pulse is seen, with its current peak in 2013 of 170.3 m/yr.

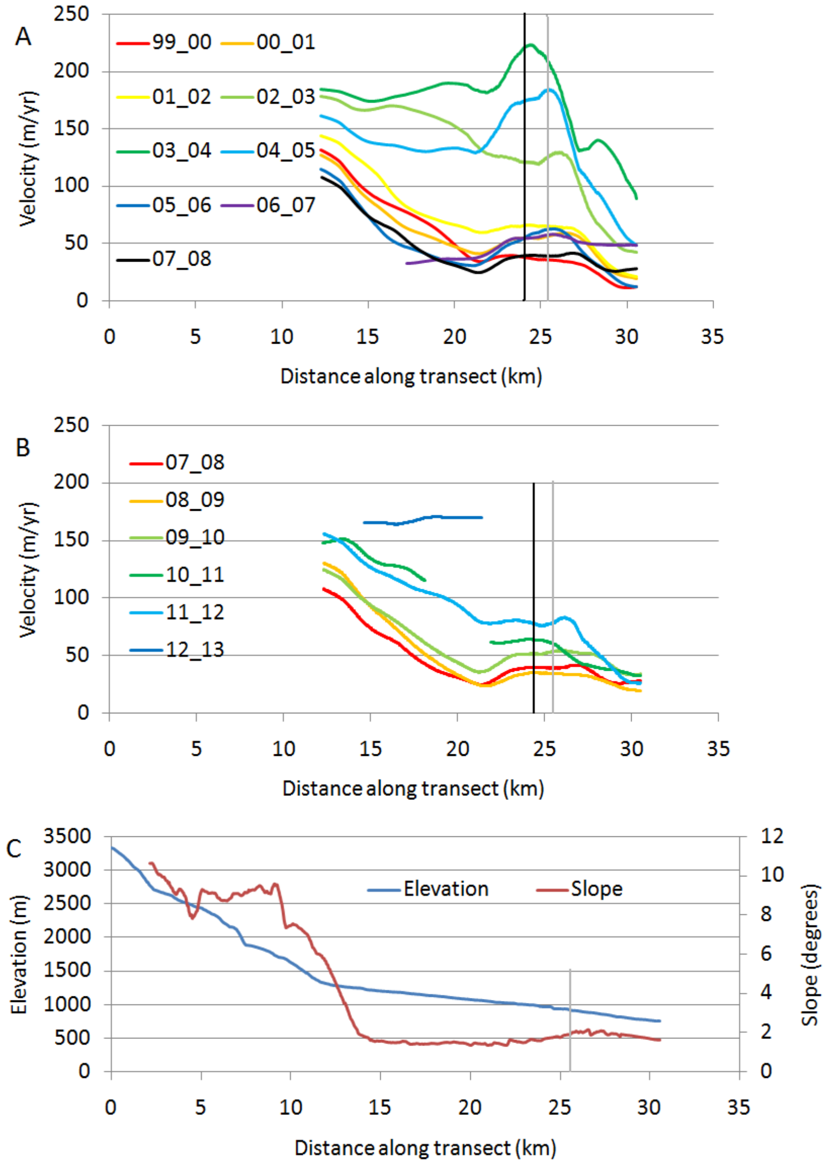

Figure 3.30. Centerline profiles for Nizina Glacier. A) Velocity profiles from 1999–2000 to 2007–2008 showing the first pulse. B) Velocity profiles from 2007–2008 to 2012–2013 showing the acceleration phase of the second pulse. C). Elevation and slope of the glacier surface. Vertical black line at the 24 km mark in panels A and B indicates position at which velocity values were taken to create time-series in Figure 3.29. Vertical gray line at the 26 km mark indicates location of change in bedrock lithology discussed in Section 3.5.7.

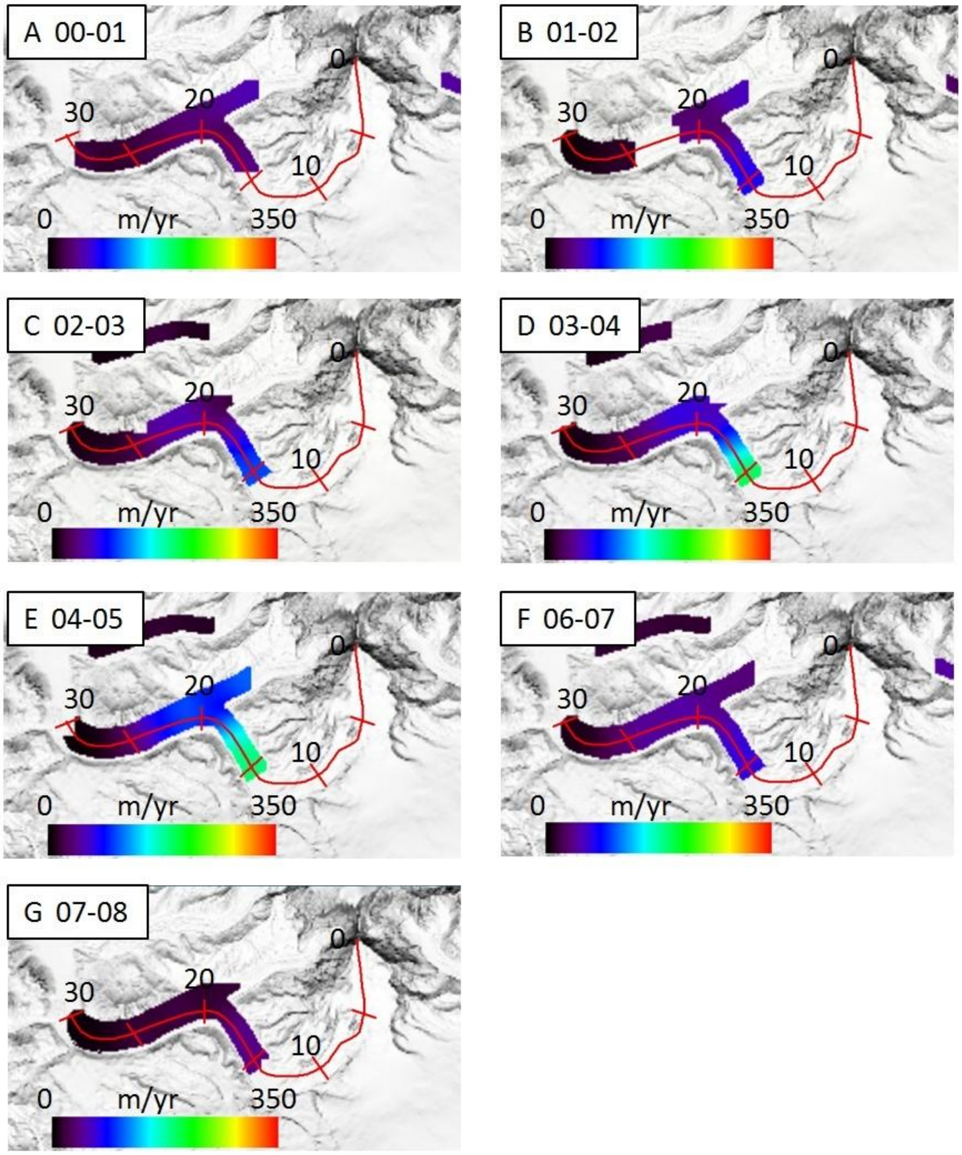

Figure 3.31. Velocity fields for Sanford Glacier encompassing its pulse from 2000–2001 to 2007–2008. A) 2000–2001 velocity. B) 2001–2002 velocity. C) 2002–2003 velocity. D) 2003–2004 velocity. E) 2004–2005 velocity. F) 2006–2007 velocity. G) 2007–2008 velocity.

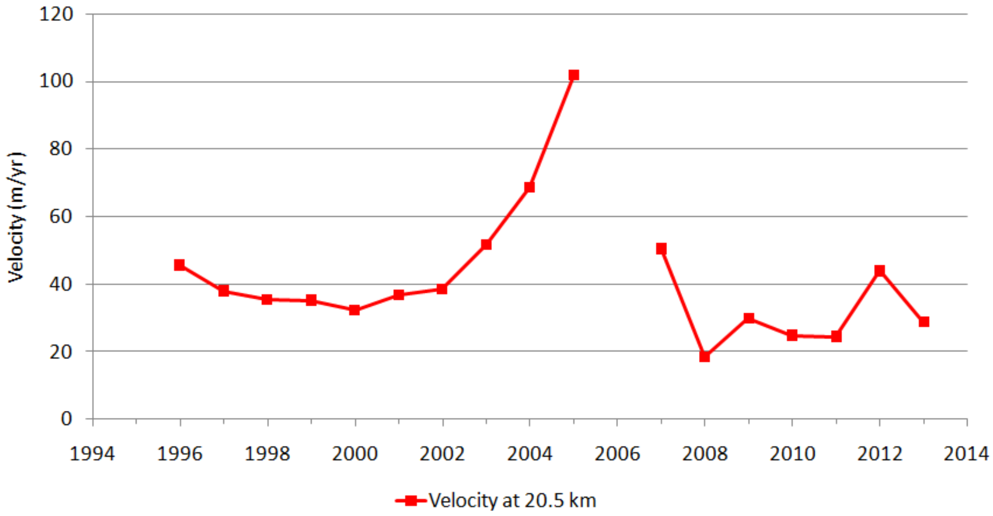

Figure 3.32. Velocity of Sanford Glacier through time, at the 20.5 km mark. One pulse cycle is seen, with a peak in 2005 of 101.7 m/yr.

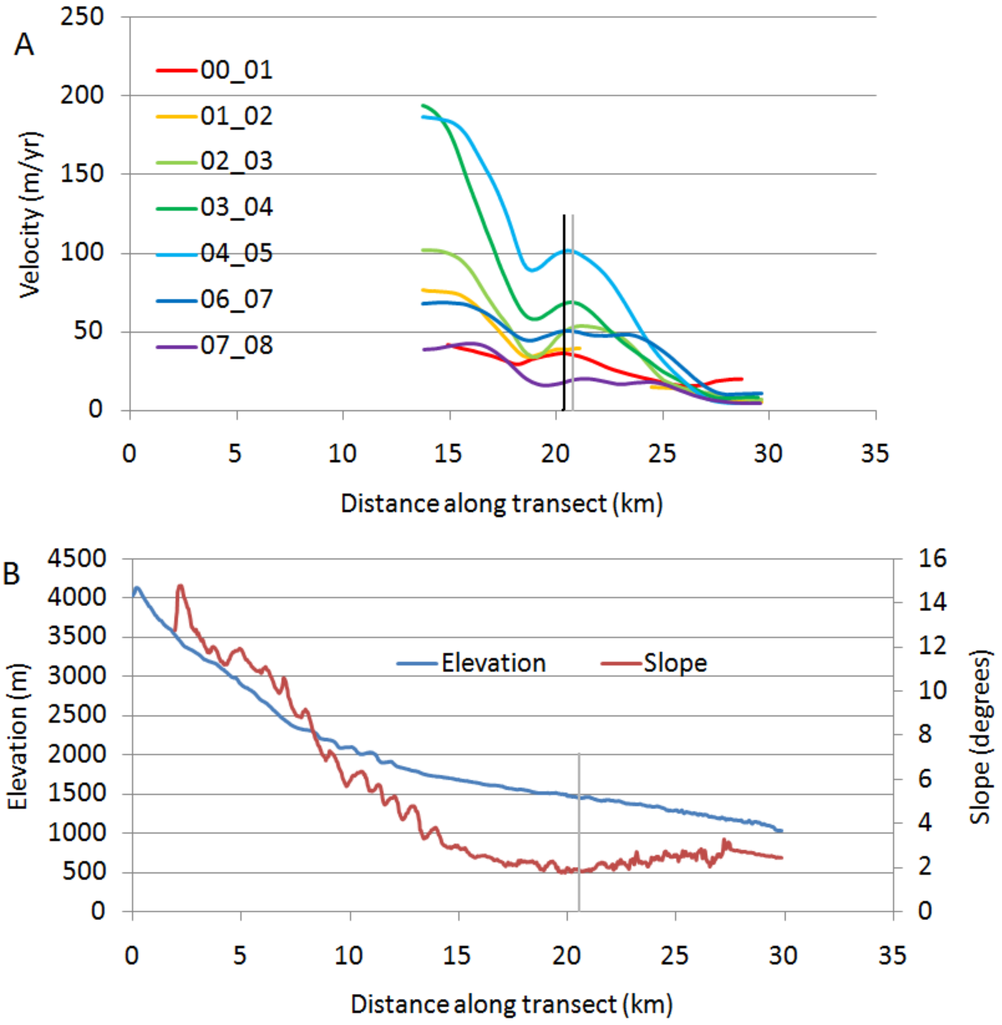

Figure 3.33. Centerline profiles for Sanford Glacier. A) Velocity profiles from 2000–2001 to 2007–2008 showing the pulse. B). Elevation and slope of the glacier surface. Vertical black line at the 20.5 km mark in panel A indicates position at which velocity values were taken to create time-series in Figure 3.32. Vertical gray line at the 21 km mark indicates location of change in bedrock lithology discussed in Section 3.5.8.

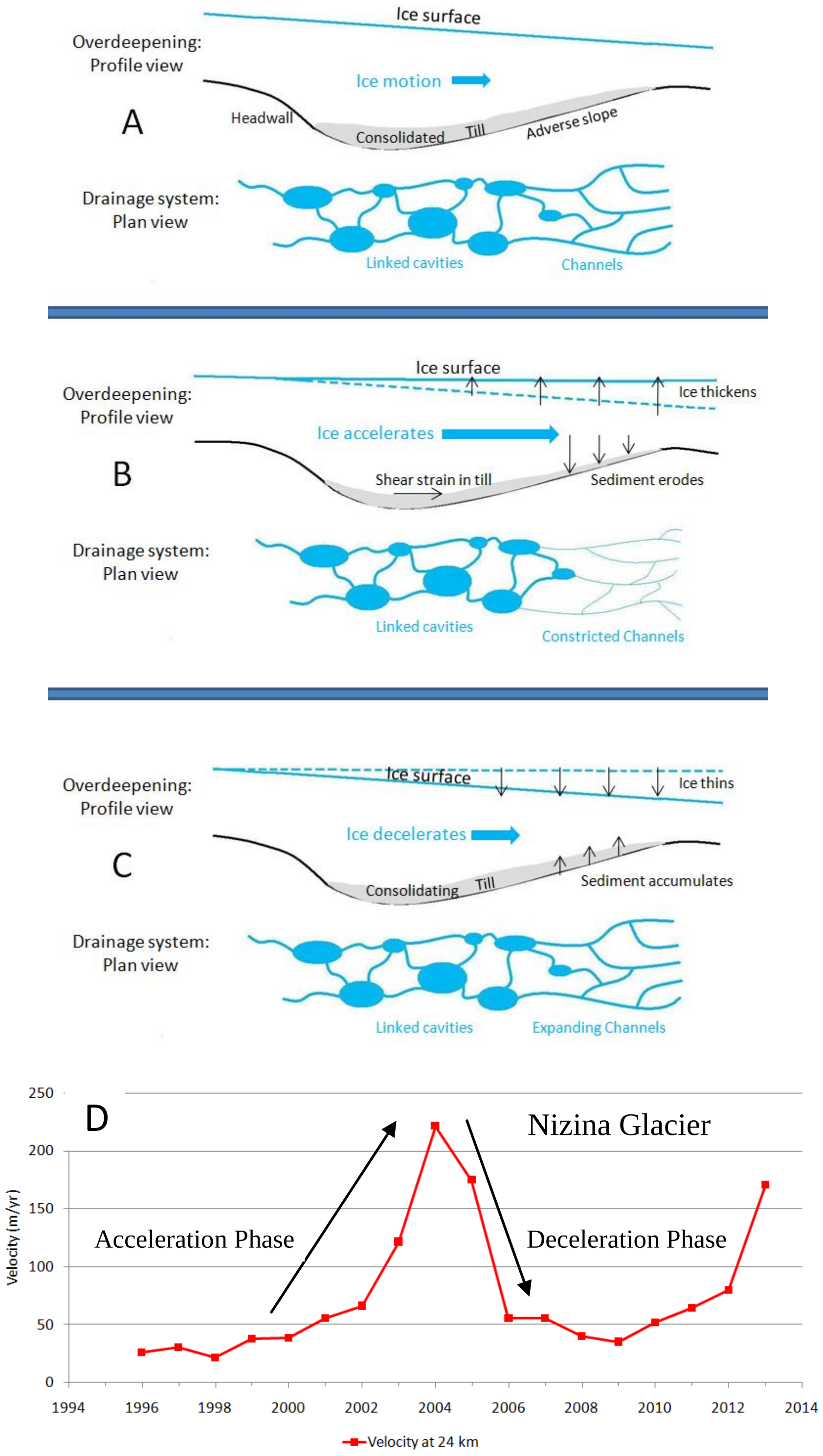

Figure 3.34. Illustration of the physical mechanisms which cause glacier pulses. A) Initial conditions. B) Acceleration phase. C) Deceleration phase. D) Example of resultant velocity time-series. See Section 3.6.5 for complete description.

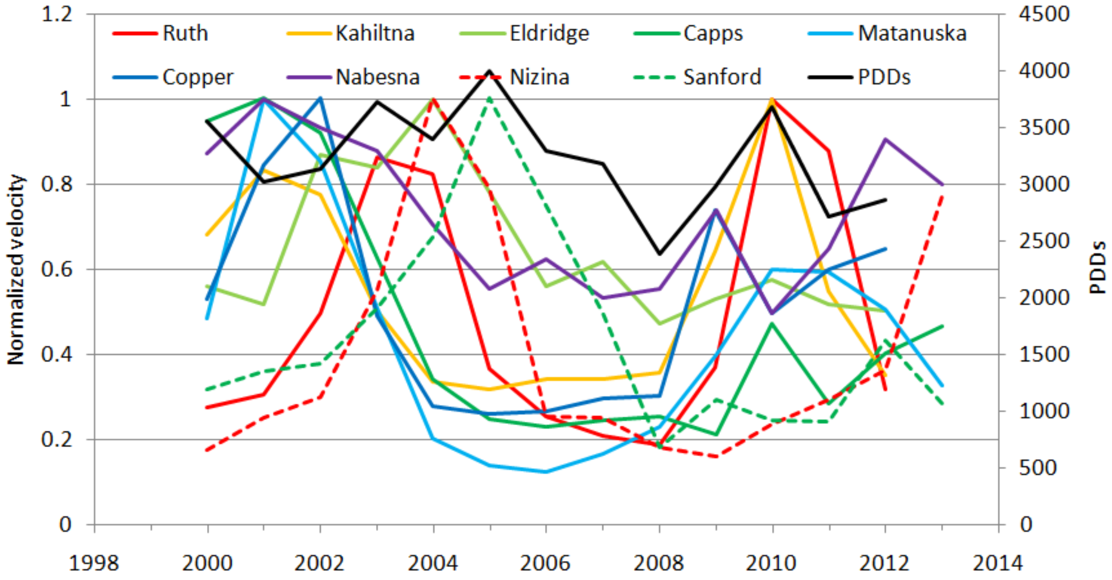

Figure 3.35. Normalized velocity of nine pulsing glaciers and Positive Degree Days (PDDs). Four pulses peaked in 2001 (Capps, Matanuska, Kahiltna, Nabesna); three pulses peaked in 2010 (Kahiltna, Matanuska, Ruth) and Capps Glacier had a spike in velocity this same year; two pulses peaked in 2004 (Eldridge, Nizina). The coincident peaks suggest synchronicity between glaciers that exist within the same regional climate. The simultaneous peak of PDDs and three pulsing glaciers in 2010 illustrates the influence annual meteorological conditions can have on the pulse cycle by causing glaciers currently in the acceleration phase of a pulse to peak.

3.8 References

Alley, R. B., Lawson, D. E., Evenson, E. B., Strasser, J. C., & Larson, G. J. (1998). Glaciohydraulic supercooling: A freeze-on mechanism to create stratified, debris-rich basal ice: II. Theory. Journal of Glaciology, *44*(148), 563–569.

Alley, R. B., Lawson, D. E., Larson, G. J., Evenson, E. B., & Baker, G. S. (2003). Stabilizing feedbacks in glacier-bed erosion. *Nature*, *424*(6950), 758–760.

Bond, G. C. & Lotti, R. (1995). Iceberg discharges into the North Atlantic on millennial time scales during the last glaciations. *Science*, *267*(5200), 1005–1010.

Capps, S. R. (1910). Glaciation on the north side of the Wrangell Mountains, Alaska. *Journal of Geology*, *18*(1), 33–57.

Clarke, G. K. C. (2005). Subglacial processes. *Annu. Rev. Earth Planet Sci.*, *33*, 247–276.

Cook, J. S., & Swift, D. A. (2012). Subglacial basins: Their origin and importance in glacial systems and landscapes. *Earth-Science Reviews*, *115*(4), 332–372.

Creyts, T. T., Clarke, G. K. C., & Church, M. (2013). Evolution of subglacial overdeepenings in response to sediment redistribution and glaciohydraulic supercooling. *Journal of Geophysical Research: Earth Surface*, *118*(2), 423–446.

Dow, C. F., Kavanaugh, J. L., Sanders, J. W., Cuffey, K. M., & MacGregor, K. R. (2011). Subsurface hydrology of an overdeepened cirque glacier. *Journal of Glaciology*, *57*(206), 1067–1078.

Evenson, E. B., Lawson, D. E., Strasser, J. C., Larson, G. J., Alley, R. B., Ensminger, S. L., & Stevenson, W. E. (1999a). *Field evidence for the recognition of glaciohydraulic supercooling.* Geological Society of America Special Paper, 337, 23-25, Boulder, CO. Eds. D. M. Mickelson and J. W. Attig.

Evenson, E. B., Larson, G. J., Lawson, D. E., Alley, R. B., & Fleisher, P. J. (1999b). Observations of glaciohydraulic supercooling at the Bering and Malaspina Glaciers, Southeastern Alaska: Geol. In *Soc. Am. Abstr. with Prog*, *30*, p. 258.

Evenson E. B., Lawson, D. E., Larson, G., Roberts, M., Knudsen, O., Russell, A. J., Alley, R. B., & Burkhart, P. (2001). Glaciohydraulic supercooling and basal ice in temperate glaciers of Iceland. *Geological Society of America Annual Meeting*, Nov. 5–8, 2001, paper 181-0.

Fitch, A. J., Kadyrov, A., Christmas, W. J., & Kittler, J. (2002). Orientation correlation. *British Machine Vision Conference*, 133–142.

Fountain, A. G. & Walder, J. S. (1998). Water flow through temperate glaciers. *Reviews of Geophysics*, *36*(3), 299-328.

Fowler, A. C. & Schiavi, E. (1998). A theory of ice-sheet surges. *Journal of Glaciology, 44*(146), 104–118.

Fowler, A. C., Murray, T., & Ng, F. S. L. (2001). Thermally controlled glacier surging. *Journal of Glaciology, 47*(159), 527–538.

Frappé, T. & Clarke, G. K. C. (2007). Slow surge of Trapridge Glacier, Yukon Territory, Canada. *Journal of Geophysical Research*, *112*(F03S32), doi:10.1029/ 2006JF000607.

Goodwin, K., Loso, M. G., & Braun, M. (2012). Glacial transport of human waste and survival of fecal bacteria on Mt. McKinley's Kahiltna Glacier, Denali National Park, Alaska. *Arctic, Antarctic, and Alpine Research*, *44*(4), 432–445.

Heid, T., & Kääb, A. (2012). Evaluation of existing image matching methods for deriving glacier surface displacements globally from optical satellite imagery. *Remote Sensing of Environment, 118*, 339–355.

Hooke, Roger LeB. (1989). Englacial and subglacial hydrology: A qualitative review. *Arctic and Alpine Research*, *21*(3), 221–233.

Hooke, R. L. & Pohjola, V. A. (1994). Hydrology of a segment of a glacier situated in an overdeepening, Storglaciären, Sweden. *Journal of Glaciology*, *40*(134), 140–148.

Hooke, Roger LeB. (2005). *Principle of glacier mechanics*, *2nd ed*. Cambridge University Press, Cambridge, UK. 429 p.

Jansson, P. (1996). Dynamics and hydrology of a small polythermal valley glacier. *Geogr. Ann. 78A*(2/3), 171–180.

Kamb, B., Raymond, C. F., Harrison, W. D., Engelhardt, H., Echelmeyer, K. A., Humphrey, N., Brugman, M. M., & Pfeffer, T. (1985). Glacier surge mechanism: 1982-1983 surge of Variegated Glacier, Alaska. *Science*, *227*(4686), 469–479.

Lawson, D. E., Strasser, J. C., Evenson, E. B., Alley, R. B., Larson, G. J., & Arcone, S. A. (1998). Glaciohydraulic supercooling: A freeze-on mechanism to create stratified, debris-rich basal ice: I. Field evidence. *Journal of Glaciology, 44*(148), 547–562.

Leprince, S., Barbot, S., Ayoub, F. & Avouac, J. P. (2007). Automatic and precise ortho-rectification, coregistration, and subpixel correlation of satellite images, application to ground deformation measurements. *IEEE Transactions on Geoscience and Remote Sensing*, *45*(6), 1529–1558.

Li, S., Benson, C., Gens, R., & Lingle, C. (2008). Motion patterns of Nabesna Glacier (Alaska) revealed by interferometric SAR techniques. *Remote Sensing of Environment, 112*, 3628–3638.

March, R. S., Mayo, L. R., & Trabant, D. C. (1997). *Snow and ice volume on Mount Spurr Volcano, Alaska, 1981*. U.S. Geological Survey Water-Resources Investigations Report 97-4142, 41 p.

Mayo, L. R. (1978). Identification of unstable glaciers intermediate between normal and surging glaciers. Academy of Sciences of the USSR. *Section of Glaciology of the Soviet Geophysical Committee and Institute of Geography, Data of Glaciological Studies Chronicle*, Discussion, Publication 133, 133-135, Moscow, May 1978.

Murray, T., Strozzi, T., Luckman, A., Jiskoot, H., & Christakos, P. (2003). Is there a single surge mechanism? Contrasts in dynamics between glacier surges in Svalbard and other regions. *Journal of Geophysical Research*, *108*(B5), doi:10.1029/2002JB001906.

Nolan, M. (2003). The “Galloping Glacier” trots: Decadal-scale speed oscillations within the quiescent phase. *Annals of Glaciology*, *36*(1), 7–13.

Penck, A. (1905). Glacial features in the surface of the Alps. *Journal of Geology*, *13*(1), 1–19.

Post, A. (1969). Distribution of surging glaciers in western North America. *Journal of Glaciology*, *8*(53), 229–240.

Richter, D. H., Preller, C. C., Labay, K. A., & Shew, N. B. (2006). Geologic Map of the Wrangell-Saint Elias National Park and Preserve, Alaska. U.S. Geological Survey Scientific Investigations Map 2877.

Truffer, M., Harrison, W. D., & Echelmeyer, K. A. (2000). Glacier motion dominated by processes deep in underlying till. *Journal of Glaciology*, *46*(153), 213–221.

Turrin, J. B., Forster, R. R., Larsen, C., & Sauber, J. (2013). The propagation of a surge front on Bering Glacier , Alaska, 2001-2011. *Annals of Glaciology, 54*(63), 221–228.

Turrin, J. B, Forster, R. R., Sauber, J. M., Hall, D. K. & Bruhn, R. L. (in review). Effects of bedrock lithology and subglacial till on the motion of Ruth Glacier, Alaska, deduced from five pulses from 1973–2012. *Journal of Glaciology*.

Ward, J. D., Anderson, R. S., & Haeussler, P. J. (2012). Scaling the Teflon Peaks: Rock type and the generation of extreme relief in the glaciated western Alaska Range. *Journal of Geophysical Research*, *117*, F01031, doi:10.1029/2011JF002068.

Willis, I. C. (1995). Intra-annual variations in glacier motion: A review. *Progress in Physical Geography*, *19*(1), 61–106.

Wilson, F. H., Dover, J. H., Bradley, D. C., Weber, F. R., Bundtzen T. K., & Haeussler, P. J. (1998). Geologic Map of Central (Interior) Alaska. U.S. Geological Survey Open-File Report OF 98-133.

CONCLUSION AND FUTURE WORK

Summarized below are the chief findings of the research presented in Chapters 1–3, beginning with the research involving pulsing glaciers, and followed by the surge of Bering Glacier. This section concludes with a discussion of possible future work.

A time-series of velocity maps spanning 4 decades, from the early 1970s through the 2000s, reveals 9 pulsing glaciers in southern Alaska: Capps, Eldridge, Kahiltna, and Ruth glaciers in the Alaska Range, Matanuska Glacier in the Chugach Mountains, and Copper, Nizina, Nabesna, and Sanford glaciers in the Wrangell Mountains. Each of these glaciers has the spatiotemporal velocity signature of a pulsing glacier in part of their ablation zone, which includes a multiyear acceleration phase followed by a multiyear deceleration phase, and the absence of a kinematic wave. Additionally, each of these glaciers pulsed where they were either laterally constricted or joined by a major tributary, and their surface slopes at these locations are very shallow, in the range of 1–2°. These physical traits are consistent with overdeepenings.

Based on previous observations of glaciers with cyclical pulsing behavior that are known to have a subglacial till, such as on Trapridge Glacier, Yukon, Canada (Frappé & Clark, 2007), and Black Rapids Glacier, Alaska (Nolan, 2003), it is concluded that enhanced basal motion via till deformation is responsible for acceleration of these pulse-type glaciers. To explain the cyclical behavior of pulsing glaciers, a process is introduced that incorporates a previous theory of glaciohydraulic supercooling in overdeepenings

(Alley et al., 2003), sediment deposition, erosion and transport along an adverse slope, ice thickening, and ablation of the ice surface, such that the ratio of the angle of the adverse slope to the ice surface slope oscillates around the supercooling threshold. Periodic freezing of water in subglacial channels as it traverses an adverse slope causes high water pressure in the overdeepening that allows the subglacial till to dilate and deform, and causes the glacier to accelerate. This is followed by periods of lower water pressure when the supercooling threshold is no longer exceeded and subglacial drainage channels expand, allowing the till to consolidate which causes the glacier to decelerate.

A decade-long time-series of velocity maps of Bering Glacier from 2001 to 2011 reveals the movement of a kinematic wave through its ablation zone. The wave is first observed in 2001 near the confluence of Bering Glacier with Bagley Ice Valley. From September 2002 to April 2009 the kinematic wave traveled at a mean rate of 4.4 ± 2.0 km/yr down the Bering Arm. The relatively constant velocity of the wave during this time suggests it was stabilized by diffusion before it entered the piedmont lobe (Fowler, 1987), after which it accelerated to 13.9 ± 2.0 km/yr. The wave took approximately a decade, from 2001 to 2011 to travel ~64 km down the ablation zone. A surge was triggered in 2008 after the kinematic wave passed an ice reservoir area in the upper ablation zone, activating the ice there. The surging ice achieved a rate of 1.5 ± 0.017 km/yr in 2008-2009 while the kinematic wave moved downglacier. The ice velocity increased to 4.4 ± 0.03 km/yr in the piedmont lobe once the surge front (kinematic wave) reached the glacier terminus in summer 2011 and the surge climaxed.

Chapters 1 and 2 add to our cumulative knowledge of the ice dynamics of large Alaskan glaciers in a changing climate. As this type of work is continued through the coming decades it will eventually become obvious what the trend in ice dynamics is, with regards to climate change and glacier flow instabilities. At that point, the fate of the Alaskan glaciers will also become clear. The new theory of glacier motion presented in Chapter 3 presents glaciologists with a new view of ice dynamics and the role overdeepenings play in glacier motion; a view that is more complex and more interesting than previously imagined; and of course, climate is a major influence on the processes central to this new theory.

The production of a time-series of annual velocity fields using optical feature tracking techniques for alpine glaciers has only recently proven to be a viable and valuable method of observation. So, future work could include production of a time-series of velocity fields for the glaciers of the St. Elias Range in Alaska, New Zealand, Patagonia, and Iceland, to find pulses of other glaciers. This additional data may help to confirm or modify the theory presented herein and further our understanding of pulsing glaciers and their response to climate change. These same time-series would be useful in re-examining past surges that occurred before optical feature tracking methods were fully developed, and they may also reveal previously unknown surges and their associated kinematic waves, or other glacial phenomenon.

For instance, while producing velocity fields for the Central Alaska Range, it was noticed that almost all the large glaciers of this mountain range currently have significantly reduced albedo in their ablation zones compared to their appearance in satellite images from the 1970s. The reduction in albedo is likely due to ice surface downwasting and accumulation of sediment atop the glacier. An opportunity exists to study the change in surface albedo of these glaciers and its effect on their mass balance. Regarding glaciers with flow instabilities, every opportunity should be taken to study surging and pulsing behavior because, as was noted in the Introduction, these types of glaciers are the majority of large glaciers in Alaska and will ultimately determine the region's contribution to sea-level rise. Extension of this type of work to the outlet glaciers and ice shelves of the two ice sheets would also be worthwhile. A 40-year time-series of velocity fields for the outlet glaciers of the ice sheets would provide a base-line with which future observations can be compared and establish a trend that would help predict their dynamic response to anticipated climate warming.

Optical feature tracking continues to evolve. There are recent developments that can improve the accuracy, or output density, of existing algorithms, but which have not yet been fully integrated into them. For example, Debella-Gilo and Kääb (2012) presented a technique to identify the best subimage size for use in cross-correlation calculations based on the variance of brightness values in each image. Selection of the best subimage size improves the strength of the correlation coefficient, thereby increasing the number of reliable measurements. Wavelet-based image matching has been shown to be capable of producing velocity fields on glaciers as accurate as cross-correlation (Schubert, et al., 2013), with the added advantage of producing dense velocity maps that may be preferable in areas of greater velocity gradient, such as at a surge front. When performing subpixel interpolation of a correlation peak, existing phase correlation algorithms often use either a Gaussian, parabolic, or sinc ($\sin\pi x/\pi x$) fitting function. Argyriou and Vlachos (2007) introduced an esinc fitting function ($\exp(-x^2)\sin\pi x/\pi x$) that has better subpixel accuracy compared to other fitting functions because it more closely approximates the impulse function output by phase correlation algorithms. As a final note, the fields of computer vision, medical imaging, and astronomy are generally more advanced in terms of their image analysis techniques than glaciology, and they may contribute to future advances in remote sensing of glaciers.

References

Alley, R. B., Lawson, D. E., Larson, G. J., Evenson, E. B., & Baker, G. S. (2003). Stabilizing feedbacks in glacier-bed erosion. *Nature*, *424*(6950), 758–760.

Argyiou, V., & Vlachos, T. (2007). On the estimation of subpixel motion using phase correlation. *Journal of Electronic Imaging, 16*(3), 033018.

Debella-Gilo, M., & Kääb, A. (2012). Locally adaptive template sizes for matching repeat images of Earth surface mass movements. *ISPRS Journal of Photogrammetry and Remote Sensing*, *69*, 10–28.

Fowler, A. C. (1987). A theory of glacier surges. *Journal of Geophysical Research, 92*(B9), 9111–9120.

Frappé, T., & Clarke, G. K. C. (2007). Slow surge of Trapridge Glacier, Yukon Territory, Canada. *Journal of Geophysical Research*, *112*(F03S32), doi:10.1029/ 2006JF000607.

Nolan, M. (2003). The “Galloping Glacier” trots: Decadal-scale speed oscillations within the quiescent phase. *Annals of Glaciology*, *36*(1), 7–13.

Schubert, A., Faes, A., Kaab, A., & Meier, E. (2013). Glacier surface velocity estimation using repeat TerraSAR-X images: Wavelet- vs. correlation-based image matching. *ISPRS Journal of Photogrammetry and Remote Sensing*, *82*, 49–62.